

MILLIMETER-WAVE FARADAY ROTATION FROM FERROMAGNETIC  
NANOWIRES AND MAGNETOELASTIC MATERIALS

A Dissertation

Presented to

The Graduate Faculty of The University of Akron

In Partial Fulfillment

of the Requirements for the Degree

Doctor of Philosophy

Nitin Parsa

August, 2019

MILLIMETER-WAVE FARADAY ROTATION FROM FERROMAGNETIC  
NANOWIRES AND MAGNETOELASTIC MATERIALS

Nitin Parsa

Dissertation

Approved:

Accepted:

---

Advisor

Dr. Ryan C. Toonen

---

Department Chair

Dr. Robert Veillette

---

Committee Member

Dr. Kye-Shin Lee

---

Dean of the College

Dr. Craig Menzemer

---

Committee Member

Dr. Igor Tsukerman

---

Dean of the Graduate School

Dr. Chand K. Midha

---

Committee Member

Dr. Ben Yu-Kuang Hu

---

Date

---

Committee Member

Dr. Ernian Pan

## ABSTRACT

This dissertation investigates the property of Faraday rotation in ferromagnetic nanowires and magnetoelastic materials for designing non-reciprocal signal processing components such as isolators and circulators. Nickel based ferromagnetic nanowires were grown in track-etched polycarbonate membranes using a three electrode electrodeposition technique where as magnetoelastic material consisting of silicone rubber infused with nickel microparticles was grown on an electromagnetic processing line. A customized measurement system with quasioptical and waveguide based components is proposed for Faraday rotation measurements at 61.25 GHz. Four different sets of experiments were performed. The first two sets of experiments confirmed the presence of Faraday rotation in ferromagnetic nanowires. A Verdet constant was extracted from experimental data was found to have a relatively high value of approximately  $25.5 \times 10^3 \text{ radT}^{-1}\text{m}^{-1}$ . The third set of experiments were performed on magnetoelastic materials. Faraday rotation in these experiments was calculated and found to be voltage dependant. The fourth set of experiments were performed on magnetoelastic materials inorder to determine the magnetic field sensing capability of the designed system. From the experimental data it was observed that the designed system was able to sense the static magnetic flux density up to 0.38 mT.

## ACKNOWLEDGEMENTS

I would like to express my deepest gratitude to my advisor Dr. Ryan C. Toonen for his encouragement, support and advice during the course of my graduate studies. It would not have been possible to work on my research and write the dissertation without his help and support. I would like to sincerely thank my committee members Dr. Kye-Shin Lee, Dr. Igor Tsukerman, Dr. Ben Yu-Kuang Hu and Dr. Ernian Pan for their support, guidance and motivation.

I would also like to thank my friend and colleague in Zip Electronic Nanotechnology Lab (ZEN LAB) Michael Gasper for his help and support. Last but not least, I would like to thank my parents, my brother for their encouragement and eternal love towards me. My family, friends, Drishti-Indian Student Association and Akron Cricket Club has the greatest ability to motivate me and help me throughout my graduate studies. I cordially thank all of them.

## TABLE OF CONTENTS

	Page
LIST OF TABLES . . . . .	viii
LIST OF FIGURES . . . . .	ix
CHAPTER	
I. INTRODUCTION . . . . .	1
1.1 Overview . . . . .	1
1.2 Polarization of EM Wave . . . . .	2
1.3 Faraday rotation . . . . .	3
1.4 Birefringence . . . . .	6
1.5 Ferromagnetic nanowires . . . . .	7
1.6 Magnetoelastic materials . . . . .	7
1.7 Dissertation contributions . . . . .	9
1.8 Organization of Dissertation . . . . .	9
II. LITERATURE REVIEW . . . . .	11
2.1 Non-reciprocal signal processing components . . . . .	11
2.2 Ferromagnetic nanowires background . . . . .	14
2.3 Magnetoelastic materials . . . . .	18
2.4 Gaussian beam propagation derivation . . . . .	20

2.5	Fundamental mode Gaussian beam and Edge taper . . . . .	26
2.6	Paraxial limit . . . . .	27
III.	MATERIAL GROWTH . . . . .	30
3.1	Template based approach of growing nanowires . . . . .	30
3.2	Magnetoelastic material . . . . .	39
IV.	SMALL ANGLE FARADAY ROTATION . . . . .	44
4.1	Stokes polarization parameters . . . . .	44
4.2	Mueller matrices for polarizing components . . . . .	46
4.3	Analytical expression for calculating Faraday rotation . . . . .	53
V.	DESIGN OF 3D PRINTED AND QUASIOPTICAL COMPONENTS . . . . .	56
5.1	Ray matrix analysis . . . . .	56
5.2	Transformation by a general quasioptical system . . . . .	58
5.3	Design of dielectric lens . . . . .	60
5.4	Design of spherical mirror . . . . .	65
5.5	Design of sample holder . . . . .	67
5.6	Design of dielectric beam splitter . . . . .	70
5.7	Gaussian beam measurements . . . . .	72
VI.	EXPERIMENTS AND RESULTS . . . . .	76
6.1	Customized signal generator . . . . .	76
6.2	Experiments . . . . .	77
VII.	CONCLUSION AND FUTURE OUTLOOK . . . . .	104

7.1 Conclusion . . . . .	104
7.2 Future Outlook . . . . .	104
BIBLIOGRAPHY . . . . .	108
APPENDICES . . . . .	114
APPENDIX A. SMALL ANGLE FARADAY ROTATION DERIVATION	115
APPENDIX B. MATLAB GUI . . . . .	120

## LIST OF TABLES

Table		Page
2.1	Fundamental Gaussian Beam Mode and Edge Taper . . . . .	28
2.2	Paraxial limit approximation . . . . .	29
5.1	Transformation parameters of Gaussian beam using lens 1 . . . . .	61
5.2	Transformation parameters of Gaussian beam using lens 2 and lens 3 . . . . .	62
5.3	Parameters used to design beam splitter . . . . .	72
6.1	Table comparing verdet constants of different materials . . . . .	93

## LIST OF FIGURES

Figure	Page
1.1 Polarization of an EM wave . . . . .	4
1.2 Depiction of non-reciprocal behavior from a waveguide based isolator with cases involving (a) alignment and (b) anti-alignment of direction of signal propagation with that of an externally applied magnetic field . . . . .	5
1.3 Depiction of birefringence (reciprocal behavior) in an anisotropic material (a) alignment and (b) anti-alignment of direction of signal propagation with that of an externally applied magnetic field. . . . .	6
1.4 Schematic of (a) Nanoporous template (b) Nanoporous template with nanowires . . . . .	8
1.5 Schematic of magnetoelastic material in (a) no magnetic field (b) applied magnetic field . . . . .	8
2.1 Faraday rotation circulator . . . . .	12
2.2 Junction Circulator a) Schematic b) Geometry . . . . .	13
2.3 Schematic illustration of Faraday rotation . . . . .	13
2.4 Standing wave pattern in a junction circulator . . . . .	14
2.5 Nanowire based circulator . . . . .	16
2.6 Nanowire based noise supressor . . . . .	17
2.7 Nanowire based PBG materials . . . . .	17
2.8 Nanowire based transmission line . . . . .	18
2.9 Magnetoelastic material based pressure sensor . . . . .	19

2.10	Magnetoelastic material based wireless resonance sensor . . . . .	20
3.1	Schematic of electrodeposition setup . . . . .	32
3.2	Photograph of three electrode electrodeposition technique . . . . .	33
3.3	Polycarbonate template (a) before gold sputtering (b) after gold sputtering . . . . .	33
3.4	Working electrode used in electrodeposition . . . . .	34
3.5	Schematic of stages in electrodeposition process . . . . .	35
3.6	Graph showing different stages of electrodeposition from current monitored during the process . . . . .	36
3.7	SEM image of nanowires in second stage of deposition . . . . .	36
3.8	SEM image of nanowires in third stage of deposition . . . . .	37
3.9	SEM image of nanowires in the fourth stage of deposition . . . . .	37
3.10	Experiments performed to identify the in-pore growth stage . . . . .	38
3.11	Current monitored during the in-pore growth . . . . .	38
3.12	SEM image of nickel nanowires after dissolving polycarbonate template (attached to gold). . . . .	39
3.13	SEM image of Novamet Type 123 nickel particles . . . . .	40
3.14	a) Schematic of EMP line. Side view of Ni microparticles embedded in PDMS membrane (b) before and (c) after passing through a high magnetic field. . . . .	41
3.15	SEM image of silicone rubber infused with nickel microparticles . . . . .	42
3.16	Demonstration of inverse magnetostriction effect . . . . .	42
4.1	Interaction of polarized EM wave with a polarizing element . . . . .	48
4.2	Mueller matrix of a polarizer with attenuation coefficients $p_x$ and $p_y$ . . . . .	49
4.3	Polarization rotator . . . . .	52

4.4	Horizontal component of E-field . . . . .	54
4.5	Vertical component of E-field . . . . .	54
5.1	Transformation of a Gaussian beam using a quasioptical component . .	59
5.2	Transformation of a Gaussian beam by lens 1 . . . . .	61
5.3	Transformation of a Gaussian beam by lens 2 and lens 3 . . . . .	62
5.4	2D model of lens 1 with dimensions . . . . .	63
5.5	2D model of lens 2 with dimensions . . . . .	63
5.6	2D model of lens 3 with dimensions . . . . .	64
5.7	Photograph of the fabricated lens . . . . .	65
5.8	Schematic illustrating the role of spherical mirror . . . . .	66
5.9	2D model of the spherical mirror with dimensions . . . . .	66
5.10	Photograph of the spherical mirror . . . . .	67
5.11	Photograph of custom made sample holder . . . . .	68
5.12	Crystal holder used for holding magnetoelastic material sample . . . . .	69
5.13	Photograph of custom made sample holder used for FMNWs sample . .	69
5.14	Photograph of custom made sample holder used for magnetoelastic material sample . . . . .	70
5.15	Static magnetic field from the electromagnet . . . . .	71
5.16	Photograph of beam splitter used in the experiments . . . . .	72
5.17	Gaussian beam measurement technique using horn antenna as a receiver antenna . . . . .	73
5.18	Gaussian beam measurement technique using dual polarized horn antenna as a receiver antenna . . . . .	74

6.1	Schematic of signal generator . . . . .	77
6.2	Three polarizer experiment . . . . .	79
6.3	Schematic of the apparatus in the first set of experiments . . . . .	80
6.4	Detected Gaussian beam ( FWHM= 21mm) . . . . .	80
6.5	Photograph of the mmW Faraday rotation apparatus used in the first set of experiments . . . . .	82
6.6	Plot comparing gain data in the first set of experiments . . . . .	83
6.7	Plot comparing gain data for filled template at different DC magnetic bias	83
6.8	Detected Gaussian beam (FWHM= 15mm) . . . . .	85
6.9	Power detected from channel A . . . . .	85
6.10	Power detected from channel B . . . . .	86
6.11	Schematic of the quasioptical system in the second set of experiments .	87
6.12	Photograph of the mmW Faraday rotation apparatus in the third set of experiments . . . . .	88
6.13	Location of different elements in the quasioptical system . . . . .	89
6.14	Gaussian beam after passing through lens 1 . . . . .	89
6.15	Detected Gaussian beam after passing through lens 2 and lens 3 . . . . .	90
6.16	Detected Gaussian beam after passing through sample holder . . . . .	90
6.17	Detected Gaussian beam at the location of the spherical mirror . . . . .	91
6.18	Detected Gaussian beam after reflecting back from the beam splitter . .	91
6.19	Faraday rotation measured at static magnetic fields of 30 mT and 18 mT	92
6.20	Faraday rotation measured at different magnetic fields . . . . .	94
6.21	Schematic of the quasioptical system used in the third set of experiments	95

6.22	MUT attached to a piezoring . . . . .	96
6.23	Strain experiments on magnetoelastic membranes. Images focused on surface of unstrained membrane with objective lens magnifications of (a) $2.5\times$ and (b) $20\times$ . (c) Image focused near midpoint of membrane thickness with objective lens magnification of $20\times$ . (d), (e), (f) Images of membrane under strain collected with the same microscope settings (g), (h), (i) Images of relaxed membrane (returned to unstrained state) collected with the same microscope settings.	97
6.24	Differential Faraday rotation as a function of frequency for different values of amplitude of piezoelectric driving signal. Data corresponding to the case of $V_{Piezo} = 16V$ has been fit to a Lorentzian lineshape. A radial resonant frequency of approximately 160 kHz has been extracted. . . . .	99
6.25	Differential Faraday rotation plotted as function of amplitude of piezoelectric driving signal (whose frequency was set to 150 kHz) for values of static magnetic field corresponding to $B = 18$ mT and $B = 30$ mT. Data has been obtained from the magnetoelastic membrane and a non-magnetic control sample. . . . .	100
6.26	Differential Faraday rotation with applied voltage on the piezo crystal .	102
6.27	Differential Faraday rotation at maximum value of applied voltage on the piezo crystal . . . . .	102

# CHAPTER I

## INTRODUCTION

This dissertation investigates the property of Faraday rotation in ferromagnetic nano-wires and magnetoelastic materials in an attempt to provide a solution to design size reduced, cost effective frequency agile non-reciprocal signal processing components at 61.25 GHz. In this chapter fundamental principles and basic definitions used in the dissertation are briefly discussed.

### 1.1 Overview

Non-reciprocal signal processing components such as circulators and isolators play a key role in transmitting and receiving modules in communications engineering. With the growth of wireless communication systems, the frequency is increasing and heading towards the wireless gigabit (WiGig) range. Hence there is a need to design these non-reciprocal signal processing components at these frequencies, which range from 57 to 70 GHz. A portion of this band falls under the unlicensed V-band and has recently received much attention for use in high-capacity, short-range, point-to-point data links that could enable emerging 5G technologies. Bulk ferrites with externally applied magnetic fields are traditionally used as anisotropic media of non-reciprocal signal processing components. However at millimeter-wave (mm-wave)

frequencies such ferrites are not recommended for monolithic microwave integrated circuits (MMIC) as they require biasing with relatively high magnetic fields. An alternative solution to this problem is to use remnant-state non-reciprocal devices thereby avoiding static magnetic field biasing [1]. The remnant-state, non-reciprocal devices can be obtained by using ferromagnetic nanowires (FMNWs). The use of FMNWs makes it possible to considerably reduce the size of the devices thereby increasing the possibility of intergating with MMICs. However, before one can engineer FMNWs for designing non-reciprocal signal processing components, there is a need to characterize the property of FMNWs (anisotropic media) to study the non-reciprocal behavior over the frequencies of interest. This dissertation proposes a custom made measurement system to study the non-reciprocal behavior in FMNWs. One of the drawbacks of non-reciprocal signal processing components is that they are narrow in bandwidth and require fine mechanical tuning (to operate at other frequencies) which is usually performed by a highly skilled technician and consequently increases production costs. In order to address this issue we have proposed the use of magnetoelastic materials to realize frequency agile non-reciprocal signal processing components.

## 1.2 Polarization of EM Wave

Electromagnetic (EM) waves have both electric field (E-field) and magnetic field (B-field) components perpendicular to each other and also to the direction of propagation.

EM waves can be defined with the following E-field wave equation

$$\nabla^2 E - \gamma^2 E = 0 \tag{1.1}$$

where  $\gamma = \sqrt{j\omega\mu(\sigma + j\omega\epsilon)}$  is called propagation constant,  $\omega$  is the radial frequency in rad/sec,  $\mu$  is permeability,  $\sigma$  is conductivity and  $\epsilon$  is permittivity.

In general EM waves have a direction in space which is constant or may change with the wave propagation. The polarization of EM waves can be defined as the figure traced by the tip of the E-field vector as a function of time, at a fixed point in space. Polarization is usually defined for an E-field vector as B-field is always obtainable from the E-field by using Maxwell equations. The tip of the E-field traces some pattern in the plane perpendicular to the direction of propagation of an EM wave. If the figure traced by the tip of the electric field intensity is a straight line, it is called linear polarization. If the figure traced by the tip of the electric field is an ellipse, then the polarization is said to be elliptical polarization. Circular polarization is a special case of elliptical polarization. Fig. 1.1 shows linearly polarized, circularly polarized and elliptically polarized EM wave [2].

### 1.3 Faraday rotation

In terms of engineering practical components, Faraday rotation is perhaps the most important manifestation of magnetically-broken time-reversal symmetry. It has been used to enable the most common types of non-reciprocal components (e.g. gyra-

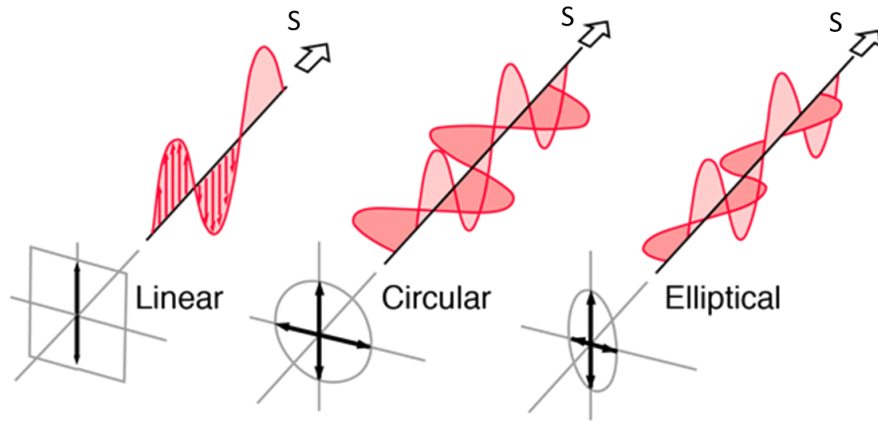


Figure 1.1: Polarization of an EM wave

tors, isolators, and circulators), which can manipulate the propagation direction of EM waves. Faraday rotation (non-reciprocal polarization) is a magneto-optical phenomenon which was first discovered by Michael Faraday. An anisotropic material (such as a ferrite immersed in an external B-field applied in the direction of EM propagation) produces a value of Faraday rotation  $\theta_{FR}$  that is directly proportional to the path length  $L$  of the EM wave through the material such that  $\theta_{FR} = VBL$  where  $V$  is a material-dependent constant (Verdet constant). Fig. 1.2 depicts the phenomenon of Faraday rotation that is used to create a waveguide-based isolator, which allows an EM wave to pass in one direction but not the other. In the case of components based on a WR-15 rectangular waveguide, the inner dimensions (width of 3.8 mm and height of 1.9 mm) have been chosen so that in-band signals (with frequencies ranging from 50 to 75 GHz) can only propagate through these transmission lines if their E-field component is aligned vertically along the waveguide's height.

As shown in Fig. 1.2 (a), when an incoming signal's direction of propagation  $S$  is aligned with the direction of the B-field, its E-field component will rotate by  $45^\circ$  in a right-handed (or clockwise) orientation (if the thickness of the anisotropic medium is chosen appropriately). By rotating the receiving waveguide aperture by the same angle, the signal will freely pass through the component.

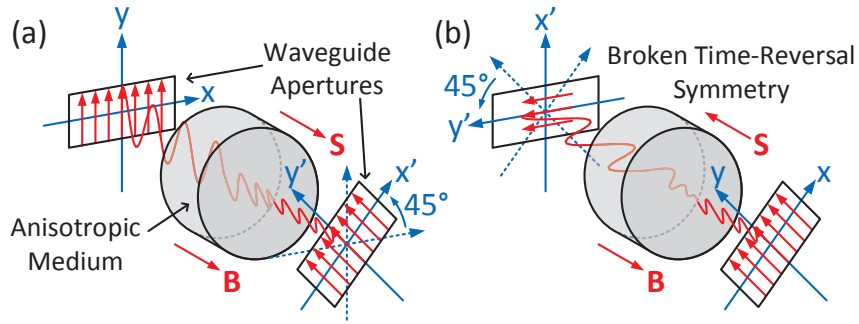


Figure 1.2: Depiction of non-reciprocal behavior from a waveguide based isolator with cases involving (a) alignment and (b) anti-alignment of direction of signal propagation with that of an externally applied magnetic field

However, as shown in Fig. 1.2 (b), if the signal's direction of propagation is reversed, its E-field will rotate by  $45^\circ$  in a left-handed orientation (this asymmetry is referred to as broken time-reversal symmetry), which will cause the signal's E-field component to be aligned in the horizontal direction of the receiving waveguide aperture. Since the waveguides only support signal propagation when the E-field is aligned with the vertical direction, the signal will not pass through the component.

## 1.4 Birefringence

Birefringence (reciprocal polarization) is an optical property of the materials having permittivity that depends up on the polarization of the incident EM wave. Fig. 1.3 (a) shows the depiction of birefringence in an isotropic material. When an incoming signal's direction of propagation  $S$  is allowed to pass through a isotropic material, the E-field component will rotate by some angle ( $45^\circ$  in this case). However if the signal's direction of propagation is reversed, the E-field will return back to its original position as shown in Fig. 1.3 (b). This reciprocal polarization behavior of isotropic materials is termed as birefringence.

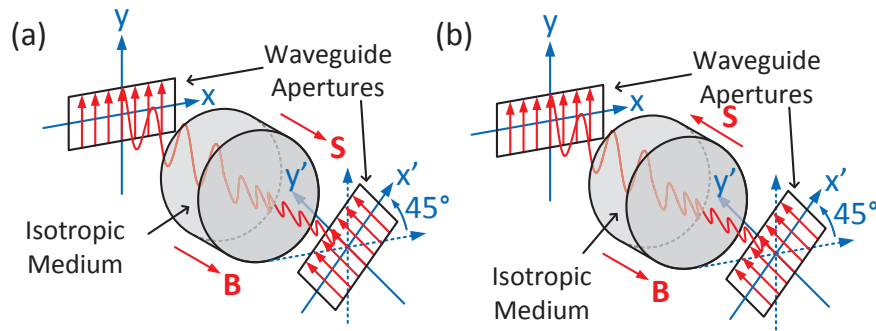


Figure 1.3: Depiction of birefringence (reciprocal behavior) in an anisotropic material (a) alignment and (b) anti-alignment of direction of signal propagation with that of an externally applied magnetic field.

## 1.5 Ferromagnetic nanowires

In the context of this dissertation FMNWs refer to a nanoporous template filled with ferromagnetic nanowires. Fig. 1.4 (a) shows the schematic of nanoporous template and Fig. 1.4 (b) shows the schematic of the template filled with FMNWs. FMNWs have received a considerable amount of attention due to their tunable magnetization properties, low cost and possible applications in high-frequency electronics. Although these materials are composed of ferromagnetic metals, they behave as electrically insulating ferrites and exhibit exotic properties not found in conventional materials [1],[3],[4] thus, they have been referred to as second-generation metamaterials [1]. Artificial ferrites based on arrays of aligned FMNWs embedded in dielectric host substrates have been used to realize non-reciprocal components [5], which isolate signals within microwave and mm-wave systems. These materials can be self-biased [1] eliminating the need for magnets that increase the size, weight and cost of the components.

## 1.6 Magnetoelastic materials

Magnetoelastic materials have the ability to change their elastic properties in the presence of an external B-field. This effect is termed as magnetostriction. A material is said to be magnetostrictive if the material develops strain when placed in a B-field. Similarly if the applied strain on a material changes the magnetic properties of the material, the effect is termed as inverse magnetostrictive effect. Fig. 1.5 (a) shows the

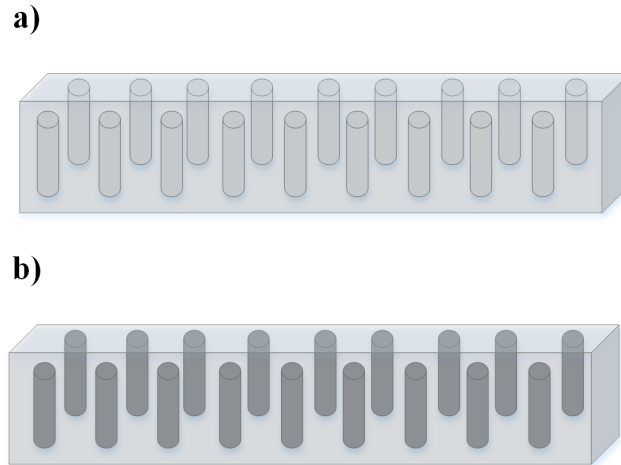


Figure 1.4: Schematic of (a) Nanoporous template (b) Nanoporous template with nanowires

magnetoelastic material in no B-field. Fig. 1.5 (b) shows the magnetoelastic material in the presence of B-field. It can be observed from the figures that the magnetic field has induced some strain in the material.

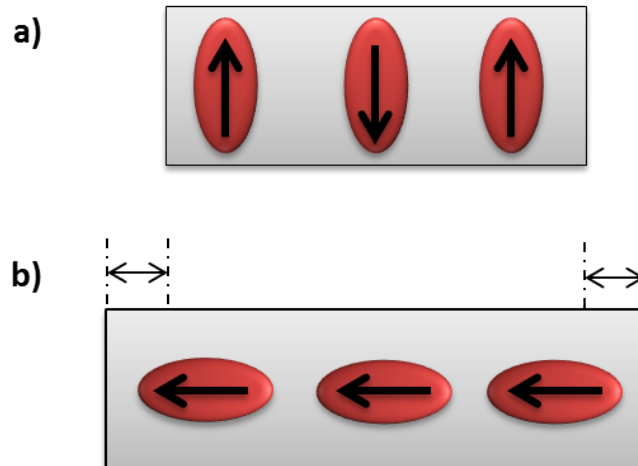


Figure 1.5: Schematic of magnetoelastic material in (a) no magnetic field (b) applied magnetic field

## 1.7 Dissertation contributions

The main objective of this dissertation is to study the property of Faraday rotation in FMNWs and magnetoelastic materials. The contributions in this dissertation are summarized as follows

1. Experimentally demonstrated the concept of mm-wave Faraday rotation in FMNWs.
2. Derived a mathematical expression for small angle Faraday rotation using Stokes vectors and Mueller matrix analysis.
3. Designed a unique waveguide and quasioptical based system in order to measure small angle Faraday rotation in FMNWs and magnetoelastic materials experimentally.
4. Demonstrated the concept of voltage controlled magnetism using magnetoelastic materials that has potential applications in designing tunable non-reciprocal signal processing components.
5. Demonstrated B-field detection using tunable Faraday rotation in magnetoelastic materials.

## 1.8 Organization of Dissertation

In Chapter 2 background on non-reciprocal signal processing components, Gaussian beam propagation, FMNWs based devices and magnetoelastic materials based devices are discussed. Chapter 3 demonstrates the fabrication of FMNWs in nanoporous

polymer membranes using electrodeposition and fabrication of nickel microspheres in silicone rubber using electromagnetic processing line. In Chapter 4 a mathematical expression for calculating small angle Faraday rotation in thin films was derived using Stokes parameters and Mueller matrix analysis. Chapter 5, discusses the design of all the quasioptical components and 3D printed components used to manipulate the Gaussian beam. In Chapter 6, four different sets of experiments along with their implementation and results are presented. In the final chapter conclusion followed by challenges and future outlook are discussed.

## CHAPTER II

### LITERATURE REVIEW

In this chapter, background on Faraday rotation based non-reciprocal signal processing components, Gaussian beam propagation, ferromagnetic nanowires, ferromagnetic nanowire based non-reciprocal signal processing components and magnetoelastic materials are discussed

#### 2.1 Non-reciprocal signal processing components

Isolators and circulators are the best examples of non-reciprocal signal processing components. A circulator in general is a three port or a four port device. The power is transferred from one port to the adjacent port. If one port is terminated among all three, then the circulator can be turned in to an isolator. An isolator is similar to a circulator in which the power flows unilaterally. The circulators can be mainly classified in to two caterogies: active and passive. Passive circulators generally have better performance compared to active circulators. All the passive circulators fall in to categories such as Faraday rotation circulator, junction circulator, ring circulator and differential phase shift circulator. In the context of this dissertation only Faraday rotation circulator and junction circulator are briefly discussed in the next sections.

### 2.1.1 Faraday rotation circulator

Faraday rotation circulator is based on the principle of Faraday rotation, a phenomenon of interaction between electromagnetic waves and magnetic field when the wave is propagating in a medium. A wave propagating in a medium with static magnetic field biasing experiences a polarization rotation. Without the magnetic field biasing two circular components equal in magnitude and opposite in phase are generated. They cancel with each other without changing the polarization of the wave. In the presence of magnetic field the phase of the circular components are no longer equal implying there will be a gradual rotation of the wave [6]. Faraday rotation can be easily imparted with a ferrite inside a waveguide as shown in Fig. 2.1 [6].

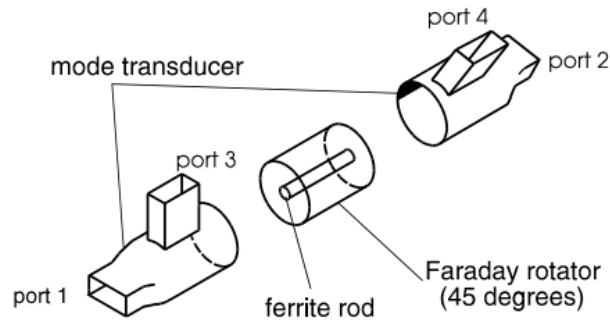


Figure 2.1: Faraday rotation circulator

### 2.1.2 Junction circulator

Junction circulators are the most commonly used circulators and are available in waveguide, stripline and microstrip line configurations. Fig. 2.2 shows the schematic

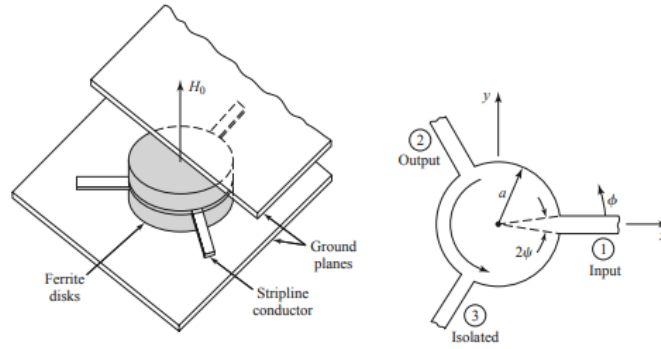


Figure 2.2: Junction Circulator a) Schematic b) Geometry

and geometry of the junction type circulator [7]. A typical junction circulator consists of a ground plane, ferrite disk and conducting line [7]. A linear polarized wave is sent through the circulator is split in to two circular polarized waves [8] that travel at the same speed but with opposite polarization directions as shown in Fig. 2.3. In the case

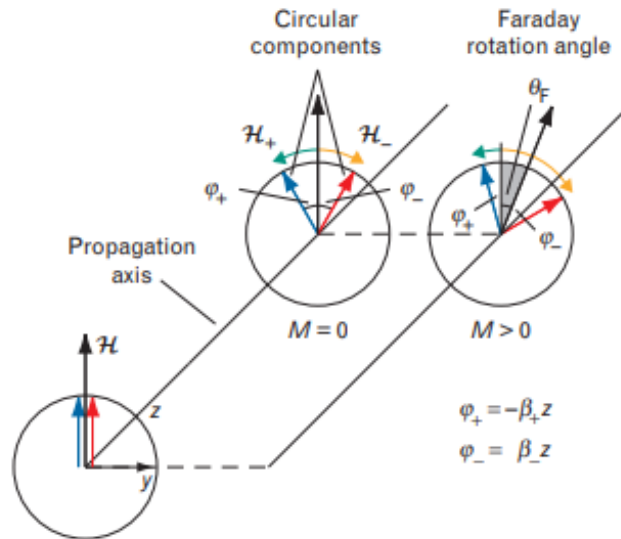


Figure 2.3: Schematic illustration of Faraday rotation

of zero magnetization ( $M = 0$ ), the linearly polarized wave is split into two circular polarized waves that will travel at the same speed and form a standing wave pattern as shown in Fig. 2.4. Therefore, the power is evenly split between port 2 and port 3. Non-zero magnetization ( $M > 0$ ) makes the speed of circular polarized waves unequal making the two waves sum up constructively and destructively at a certain distance from the input reference plane. From the standing wave point of view, the wave is either rotated clockwise or counterclockwise. If the wave is rotated counterclockwise the standing wave pattern will be similar to Fig. 2.4 (b) [6]. This implies the signal is coupled to port 2 while port 3 is uncoupled. If the wave is rotated clockwise the standing wave pattern will be similar to Fig. 2.4 (c) [6]. This implies that the signal is coupled to port 3 while port 2 is uncoupled.

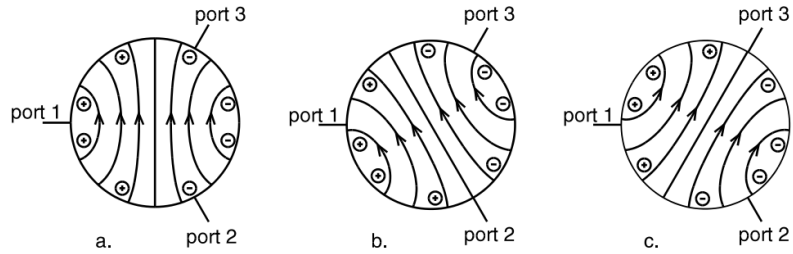


Figure 2.4: Standing wave pattern in a junction circulator

## 2.2 Ferromagnetic nanowires background

As far back as the 1850s, investigators of decorative and anti-corrosive coatings of metallic surfaces had used a technique [9] that would later be referred to as Anodic

Aluminum Oxide (AAO) synthesis. About 100 years later, the morphologies of such coatings were investigated and found to consist of highly-ordered / quasi-regular arrays of high-aspect-ratio nanopores [10]. During the same decade, nuclear scientists detected the tracks of energetic heavy ions in polymer membranes, and by the 1960s, chemical etching of ion tracks was used as a standard nuclear diagnostic [11], [12]. Although track-etched polymer membranes offer arrays of nanopores with uniform diameter, the nanopore spacing is random. In the mid 1970s, Ferromagnetic Nanowires (FMNWs) were synthesized in the pores of AAO coatings on aluminum substrates by means of electroplating and characterized in terms of their magnetic properties [13]. At that time, however, few if any, efforts focused on exploiting the unique properties offered by nanowires for practical applications. The idea of using nanowires in microwave and optical communication components was first proposed in 1990 by a panel of 30 scientists and engineers who convened to address the very question of what nanowires might be good for [14],[15]. Around that time, researchers took interest in template synthesis as a means of bottom-up nanomanufacturing [7]. These materials were synthesized by electroplating the nanopores of AAO [16] and track-etched polymer membranes [17], [18] with metals such as Ni, Cobalt (Co), Iron (Fe), and several alloys thereof. Today, both AAO and track-etched polymer nanoporous templates are commercially available, inexpensive, and commonly used for biological sample filtration. In fact, template synthesis of metallic nanowires has become so accessible that a simplified method is often used in classroom demonstrations when introducing students to the field of nanotechnology [19].

### 2.2.1 Nanowires based non-reciprocal signal processing components

Artificial ferrites based on FNMWs have been used for fabrication of unbiased signal processing components up to 10 GHz [20], [21]. In general, the non-reciprocal signal processing components rely on magnetic materials. However at millimeter wave frequencies, traditional ferrite based circulators are disadvantageous in monolithic microwave integrated circuits, as they require a really high static magnetic field. A straightforward approach of remnant based circulators without static field biasing was proposed in [5], [21]. Fig. 2.5 shows the nanowired based circulator.

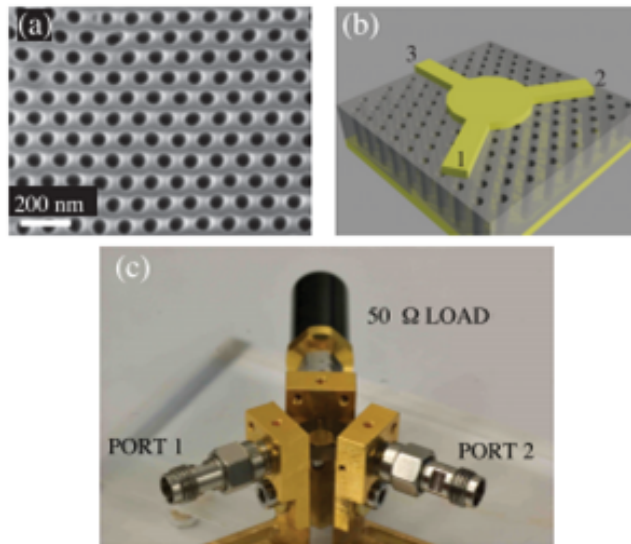


Figure 2.5: Nanowire based circulator

FMNWs have also been used as planar fully-integrated microwave nonreciprocal phase shifters at 50 GHz [22]. Usually nonreciprocal microstrip line phase shifters require the assembly of substrates with different permittivity. By asymmetric

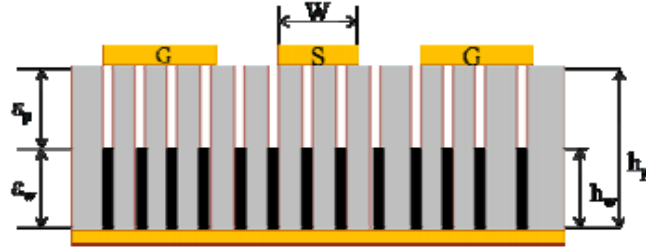


Figure 2.6: Nanowire based noise suppressor

filling of the FMNWs in the substrates, variation in the permittivity can be obtained [22]. FMNW integrated devices have also been used as noise suppressors. Fig. 2.6 shows the FMNW based noise suppressors. In the past, arrays of nanowires of Ni, Co, Co-Ni in AAO templates were used for these applications [23], [24].

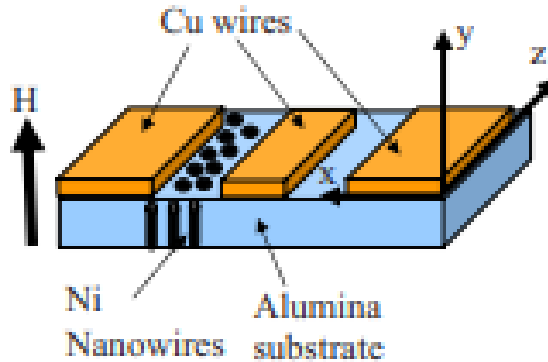


Figure 2.7: Nanowire based PBG materials

FMNWs provide good noise attenuation characteristics and high resonant frequencies [24]. These properties, in association with tunable magnetization, make the FMNW-integrated devices as good electromagnetic noise suppressors at high fre-

quencies [23],[24], [25]. FMNWs as a dielectric substrate have also been used in photonic band gap materials to replace ferrites and ferromagnetic materials [26], [27]. Fig. 2.7 shows the nanowired based photonic band gap materials. FMNWs have also been used as a slow wave microstrip lines in millimeter-wave circuits [28] as shown in Fig. 2.8. Although not involving FMNWs, non-planar inductors that operate at 100 GHz have been realized using copper nanowires as through-substrate vias [29]. Other experiments have focused on the magneto-optical properties of photonic resonances (at visible frequencies) in Ni nanowire arrays [30]. All in all FMNWs have shown promising applications in the field of microwave and millimeter wave engineering.

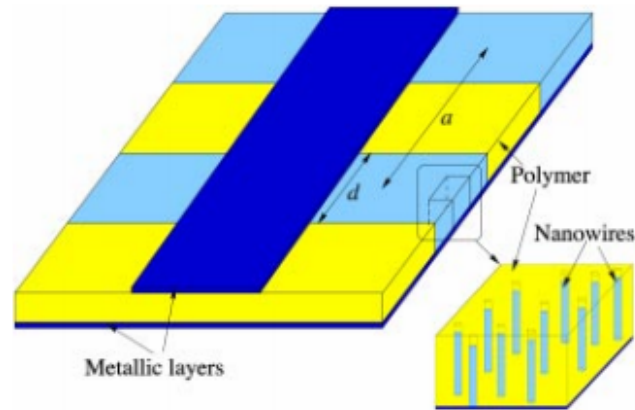


Figure 2.8: Nanowire based transmission line

### 2.3 Magnetoelastic materials

The history of magnetoelastic materials goes back to the early 1960's where in exceptionally large magnetostriction was observed from rare earth compounds [31] [32].

However, most of these materials exhibited magnetic behavior only at cryogenic temperatures which proved to be a major disadvantage. In 1970's a new material known as Terfenol-D was invented which exhibited the highest known room temperature magnetostriction [33]. However this material was very brittle and was often not preferred. Eventually in 1990's a new material, Galfenol was invented. This material exhibited smaller magnetostriction behavior compared to Terfenol-D, but is much more mechanically robust [34] [35]. Galfenol was used for sensing applications.

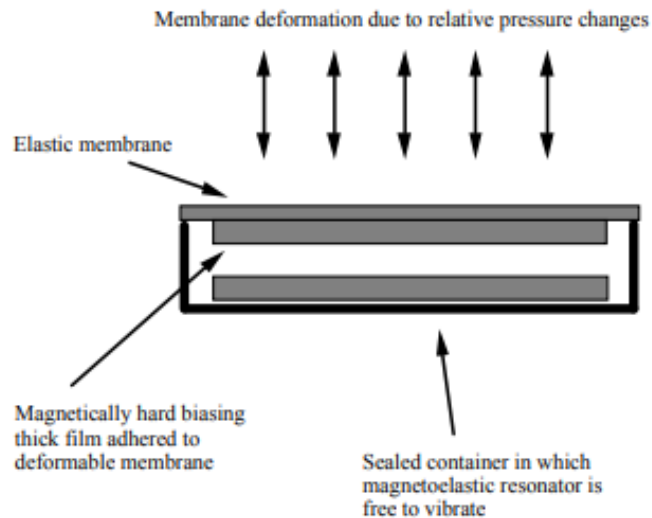


Figure 2.9: Magnetoelastic material based pressure sensor

Although magnetoelastic materials have many useful properties, they are used less often as these materials are usually large and bulky, requires magnetic bias, solenoid coils etc. However, these limitations started to disappear as the overall size of the magnetoelastic materials was reduced from macroscale to microscale [36]. Recently microstructured multiferroic materials have found several applications. Fig.

2.9 shows the schematic of magnetoelastic material based pressure sensor [37]. Fig. 2.10 shows the schematic of magnetoelastic material based wireless resonance sensor that can be used to detect stress, pressure, temperature etc. [38].

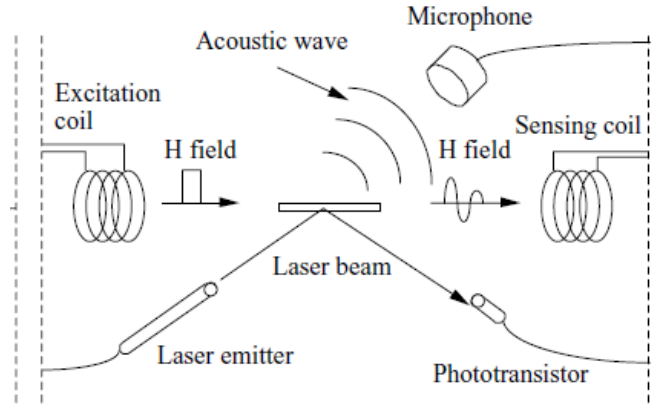


Figure 2.10: Magnetoelastic material based wireless resonance sensor

In this work, Gaussian beams at 61.25 GHz have been used to study Faraday rotation in FMNWs and magnetoelastic materials. In the next section, basic concepts of Gaussian beam propagation have been discussed.

#### 2.4 Gaussian beam propagation derivation

The propagation of an EM wave results in distribution of field amplitudes that is independent of position. The best example for this is a plane wave. In order to understand Gaussian beam, if we restrict the region over which there is initially a nonzero field, wave propagation becomes a problem of diffraction which results in a complex vector problem. Consider a case when a beam of radiation has a well-

defined direction of propagation but has also a transverse variation, thus developing paraxial wave equation which forms basis for Gaussian beam propagation. Thus a Gaussian beam does have limited transverse variation compared to a plane wave. It is different from a beam originating from a source in geometrical optics. The Gaussian beam originates from a region of finite extent, rather than from an infinitesimal point source. In order to derive an expression for Gaussian beam propagation [39], we start with the well known wave equation,

$$(\nabla^2 + k^2)\psi = 0 \quad (2.1)$$

where  $\psi$  represents either E-field or B-field,  $k$  represents wave number and can be given as

$$k = \omega \frac{\sqrt{\epsilon_r \mu_r}}{c} \quad (2.2)$$

where  $\omega$  is the angular frequency,  $c$  is the speed of light,  $\epsilon_r$  and  $\mu_r$  are the relative permittivity and permeability of the medium. Assuming the beam propagates along the  $Z$  direction, the solution to equation 2.1 (assuming  $\psi$  represents E-field) can be given as

$$E(x, y, z) = u(x, y, z)e^{-jkz} \quad (2.3)$$

where  $u$  is a complex scalar function that defines the non-plane wave part of the beam. Substituting this in to the rectangular coordinates of the Helmholtz equation, the

solution can be given as

$$\frac{\partial^2 u}{\partial x^2} + \frac{\partial^2 u}{\partial y^2} + \frac{\partial^2 u}{\partial z^2} - 2jk \frac{\partial u}{\partial z} = 0 \quad (2.4)$$

Assuming the variation along the direction of propagation of the amplitude  $u$  will be small over a distance comparable to wavelength ( $\lambda$ ) (due to diffraction) and the axial variation is smaller comparable to the variation in perpendicular direction, the paraxial wave equation in rectangular coordinates is given as

$$\frac{\partial^2 u}{\partial x^2} + \frac{\partial^2 u}{\partial y^2} - 2jk \frac{\partial u}{\partial z} = 0. \quad (2.5)$$

Equation 2.5 in cylindrical coordinates can be given as

$$\frac{\partial^2 u}{\partial r^2} + \frac{1}{r} \frac{\partial u}{\partial r} - 2jk \frac{\partial u}{\partial z} = 0, \quad (2.6)$$

where  $r$  represents the perpendicular component from  $Z$ -axis (axis of propagation). The equation 2.6 is independent of  $\varphi$  because of axial symmetry. In general the simplest solution of axially symmetric paraxial wave equation can be given as [39]

$$u(r, z) = A(z) e^{\frac{-jkr^2}{2q(z)}} \quad (2.7)$$

where  $A$  and  $q$  are the complex functions that are yet to be determined. Substituting

equation 2.7 in equation 2.6 we get

$$-2jk\left(\frac{A}{q} + \frac{\partial A}{\partial z}\right) + \frac{k^2 r^2 A}{q^2}\left(\frac{\partial q}{\partial z} - 1\right) = 0 \quad (2.8)$$

The terms that are in the parentheses in equation 2.8 should equal to zero as the equation should be satisfied for all  $r$  and  $z$ . Hence we have

$$\frac{\partial q}{\partial z} = 1 \quad (2.9)$$

and

$$\frac{\partial A}{\partial z} = -\frac{A}{q} \quad (2.10)$$

#### 2.4.1 Complex beam parameter

The Complex beam parameter,  $q(z)$  can be obtained by solving equation 2.9, the equation for  $q(z)$  is

$$q(z) = q(0) + z \quad (2.11)$$

Splitting the complex beam parameter in to real and imaginary parts we get

$$\left(\frac{1}{q}\right)_{real} = \frac{1}{R}, \quad (2.12)$$

and

$$\left(\frac{1}{q}\right)_{imag} = \frac{\lambda}{\pi w^2} \quad (2.13)$$

where  $R$  in equation 2.12 is the radius of curvature, that can be obtained from the real part and  $w$  in equation 2.13 is the beam radius from the imaginary part. Another equation for complex beam parameter can be obtained by using equation 2.7 by substituting  $z=0$  and  $w=w_0$  ( $w_0$  is the beam waist radius). This equation can be given as

$$q = \frac{j\pi w_0^2}{\lambda} + z \quad (2.14)$$

Now by using equations 2.12, 2.13 and 2.14, a generalized expression for radius of curvature and beam radius can be obtained as follows

$$R = z + \frac{1}{z} \left( \frac{\pi w_0^2}{\lambda} \right)^2 \quad (2.15)$$

$$w = w_0 \sqrt{\left[ 1 + \left( \frac{\lambda z}{\pi w_0^2} \right)^2 \right]} \quad (2.16)$$

Using equation 2.16 the beam waist radius is the minimum value of waist radius at beam waist. It can be noticed that at the position of beam waist radius, radius of curvature ( $R$ ) is infinite indicating a plane wavefront. Now using equation 2.9 and equation 2.10 , we get

$$\frac{A(z)}{A(0)} = \frac{1 + \frac{j\lambda z}{\pi w_0^2}}{1 + \left( \frac{\lambda z}{\pi w_0^2} \right)^2} \quad (2.17)$$

Now by replacing  $\tan \phi_0 = \left( \frac{\lambda z}{\pi w_0^2} \right)$ , we introduce a new term called phasor  $\phi_0$  that

corresponds to Gaussian beam phase shift. Based on the parameters that define the Gaussian beam behavior, the complete expression for the fundamental Gaussian beam mode can be given as

$$u(r, z) = \frac{w_0}{w} \exp \left[ \frac{-r^2}{w^2} - \frac{-j\pi r^2}{\lambda R} + j\phi_0 \right]. \quad (2.18)$$

An equation for E-field can be obtained using equation 2.18 in equation 2.3 and can be given as

$$E(r, z) = \left( \frac{w_0}{w} \right) \exp \left[ \frac{-r^2}{w^2} - jkz - \frac{-j\pi r^2}{\lambda R} + j\phi_0 \right] \quad (2.19)$$

#### 2.4.2 Confocal distance

The parameters that describe the Gaussian beam can further be simplified when expressed in terms of the confocal distance ( $z_c$ ) which can be given as

$$z_c = \frac{\pi w_0^2}{\lambda} \quad (2.20)$$

The confocal distance is sometimes referred as Rayleigh range denoted as ( $Z_0$ ). Now using the definition of Rayleigh range, the Gaussian beam parameters can be written as

$$R = z + \frac{z_c^2}{z} \quad (2.21)$$

$$w = w_0 \sqrt{\left[ 1 + \left( \frac{z}{z_c} \right)^2 \right]} \quad (2.22)$$

$$\phi_0 = \tan^{-1} \left( \frac{z}{z_c} \right) \quad (2.23)$$

Equations 2.21, 2.22 and 2.23 describes the behavior of Gaussian beam at all distances starting from beam waist. If  $z \ll z_c$ , then the beam is propagating in to a near field and if  $z \gg z_c$  the beam is propagating in to a far field. At the beam waist the beam radius has its minimum value  $w_0$  and this is where the E-field distribution is mostly concentrated. E-field and power distributions have their maximum on-axis values at this position. The radius of curvature is infinite at this location (indicating plane wave), phase shift is zero. Away from the beam waist, the beam radius increases monotonically.

## 2.5 Fundamental mode Gaussian beam and Edge taper

The fundamental Gaussian beam mode has a Gaussian distribution of the E-field perpendicular to the axis of propagation which can be given as

$$\frac{|E(r, z)|}{|E(0, z)|} = \exp \left[ - \left( \frac{r}{w} \right)^2 \right] \quad (2.24)$$

where  $r$  is the distance from the propagation axis. The power density distribution is proportional to the square of the quantity in equation 2.24 and can be given as

$$\frac{|P(r)|}{|P(0)|} = \exp \left[ - 2 \left( \frac{r}{w} \right)^2 \right] \quad (2.25)$$

Since the basic description of the Gaussian beam is in terms of its E-field distribution, the width of the E-field distribution can be used to characterize the beam (even if the power distribution is directly measured). Therefore to characterize the beam in terms of relative power at a specified radius, the edge taper ( $T_e$ ) is defined, which is given as

$$T_e = \frac{P(r_e)}{P(0)} \quad (2.26)$$

Using equation 2.26 in equation 2.25 and expressing the whole quantity in terms of decibels (dB), we have

$$T_e(r_e) = \frac{10\alpha}{\ln(10)} \quad (2.27)$$

where  $\alpha=2(r_e/w)^2$ . From equation 2.27, edge taper for different values of  $r_e/w$  can be calculated [39] and the results are tabulated in table 2.1

## 2.6 Paraxial limit

The paraxial approximation is a well-defined satisfactory approach to approximate the complete wave equation, only for reasonably well collimated beams. There is a limit on how much the paraxial wave equation is applicable before the Gaussian beam solutions are no longer valid. For a highly divergent beam the electric field distribution at the beam waist is concentrated within a small region, on the order of a wavelength or less. In such situations, the approximation that variations will occur

Table 2.1: Fundamental Gaussian Beam Mode and Edge Taper

$\frac{r_e}{w}$	$T_e(r_e)$	$T_e(dB)$
0	1.0000	0
0.2	0.9231	0.4
0.4	0.7262	1.4
0.6	0.4868	3.1
0.8	0.2780	5.6
1	0.1353	8.7
1.2	0.0561	12.5
1.4	0.0198	17.0
1.6	0.0060	22.2
1.8	0.0015	28.1
2	0.0003	34.7
2.2	0.0001	42

on a scale that is large compared to a wavelength is unlikely satisfactory. In fact a solution to the wave equation cannot have transverse variations on such a small scale and still have an E-field that is purely transverse to the axis of propagation. Also it is practically impossible to have an E-field that is purely linearly polarized. Hence when a beam waist that is of the order of a wavelength, the solution for the electric field has longitudinal and cross-polarized components. In addition, the beam size variation and amplitude as a function of distance from the beam waist do not follow the basic Gaussian beam formulas. As indicated in [39], if a Gaussian beam is forced at the waist to a fundamental mode, the beam diverges more rapidly than expected from a general Gaussian beam equations and on axis amplitude decreases more rapidly and the phase is also affected. [39] defines four different regimes for making appropriate paraxial approximations as shown in table.

Table 2.2: Paraxial limit approximation

$w_0/\lambda$	Paraxial approximation
$\geq 0.9$	valid
$\geq 0.5$ and $\leq 0.9$	valid with limitations
$\geq 0.25$ and $\leq 0.5$	valid with limitations
$< 0.25$	Not valid

In this chapter literature review on non-reciprocal signal processing components , Gaussian beam derivation, FMNWs based devices and magnetoelastic materials are discussed. In the next chapter material fabrication of ferromagnetic nanowired material and magnetoelastic material will be discussed.

## CHAPTER III

### MATERIAL GROWTH

This chapter focuses on the techniques used to grow FMNWs and magnetoelastic materials. FMNWs are nickel nanowires embedded in polycarbonate template and the magnetoelastic material is silicone rubber embedded with nickel microparticles. The nanowires were deposited in to the nanoporous templates using three electrode electrodeposition technique and the silicone rubber embedded with nickel microparticles was grown on an Electromagnetic Processing (EMP) line.

#### 3.1 Template based approach of growing nanowires

There are many physical deposition techniques available in the literature for growing one dimensional nanowires. One of the most straight forward techniques is the template based approach. In this method, nanowires are electrochemically grown inside a template. A template in this context refers to a material that has pores of diameter of the order of nanometers. The templates used in our experiments are commercially available nanoporous polycarbonate (PC) templates which are typically used as biological filters in separating different species such as polymers, molecules, salts etc. [40]. Among template based techniques, electrodeposition is the most preferred technique as it offers more advantages in terms of vacuum equipment, handling

capability and higher deposition rates. There are many parameters such as temperature, agitation, substrate properties, cleaning procedure etc. that play a significant role in electrodeposition of nanowires in to template [40]. Hence, these parameters have to be strictly considered during deposition. In general electrodeposition of a metal is done using two conductive electrodes and a reference electrode (a reference electrode is used in order to maintain a constant potential between the conductive electrodes). An electric potential is applied between the electrodes and thereby an electrical connection is created between the conducting electrodes. The current flows in the cell, an oxidation reaction occurs at anode and a reduction reaction occurs at cathode. This process can be either three electrode potentiostatic (constant voltage) or galvanostatic (constant current). The three-electrode technique is the most commonly used electrochemical cell in electrochemistry. As the name suggests this technique uses three electrodes a) Working Electrode (WE) b) Reference Electrode (RE) c) Counter Electrode (CE). Fig. 3.1 shows the schematic of three electrode potentiostatic technique.

### 3.1.1 Experimental demonstration of electrodeposition

Fig. 3.2 shows the photograph of three electrode potentiostatic technique. As mentioned before, electrodeposition technique [9] has been used to synthesize artificial ferrites consisting of nickel nanowires embedded in commercially available polycarbonate membrane filters. The templates (track-etched membrane filters) are approximately 25 mm in diameter and 30  $\mu\text{m}$  in thickness and have pore size of 100 nm. The

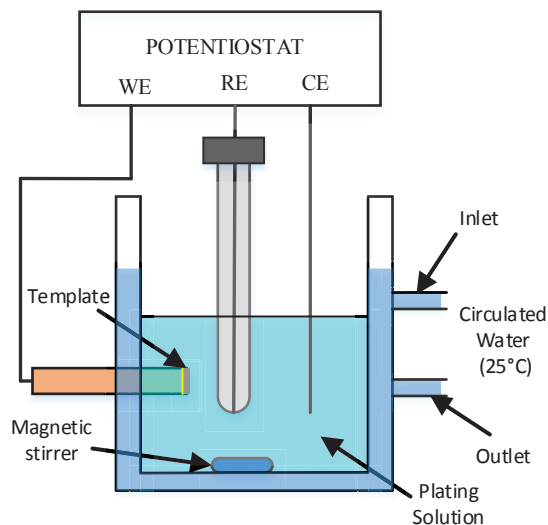


Figure 3.1: Schematic of electrodeposition setup

deposition process began with sputtering a sacrificial gold thin film on the back-side of the polycarbonate template. Fig. 3.3 (a) and Fig. 3.3 (b) and shows the polycarbonate template before and after gold sputtering. The gold sputtered polycarbonate template was then attached to an aluminum rod which is covered with a custom made hollow cylindrical Teflon cell as shown in Fig. 3.4. The entire set-up serves as a WE. The WE was placed in a ultrasonic bath for five minutes to remove air bubbles inside the sputtered nanoporous template. The CE is nickel wire and reference electrode is a saturated silver chloride electrode (AgCl/KCl). The deposition of nanowires into the pores was initiated by applying a potential between the WE and a CE with respect to a RE in Watts nickel plating solution. The deposition was carried out at a potential of  $-1.1$  V for 1200 seconds at  $25^{\circ}\text{C}$  with continuous magnetic stirring at 500 rpm. The deposition process was monitored using current vs time plot recorded

during deposition of nanowires in to the template. The current during the deposition process demonstrates several stages during the deposition.



Figure 3.2: Photograph of three electrode electrodeposition technique

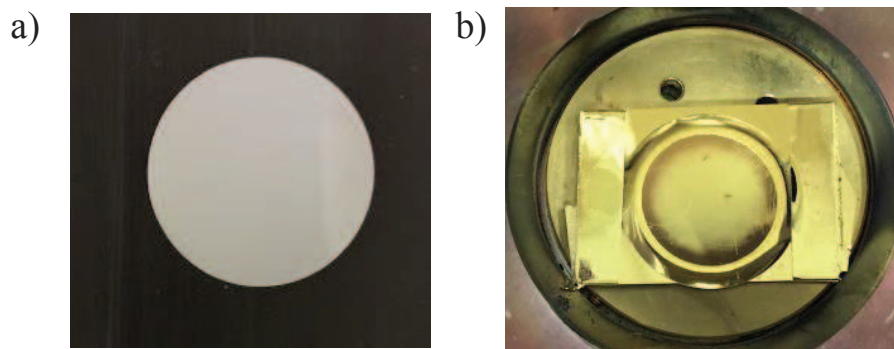


Figure 3.3: Polycarbonate template (a) before gold sputtering (b) after gold sputtering

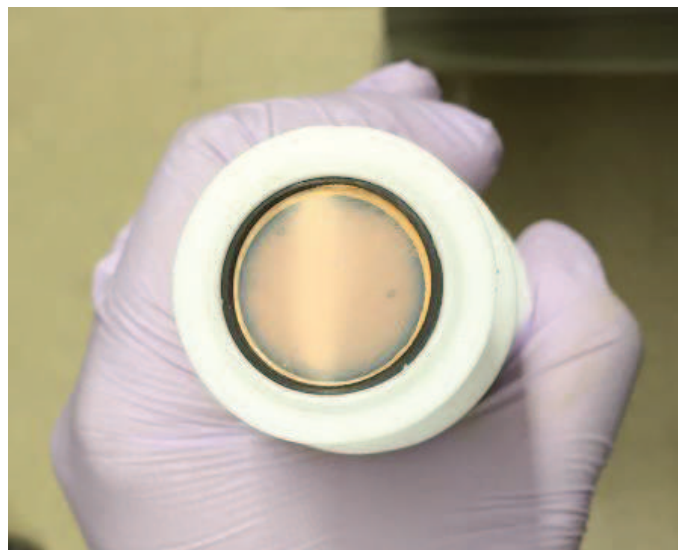


Figure 3.4: Working electrode used in electrodeposition

### 3.1.2 Different stages in electrodeposition

Fig. 3.5 shows the schematic of different stages in electrodeposition. The initial stage in the deposition is the nucleation phase where the seeding of the metal takes place inside the sputtered nanoporous template. The second stage is the in-pore growth. The actual deposition of the metal in to the pores takes place in this phase. The third stage is hemispherical cap overgrowth where there is a rapid increase in deposition of metal in the pores forming a hemispherical cap structure. The formation of hemispherical caps results in steady increase in current and the hemispherical caps amalgamate into a continuous metallic layer. At this point, the current reaches a constant value indicating film overgrowth. This is the final stage of deposition. Fig. 3.6 shows the current monitored during different stages of electrodeposition [41]. Fig.

3.7 shows the SEM image of the in-pore deposited nickel nanowires. Fig. 3.8 shows the SEM image of the hemispherical cap nickel nanowires. Fig. 3.9 shows the SEM image of the overgrowth of nickel nanowires. All the three SEM images ( Fig. 3.7, Fig. 3.8, Fig. 3.9) were taken after nanowires were liberated from the polycarbonate template and with gold coating removed.

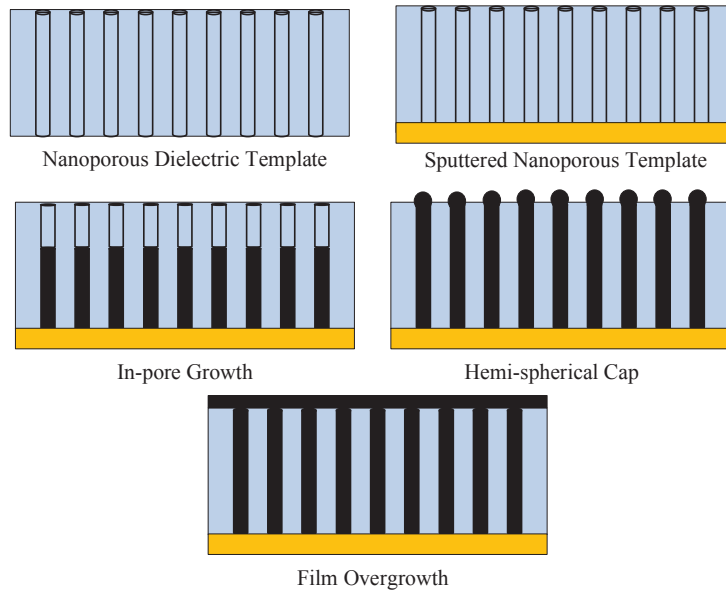


Figure 3.5: Schematic of stages in electrodeposition process

In the hemispherical cap overgrowth and film overgrowth stages, the electrodeposited material has high resistance and hence to use FMNWs as artificial ferrites, in-pore growth is recommended. Fig. 3.10 shows the current monitored in different electrodeposition experiments. From these experiments it is clear that the in-pore deposition is possible for deposition time greater than 100 seconds and less than 2000 sec. Hence the deposition time was restricted to 1200 sec. Fig. 3.11 shows

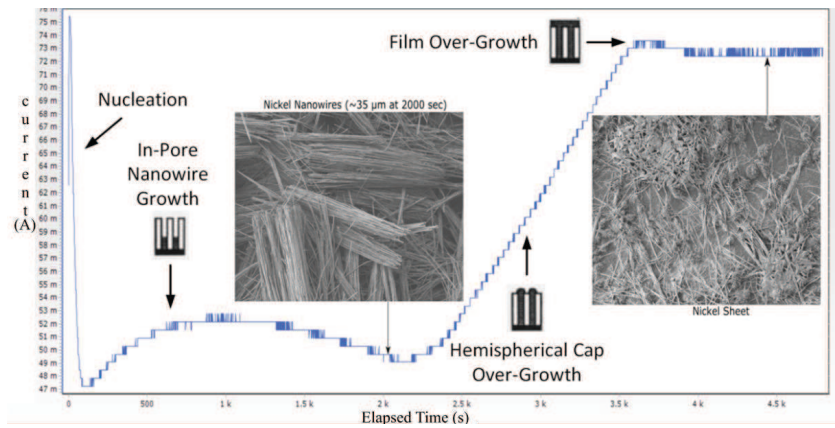


Figure 3.6: Graph showing different stages of electrodeposition from current monitored during the process

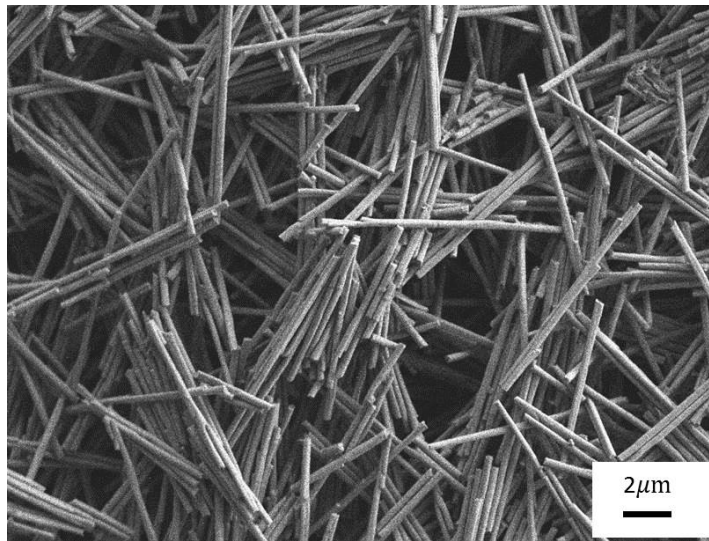


Figure 3.7: SEM image of nanowires in second stage of deposition

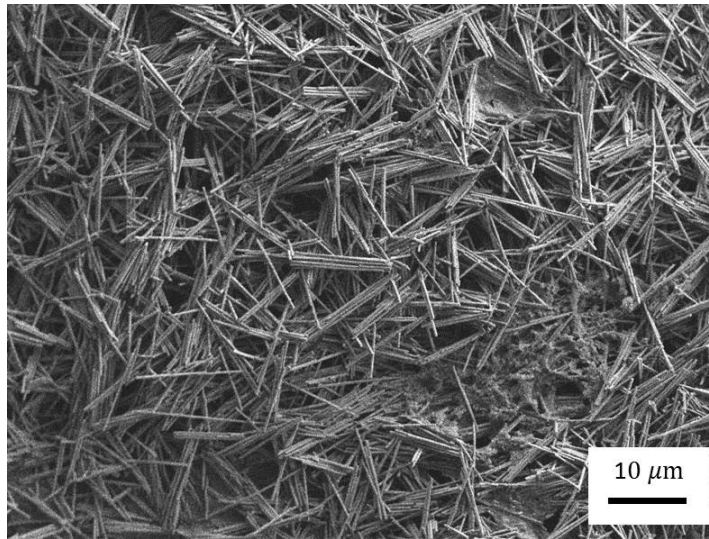


Figure 3.8: SEM image of nanowires in third stage of deposition

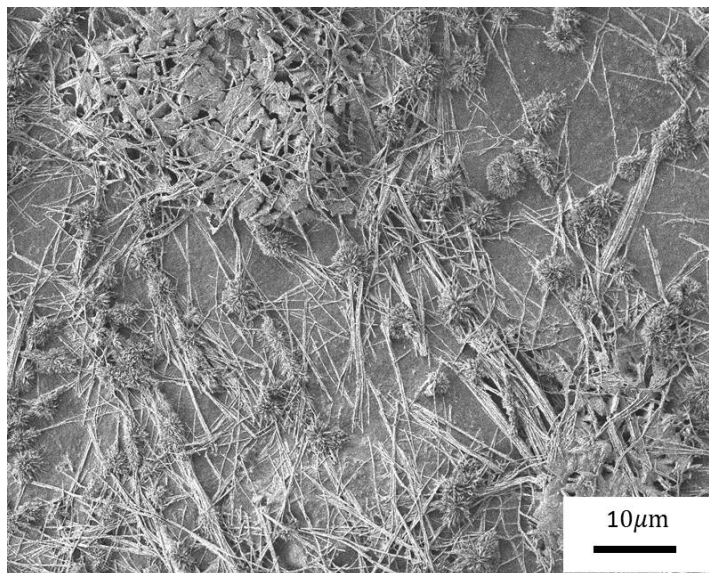


Figure 3.9: SEM image of nanowires in the fourth stage of deposition

the current monitored during the in-pore growth.

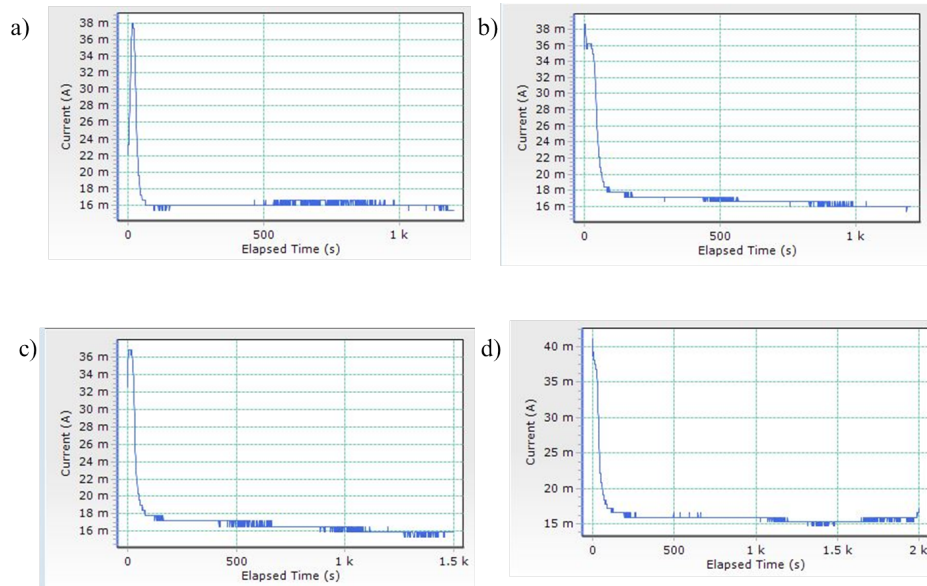


Figure 3.10: Experiments performed to identify the in-pore growth stage

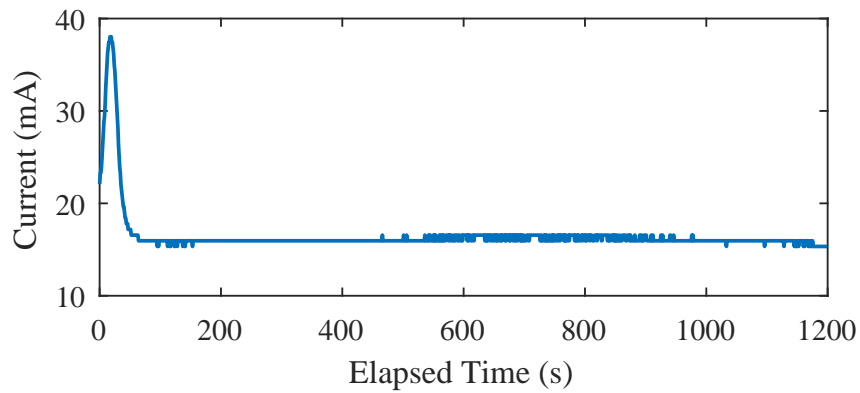


Figure 3.11: Current monitored during the in-pore growth

Following the electrodeposition, the back-side gold coating was removed using gold etchant obtained from Transene, Inc. and the gold removed sample was used as

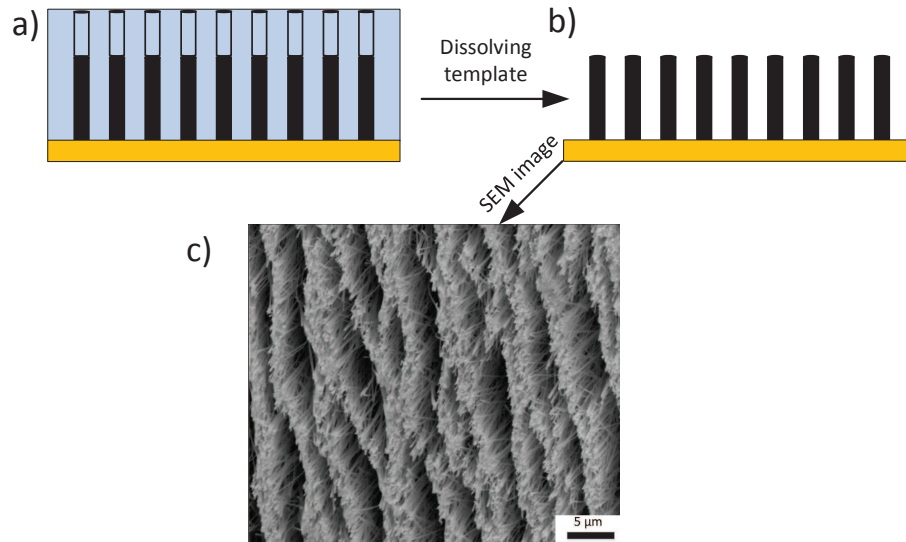


Figure 3.12: SEM image of nickel nanowires after dissolving polycarbonate template (attached to gold).

material under test (MUT) in the experiments. Fig. 3.12 shows the nanoporous templates after electrodeposition and a Scanning Electron Microscope (SEM) micrograph featuring nickel nanowires that have been liberated from the polycarbonate template but remained attached to the sacrificial gold thin film. From the SEM image, the nanowires were found to have lengths of approximately  $3.5 \mu\text{m}$ .

### 3.2 Magnetoelastic material

Another type of material used for the experiments is Polydimethylsiloxane (PDMS or silicone rubber) infused with nickel microparticles. The material was used to demonstrate tunable Faraday rotation by modulating the nickel microparticle density. In order to modulate the nickel microparticle density, the material used in conjunction

with nickel microparticles should be easily stretchable (low Young's Modulus) and hence silicone rubber with nickel microparticles was chosen. The material was grown on the EMP line at the National polymer innovation center (NPIC) at the University of Akron. PDMS is Dow Corning Sylgard 184 and nickel particles are Novamet Type 123. Fig. 3.13 shows the SEM image of the nickel particles [42]. The particle size varies from  $3\mu\text{m}$  to  $6\mu\text{m}$ . nickel powders were mixed with PDMS base and curing agent(10:1) by using a vacuum planetary mixer (Thinky ARV-310). PDMS/Ni films were fabricated by continuously blade-coating the mixture onto a PET substrate (Mylar A) carried by the roll-to-roll processing on the EMP line. Fig 3.14 shows the schematic of EMP line [43].

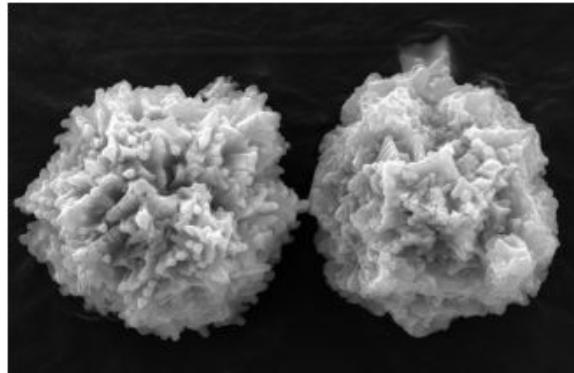


Figure 3.13: SEM image of Novamet Type 123 nickel particles

The nickel particles were randomly dispersed in the polymer solution (PDMS) on a roller belt and were passed between the poles of the electromagnet that arranges these particles in vertical chains. The presence of magnetic field makes each nickel particle in the solution to magnetize in the field direction. Since all the dipoles are

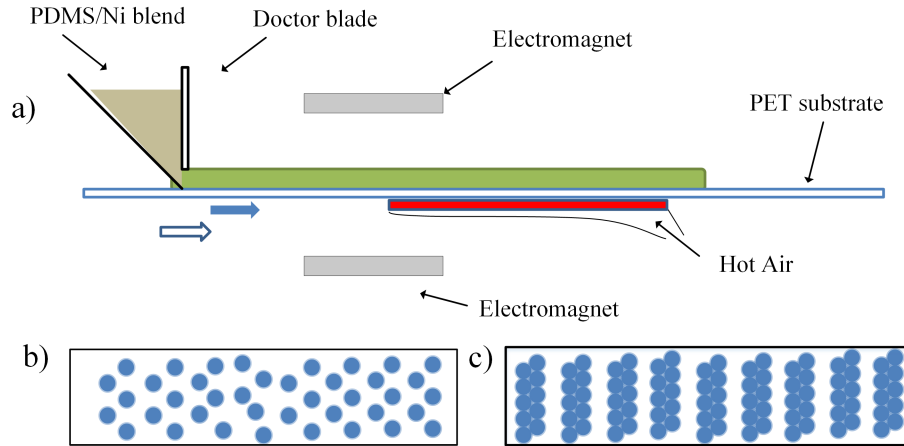


Figure 3.14: a) Schematic of EMP line. Side view of Ni microparticles embedded in PDMS membrane (b) before and (c) after passing through a high magnetic field.

arranged in the magnetic field direction, the particles repel in transverse direction and attract each other in field direction. The chains, thus formed in the direction of thickness of PDMS membrane increase with increasing magnetic field (until saturation of nickel particles), are responsible for electrical conductivity. An SEM image of the nickel microparticles infused in silicone rubber is shown in Fig. 3.15. The visible dots in the SEM image are the nickel microparticles.

As mentioned in Chapter 1, the material was used to exhibit inverse magnetostrictive effect from which tunable Faraday rotation may be obtained. In order to do so, a sample of this material was taken and fixed with silicone tire glue to a piezoelectric crystal with annular shape. The crystal dimensions included an outer radius of 40 mm and an inner radius of 20 mm and a thickness of 5 mm. The piece of material attached to the piezoelectric crystal is another MUT and serves as magnetoelastic material. Fig. 3.16 shows the concept of inverse magnetostrictive effect

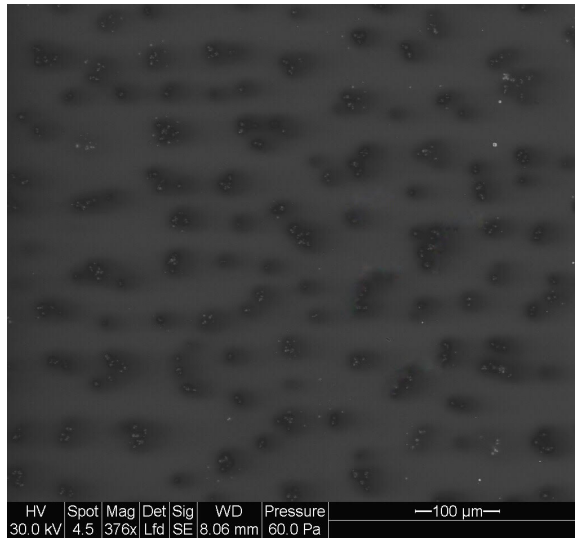


Figure 3.15: SEM image of silicone rubber infused with nickel microparticles

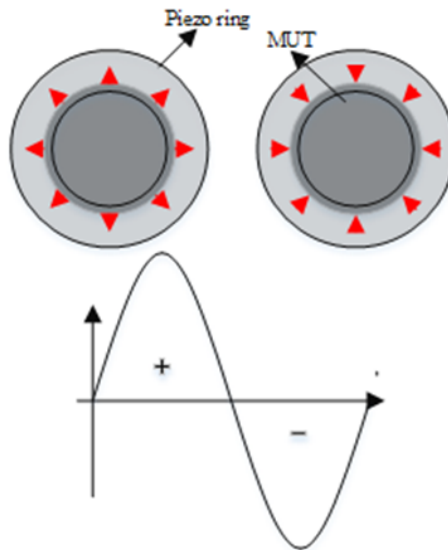


Figure 3.16: Demonstration of inverse magnetostriction effect

using the material attached to a piezoelectric crystal. The idea here is to operate the piezoelectric crystal at its radial resonant frequency which modulates the nickel microparticle density (due to radial displacement of the piezoring). The piezoelectric crystal used in our work is PZT 880. The radial resonant frequency of the piezocrystal can be given as

$$f_{rad} = N_{ring}/(OD - ID) \quad (3.1)$$

where  $N_{ring}$  is called frequency constant (depends up the type of the material), OD is the outer diameter of the piezoring and ID is the inner diameter of the piezoring. By substituting all these values in equation 3.1, theoretical value for radial resonant frequency was found to be  $f_{rad} = 106$  kHz.

The chapter discussed the growth of the materials that will be used as MUT in Faraday rotation experimental measurements. In the next chapter a mathematical expression for calculating Faraday rotation in thin films will be derived.

## CHAPTER IV

### SMALL ANGLE FARADAY ROTATION

In the previous chapter, FMNWs and magnetoelastic material growth were discussed. In this chapter a generalized mathematical equation, that can be used to calculate Faraday rotation in these materials was derived using Stokes polarization parameters and Mueller matrix analysis.

#### 4.1 Stokes polarization parameters

The polarization behavior could be represented in terms of observables. Any state of polarized EM wave can be described by four measurable real quantities known as Stokes polarization parameters. These were first described by Sir George Gabriel Stokes. The very first parameter gives the information on the total intensity of the EM wave while the remaining three parameters describe polarization state of the EM wave.

##### 4.1.1 Arbitrarily polarized EM wave

If  $E_{0x}$  and  $E_{0y}$  are the amplitudes of the horizontal and vertical components of the propagating EM wave, the Stokes polarization parameters for an arbitrarily polarized EM wave ( $S_{AP}$ ) in vector form can be given as [44]

$$S_{AP} = \begin{bmatrix} S_0 \\ S_1 \\ S_2 \\ S_3 \end{bmatrix} = \frac{1}{2} \begin{bmatrix} E_{0x}^2 + E_{0y}^2 \\ E_{0x}^2 - E_{0y}^2 \\ 2E_{0x}E_{0y} \cos \delta \\ 2E_{0x}E_{0y} \sin \delta \end{bmatrix}, \quad (4.1)$$

where  $S_0$  is the total intensity of the EM wave,  $S_1$  describes the total amount of linear horizontal and vertical polarization,  $S_2$  describes the total amount of linear  $+45^\circ$  and  $-45^\circ$  polarization,  $S_3$  describes the total amount of right or left circular polarization and  $\delta$  is phase factor.

#### 4.1.2 Linearly horizontal polarized EM wave

For a linearly horizontal polarized EM Wave,  $E_{0y}=0$  and hence the Stokes parameters in vector form can be given as [44]

$$S_H = \begin{bmatrix} S_0 \\ S_1 \\ S_2 \\ S_3 \end{bmatrix} = \frac{1}{2} \begin{bmatrix} E_{0x}^2 \\ E_{0x}^2 \\ 0 \\ 0 \end{bmatrix} \quad (4.2)$$

#### 4.1.3 Linearly vertical polarized EM wave

For a linearly vertical polarized EM Wave,  $E_{0x}=0$  and hence the Stokes parameters can be simplified as [44]

$$S_V = \begin{bmatrix} S_0 \\ S_1 \\ S_2 \\ S_3 \end{bmatrix} = \frac{1}{2} \begin{bmatrix} E_{0y}^2 \\ -E_{0y}^2 \\ 0 \\ 0 \end{bmatrix} \quad (4.3)$$

#### 4.1.4 Linearly 45° polarized EM wave

The conditions to obtain a linearly 45° polarized EM Wave are  $E_{0x}=E_{0y}=E_0$  and  $\delta=0$ . Using these conditions in the unpolarized EM wave Stokes equations, we find that

$$S_{45} = \begin{bmatrix} S_0 \\ S_1 \\ S_2 \\ S_3 \end{bmatrix} = \frac{1}{2} \begin{bmatrix} 2E_0^2 \\ 0 \\ 2E_0^2 \\ 0 \end{bmatrix} \quad (4.4)$$

## 4.2 Mueller matrices for polarizing components

The Mueller matrix is the matrix representation of Stokes parameters for studying the interaction of the EM wave with different materials. Fig.4.1 shows an input incident beam interacting with a polarizing element which results in an emerging output beam. As mentioned before, any EM wave can be characterized by Stokes parameters, as in this case the incident beam is characterized by Stokes parameters ( $S_0, S_1, S_2$  and  $S_3$ ) and therefore the emerging output beam is also characterized by a new set of Stokes

parameters ( $S'_0, S'_1, S'_2$  and  $S'_3$ ). The relationship between these two parameters can be explained by assuming the output beam is a linear combination of the four Stokes parameters of the input beam by

$$S'_0 = m_{00}S_0 + m_{01}S_1 + m_{02}S_2 + m_{03}S_3, \quad (4.5)$$

$$S'_1 = m_{10}S_0 + m_{11}S_1 + m_{12}S_2 + m_{13}S_3, \quad (4.6)$$

$$S'_2 = m_{20}S_0 + m_{21}S_1 + m_{22}S_2 + m_{23}S_3, \quad (4.7)$$

$$S'_3 = m_{30}S_0 + m_{31}S_1 + m_{32}S_2 + m_{33}S_3. \quad (4.8)$$

The four equations in matrix form can be given as

$$\begin{bmatrix} S'_0 \\ S'_1 \\ S'_2 \\ S'_3 \end{bmatrix} = \begin{bmatrix} m_{00} & m_{01} & m_{02} & m_{03} \\ m_{10} & m_{11} & m_{12} & m_{13} \\ m_{20} & m_{21} & m_{22} & m_{23} \\ m_{30} & m_{31} & m_{32} & m_{33} \end{bmatrix} \begin{bmatrix} S_0 \\ S_1 \\ S_2 \\ S_3 \end{bmatrix}. \quad (4.9)$$

This  $4 \times 4$  matrix is termed as Mueller matrix.

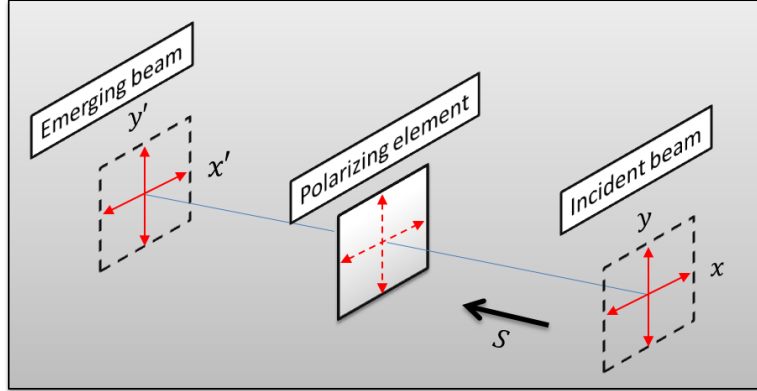


Figure 4.1: Interaction of polarized EM wave with a polarizing element

#### 4.2.1 Mueller matrix of a polarizer

A polarizer is an optical element that attenuates the orthogonal components of a beam unequally. Fig. 4.2 shows a polarized beam incident on a polarizer along with the emerging output beam. The horizontal attenuation coefficient of the polarizer is given by  $p_x$  while the vertical attenuation coefficient is given by  $p_y$ . After the beam emerges from the polarizer, the amplitudes of the horizontal and vertical components are represented by  $E_{x'}$  and  $E_{y'}$ . The relationship between incident and emerging beam can be given as

$$E'_{x'} = p_x E_x \quad (4.10)$$

and

$$E'_{y'} = p_y E_y. \quad (4.11)$$

In case of no attenuation, the values of  $p_x$  and  $p_y$  are one. In case of a 100% attenuation, the values of  $p_x$  and  $p_y$  are zero. In this case the Stokes polarization

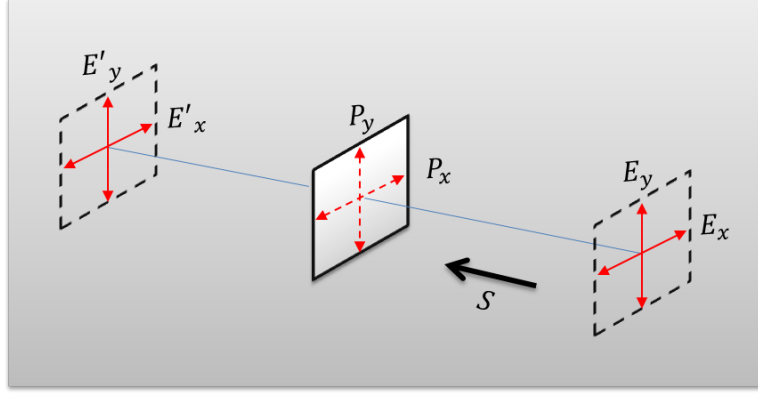


Figure 4.2: Mueller matrix of a polarizer with attenuation coefficients  $p_x$  and  $p_y$

parameters of the incident and emerging output beams are given as

$$S_0 = E_x E_x^* + E_y E_y^*, \quad (4.12)$$

$$S_1 = E_x E_x^* - E_y E_y^*, \quad (4.13)$$

$$S_2 = E_x E_y^* + E_y E_x^*, \quad (4.14)$$

$$S_3 = i(E_x E_y^* - E_y E_x^*), \quad (4.15)$$

and

$$S'_0 = E'_x E_x^* + E'_y E_y^*, \quad (4.16)$$

$$S'_1 = E'_x E'_x{}^* - E'_y E'_y{}^*, \quad (4.17)$$

$$S'_2 = E'_x E'_y{}^* + E'_y E'_x{}^*, \quad (4.18)$$

$$S'_3 = i(E'_x E'_y{}^* - E'_y E'_x{}^*). \quad (4.19)$$

Here  $E^*$  and  $E'^*$  are the complex conjugates. Substituting equations 4.10 and 4.11 in 4.16 to 4.19 and using equations 4.12 to 4.15, the resultant Mueller matrix can be given as

$$\begin{bmatrix} S'_0 \\ S'_1 \\ S'_2 \\ S'_3 \end{bmatrix} = \frac{1}{2} \begin{bmatrix} p_x^2 + p_y^2 & p_x^2 - p_y^2 & 0 & 0 \\ p_x^2 - p_y^2 & p_x^2 + p_y^2 & 0 & 0 \\ 0 & 0 & 2p_x p_y & 0 \\ 0 & 0 & 0 & 2p_x p_y \end{bmatrix} \begin{bmatrix} S_0 \\ S_1 \\ S_2 \\ S_3 \end{bmatrix} \quad (4.20)$$

Comparing this equation with 4.9 , the Mueller matrix for a polarizer can be given

as

$$M_{polarizer} = \frac{1}{2} \begin{bmatrix} p_x^2 + p_y^2 & p_x^2 - p_y^2 & 0 & 0 \\ p_x^2 - p_y^2 & p_x^2 + p_y^2 & 0 & 0 \\ 0 & 0 & 2p_x p_y & 0 \\ 0 & 0 & 0 & 2p_x p_y \end{bmatrix} \quad (4.21)$$

Substituting  $p_x=0$  and  $p_y=1$  in 4.21 gives the Mueller matrix of the vertical component (equation 4.23) of the EM wave ( $M_v$ ). Substituting  $p_y=0$  and  $p_x=1$  gives the Mueller matrix of the horizontal component of the EM wave ( $M_h$  (equation 4.22)

$$M_h = \frac{1}{2} \begin{bmatrix} 1 & 1 & 0 & 0 \\ 1 & 1 & 0 & 0 \\ 0 & 0 & 0 & 0 \\ 0 & 0 & 0 & 0 \end{bmatrix} \quad (4.22)$$

$$M_v = \frac{1}{2} \begin{bmatrix} 1 & -1 & 0 & 0 \\ -1 & 1 & 0 & 0 \\ 0 & 0 & 0 & 0 \\ 0 & 0 & 0 & 0 \end{bmatrix} \quad (4.23)$$

#### 4.2.2 Mueller matrix of a rotator

The polarization state of an EM wave can be changed by propagating the wave through a polarizing element that rotates the horizontal and vertical components of the E-field by an angle  $\theta$ . The Mueller matrix for a polarizing rotator can be obtained by applying the same analysis in the section 4.2.1. Fig. 4.3 shows rotation of an EM field by a rotator. The angle  $\theta$  describes the rotation of  $E_x$  to  $E'_x$  and  $E_y$  to  $E'_y$ . The angle  $\beta$  is the angle between the E-field (E) and horizontal component of the E-field  $E_x$ . The point P can be described as

$$E'_x = E \cos(\beta - \theta), \quad (4.24)$$

$$E'_y = E \sin(\beta - \theta). \quad (4.25)$$

Similarly, the horizontal and vertical components of the E-field can be given as

$$E_x = E \cos \beta, \quad (4.26)$$

$$E_y = E \sin \beta, \quad (4.27)$$

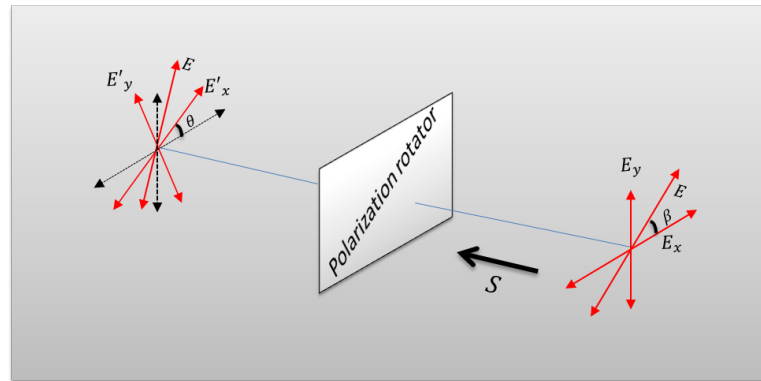


Figure 4.3: Polarization rotator

As described in the previous sections, the Mueller matrix for a polarization rotator can be given as

$$M_R = \begin{bmatrix} 1 & 0 & 0 & 0 \\ 0 & \cos(2\theta) & \sin(2\theta) & 0 \\ 0 & -\sin(2\theta) & \cos(2\theta) & 0 \\ 0 & 0 & 0 & 1 \end{bmatrix} \quad (4.28)$$

### 4.3 Analytical expression for calculating Faraday rotation

The analytical expression for Faraday rotation can be obtained by using Mueller matrix and Stokes parameters. A  $45^\circ$  linearly polarized EM wave is passed through a polarizing rotator (whose Faraday rotation needs to be determined). Assuming the beam was split in to its horizontal and vertical components individually as shown in Fig. 4.4 and Fig. 4.5, a mathematical expression for Faraday rotation can be derived. The Stokes vector of the EM wave in horizontal direction is

$$S_H = M_h M_R S_{45} \quad (4.29)$$

The Stokes vector of the EM wave in vertical direction is

$$S_V = M_v M_R S_{45} \quad (4.30)$$

Considering only the intensity component (first element) of the Stokes vector for both horizontal and vertical components and simplifying, we get

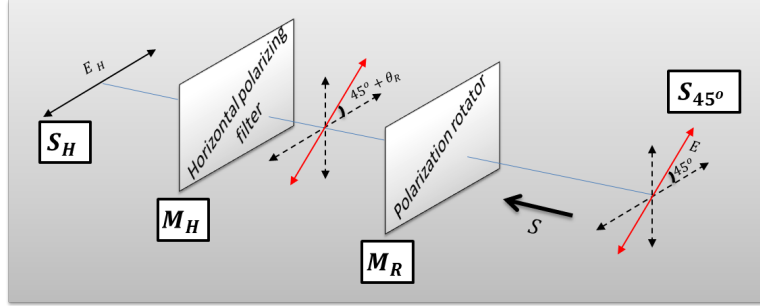


Figure 4.4: Horizontal component of E-field

$$|\cos(n\theta_R)\sin(n\theta_R)| = \frac{\langle V_h - V_v \rangle}{(\langle V_H \rangle + \langle V_V \rangle)} \quad (4.31)$$

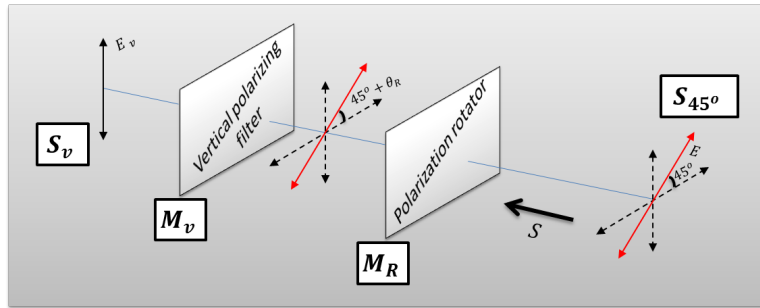


Figure 4.5: Vertical component of E-field

Using the small angle approximation, the Faraday rotation angle can be given

as

$$\theta_R = \frac{\langle V_h - V_v \rangle}{n(\langle V_H \rangle + \langle V_V \rangle)} \quad (4.32)$$

where  $n$  is the number of passes through the Faraday rotator,  $\langle V_h - V_v \rangle$  is the difference

of the average value of the intensity of horizontal and vertical components,  $\langle V_H \rangle$  and  $\langle V_V \rangle$  are the average value of the intensity of horizontal and vertical components of the EM wave. Equation 4.32 was used to calculate the Faraday rotation in FMNWs and magnetoelastic materials.

## CHAPTER V

### DESIGN OF 3D PRINTED AND QUASIOPTICAL COMPONENTS

In the previous chapter, a mathematical expression for small angle Faraday rotation was derived. In order to implement this equation practically, Gaussian beam has to be manipulated to eliminate the effect of birefringence in the measurements. This chapter discusses the design and construction of all 3D printed and quasioptical components such as dielectric lens, mirror, 3D-printed sample holder and beam splitter. The term quasioptics refer to the propagation of EM wave when wavelength is comparable to the size of the optical components

#### 5.1 Ray matrix analysis

The similarity between the complex beam parameter and radius of curvature suggests that quasioptical systems can be analyzed in terms of their effective complex beam parameter analogous to rays in a linear geometrical optics system. In this approach, the location and slope of the output plane of a paraxial system ( $r'_{out}$ ) are defined to be linear functions of the parameters of the input ray ( $r_{in}$ ). The relationship between input plane and output plane of the paraxial system can be given as

$$\begin{bmatrix} r_{out} \\ r'_{out} \end{bmatrix} = \begin{bmatrix} A & B \\ C & D \end{bmatrix} \begin{bmatrix} r_{in} \\ r'_{in} \end{bmatrix}. \quad (5.1)$$

In general the radius of curvature is defined as  $R = \frac{r}{r'}$ . Using equation 5.1 the radius of curvature can be given as

$$R_{out} = \frac{AR_{in} + B}{CR_{in} + D} \quad (5.2)$$

The same approach is applied to Gaussian beams, which leads to ABCD law in quasioptical systems. The radius of curvature in equation 5.2 is now replaced with a complex beam parameter

$$q_{out} = \frac{Aq_{in} + B}{Cq_{in} + D}. \quad (5.3)$$

The ABCD law is one of the significant tools in analysis of a quasioptical system, since the entire geometrical optics ray theory can be applied to Gaussian beam representation of a system. In all of the analysis, the rays are assumed to be incident from the left. We obtain the matrix representing the effects of a sequence of elements by multiplying the respective ABCD matrices. The analysis is done from left to right starting with first element encountered by the beam and multiplying by the matrix for each subsequent element placed on the left. A complex beam parameter at the system output is then obtained.

The most basic ray transfer matrix is that for a distance  $L$  of propagation in a uniform material of uniform index of refraction. The ray transfer matrix is given as [39]

$$M_{dist} = \begin{bmatrix} 1 & L \\ 0 & 1 \end{bmatrix}. \quad (5.4)$$

A second fundamental ray transfer matrix is the interface between media of different indices of refraction ( $n_1$  and  $n_2$ ). Assuming the interface has radius  $R$ , the ray transformation matrix is given as [39]

$$M_{int} = \begin{bmatrix} 1 & 0 \\ \frac{n_2 - n_1}{n_2 R} & \frac{n_1}{n_2} \end{bmatrix} \quad (5.5)$$

## 5.2 Transformation by a general quasioptical system

Using the previously described matrix analysis, the transformational properties of quasioptical systems can be found using ABCD law. The situation illustrated in Fig. 5.1 consists of a waist located at input distance  $d_{in}$  where a quasioptical focusing element is placed. The beam is transformed and a new complex beam parameter is obtained at  $d_{out}$ . Any quasioptical system can be simplified by obtaining its overall ABCD matrix from cascaded representation of its constituent elements as follows

$$M_T = \begin{bmatrix} 1 & d_{out} \\ 0 & 1 \end{bmatrix} \begin{bmatrix} A & B \\ C & D \end{bmatrix} \begin{bmatrix} 1 & d_{in} \\ 0 & 1 \end{bmatrix} \quad (5.6)$$

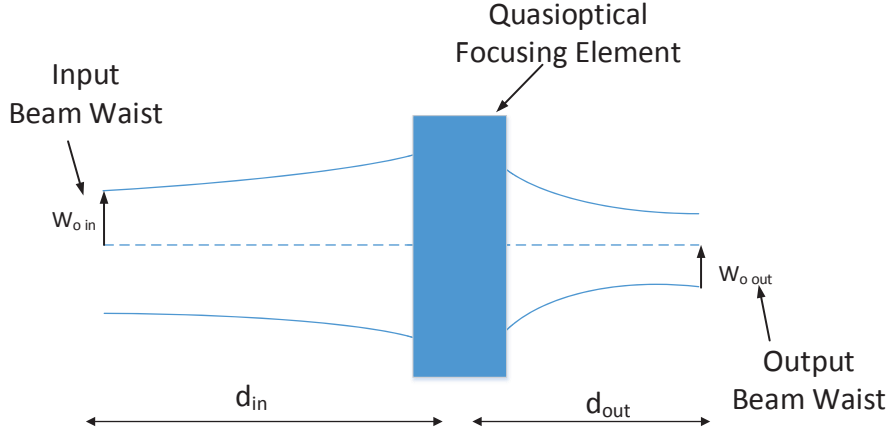


Figure 5.1: Transformation of a Gaussian beam using a quasioptical component

Now using equation 5.3 in equation 5.6 the complex beam parameter is

$$q_{out} = \frac{(A + Cd_{out})q_{in} + ((A + Cd_{out})d_{in} + (B + Dd_{out}))}{Cq_{in} + Cd_{in} + D}. \quad (5.7)$$

The parameters that define the output waist can be obtained by considering the fact that the complex beam parameter has both real and imaginary parts. By solving for the real part of  $q_{out}$  the distance to the output beam waist can be given as

$$d_{out} = \frac{(Ad_{in} + B)(Cd_{in} + D) + (ACZ_c^2)}{(Cd_{in} + D)^2 + (CZ_c)^2}. \quad (5.8)$$

The imaginary part of the expression can be found using determinant of  $ABCD=1$ .

This gives

$$w_{out} = \frac{w_{oin}}{[(Cd_{in} + D)^2 + (CZ_c)^2]^{0.5}}. \quad (5.9)$$

The equations 5.8 and 5.9 can be applied to any quasioptical system and to any Gaussian beam mode in paraxial limit. In this work, a Gaussian beam was transformed using dielectric lens and spherical mirror. The design of the lens system and spherical mirror are discussed in the next sections.

### 5.3 Design of dielectric lens

The Gaussian beam was transformed using dielectric lens. High density Polyethylene (HDPE) was used to fabricate the lens. Three different lenses were designed at 61.25 GHz to transform the Gaussian beam propagation. The three lenses were plano convex. The ABCD parameters for a lens of radius of curvatures  $R_1$  and  $R_2$ , thickness  $t_c$  of material having refractive index  $n_2$  embedded in material of index  $n_1$  can be given as

$$ABCD_{lens} = \begin{bmatrix} 1 + \frac{(n_2-n_1)t_c}{n_2R_1} & \frac{(n_1)t_c}{n_2} \\ \frac{-1}{f} - \frac{(n_2-n_1)^2t_c}{n_1n_2R_1R_2} & 1 + \frac{(n_1-n_2)t_c}{n_2R_2} \end{bmatrix}. \quad (5.10)$$

For a thick lens, focal length,  $f$  is given in equation 5.11 and central thickness is given in equation 5.12

$$\frac{1}{f} = \frac{n_2 - n_1}{n_1} \left( \frac{1}{R_2} - \frac{1}{R_1} \right), \quad (5.11)$$

$$t_c = \frac{f}{n + 1} \left[ \left( 1 + \frac{D^2}{4f^2} \right)^{0.5} - 1 \right]. \quad (5.12)$$

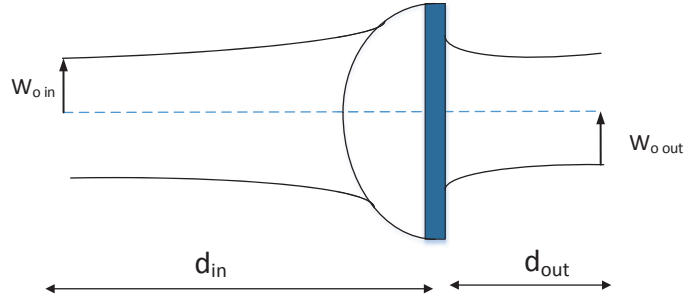


Figure 5.2: Transformation of a Gaussian beam by lens 1

The positions of the dielectric lenses were determined by using the analysis described in section 5.2. Lens 1 was used independently where as lens 2 and lens 3 were used conjointly. Fig 5.2 and Fig 5.3 shows the Gaussian beam transformation using these lenses. Table 5.1 and Table 5.2 summarizes the input and output parameters of the Gaussian beam due to the lens system. Fig. 5.4, Fig. 5.5 and Fig. 5.6 shows the 2D model drawings of these lens systems.

Table 5.1: Transformation parameters of Gaussian beam using lens 1

Parameters Values (in mm)	
$W_{oin}$	6
$d_{in}$	210
$W_{out}$	8
$d_{out}$	276

In figuring out the lens dimensions, the concept of beam truncation comes in to picture. The beam truncation can have harmful effects in addition to the power loss from the fundamental mode produced by the truncation itself. The truncation

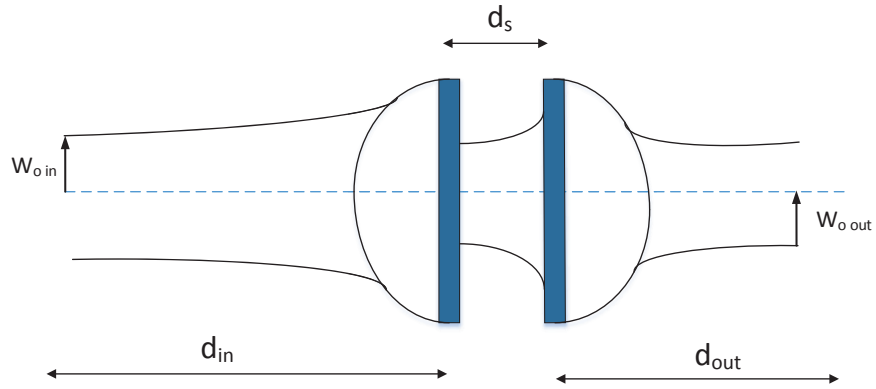


Figure 5.3: Transformation of a Gaussian beam by lens 2 and lens 3

Table 5.2: Transformation parameters of Gaussian beam using lens 2 and lens 3

Parameters Values (in mm)	
$W_{oin}$	8
$d_{in}$	209
$W_{out}$	9.6
$d_{out}$	121

particularly at a beam waist produces sidelobes in the far field. The situation becomes more complex in the near field of the beam waist as this results in non-Gaussian component of the beam. The exact effects of beam truncation in a quasioptical system are not easy to deal, as one quasioptical element producing decreased effective beam waist radius can be followed by another element in the near field which will have negligible effect. If the second element is in the far field, the effect will be increased as a result of larger beam divergence and beam size at the location of the second quasioptical element resulting from the first. The effects of beam truncation can be

eliminated by expanding the beam at each truncating element in terms of a set of Laguerre Gaussian beam modes and propagating each of them through the system [39]. In case of multiple apertures, the calculations become quite complex and this technique is not recommended.

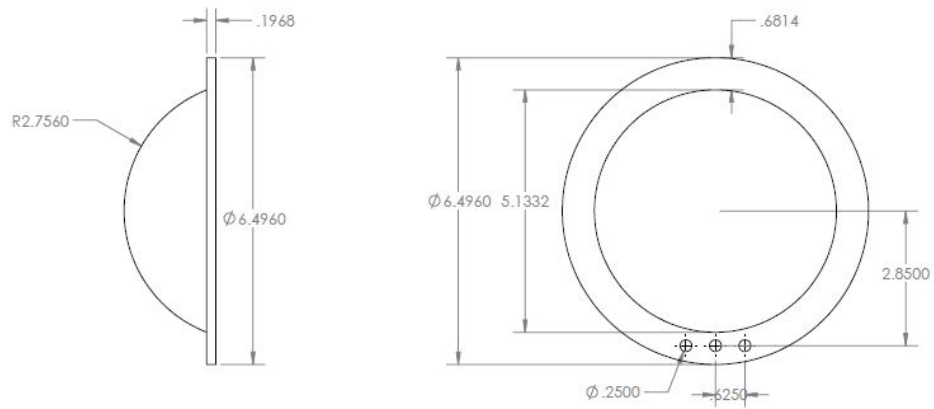


Figure 5.4: 2D model of lens 1 with dimensions

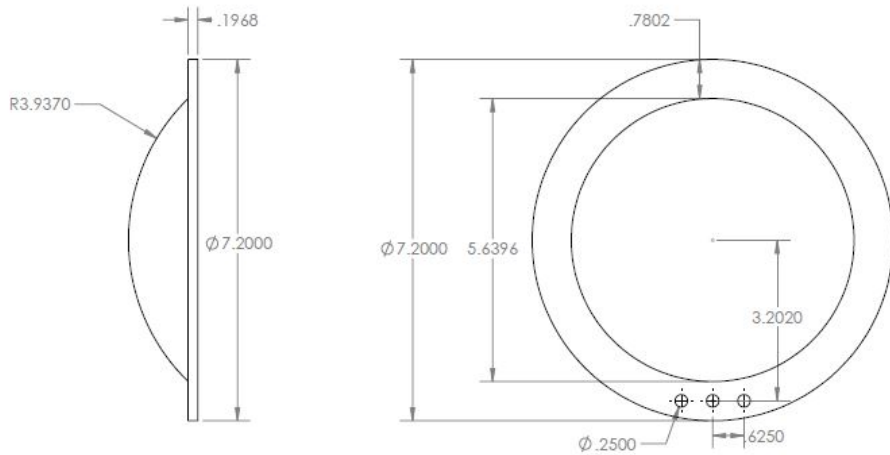


Figure 5.5: 2D model of lens 2 with dimensions

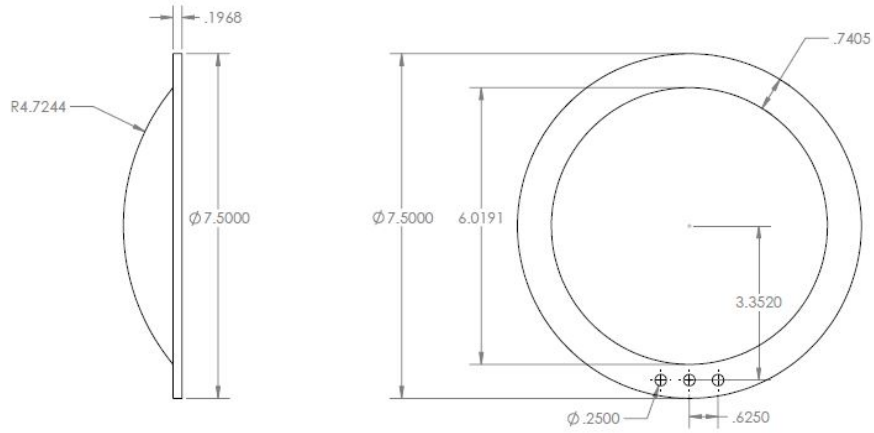


Figure 5.6: 2D model of lens 3 with dimensions

A simple approach but one that is justified by its successful use by many designers, is to handle truncation in a moderately conservative manner. Satisfactory results even in systems employing large number of quasioptical elements with minimum diameter of  $D_{min}=4w$ , where  $w$  is the beam radius at quasioptical element. This corresponds to a fractional power loss ( $P_{out}/P_{in}$ ) of  $3 \times 10^{-4}$  (W/W) and an edge taper of 35 dB. For simple systems,  $D_{min}=3w$  corresponding to a fractional power loss of 0.011 and an edge taper of 20 dB can be adopted. All the lenses were designed based up on this idea. Fig 5.4, Fig 5.5 and Fig 5.6 shows the 2D model of the lenses used along with the dimensions. Fig 5.7 shows the photograph of lens placed in a custom designed holder.



Figure 5.7: Photograph of the fabricated lens

#### 5.4 Design of spherical mirror

Another quasioptical component used for Gaussian beam transformation is spherical mirror. The main purpose of designing spherical mirror is to retrace the incoming Gaussian beam path so that the effect of birefringence is nullified. In order for the beam to retrace the path, the radius of curvature for the incoming Gaussian beam ( $R_{Ga}$ ) should be equal to the radius of curvature of the mirror( $R_s$ ). Fig. 5.8 illustrates the role of spherical mirror. The radius of curvature of the Gaussian beam is calculated using equation 2.21 in chapter 2. The mirror was designed using aluminum with radius of curvature ( $R_s$ ) of 300 mm. Fig. 5.9 shows the 2D model of the spherical mirror with dimensions and Fig. 5.10 shows the photograph of the spherical mirror.

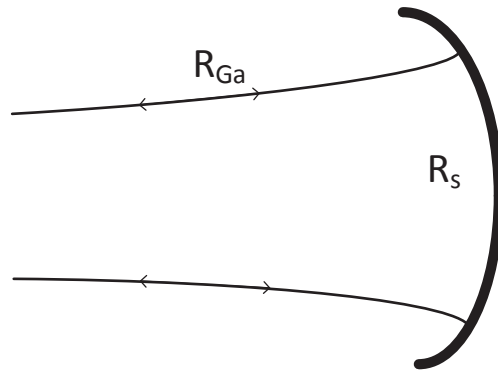


Figure 5.8: Schematic illustrating the role of spherical mirror

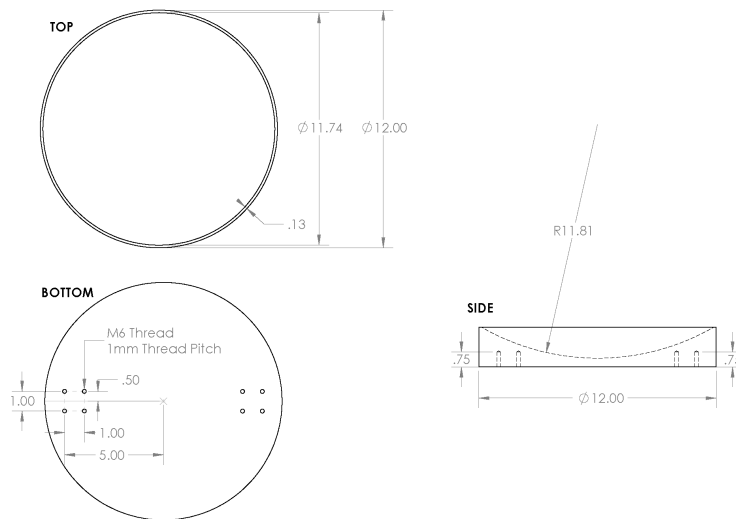


Figure 5.9: 2D model of the spherical mirror with dimensions

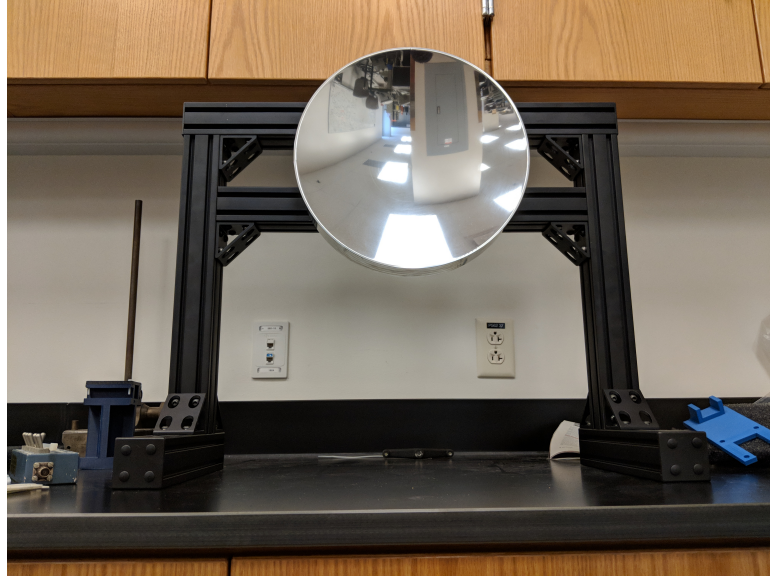


Figure 5.10: Photograph of the spherical mirror

## 5.5 Design of sample holder

The sample holders used in the experiments is custom made using 3D printing. Two different types of sample holders were designed to hold the MUT in the presence of static magnetic flux density ( $B$ ). The first sample holder was designed with toroidal magnets and the second one was designed with electromagnets.

### 5.5.1 Sample holder with toroidal magnets

The holder has two slots for placing rare earth toroidal magnets so as to create a  $B$  of 30 mT at the center. The holder also has a slot of about 28 mm in the center, for placing the MUT. A spacer was also made using 3D-printing to use with the sample holder to change  $B$  to 18 mT. Fig. 5.11 shows the sample holder used in the experiments for holding FMNWs sample. In order to use magnetoelastic material

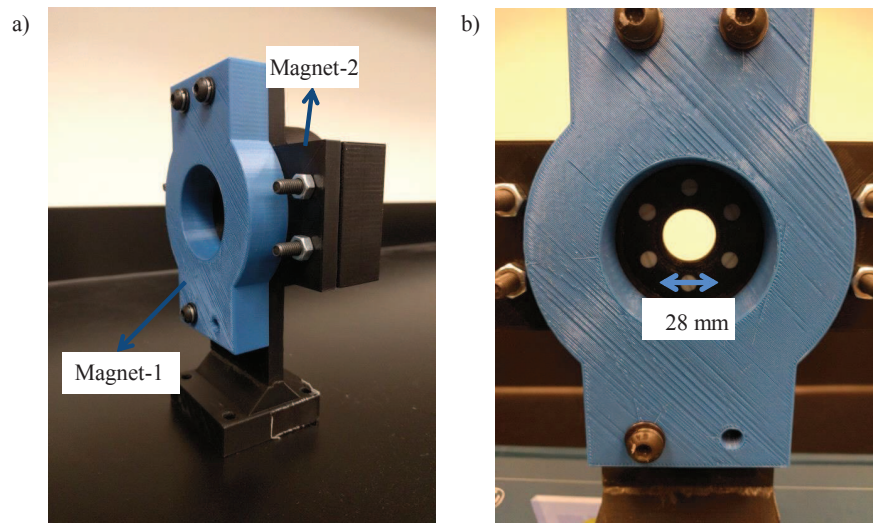


Figure 5.11: Photograph of custom made sample holder

sample a custom designed holder was used. The piezoelectric crystal was enveloped along its edges by a urethane rubber gasket which was fabricated by pouring Reoflex 50 (by Smooth-On, Inc.) in to a 3D printed mold. A ridge along the gasket interfaced with a 3-D printed fixture. Fig. 5.12 shows the crystal holder used for holding the magnetoelastic material.

#### 5.5.2 Sample holder with electromagnets

Fig. 5.13 shows the sample holder with electromagnets used for holding FMNWs sample . The current through the coils was varied to create different static values of  $B$ . Fig. 5.14 shows the 3D printed sample holder that is used to hold magnetoelastic material.

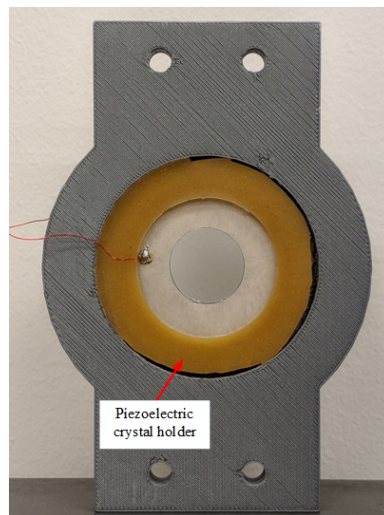


Figure 5.12: Crystal holder used for holding magnetoelastic material sample

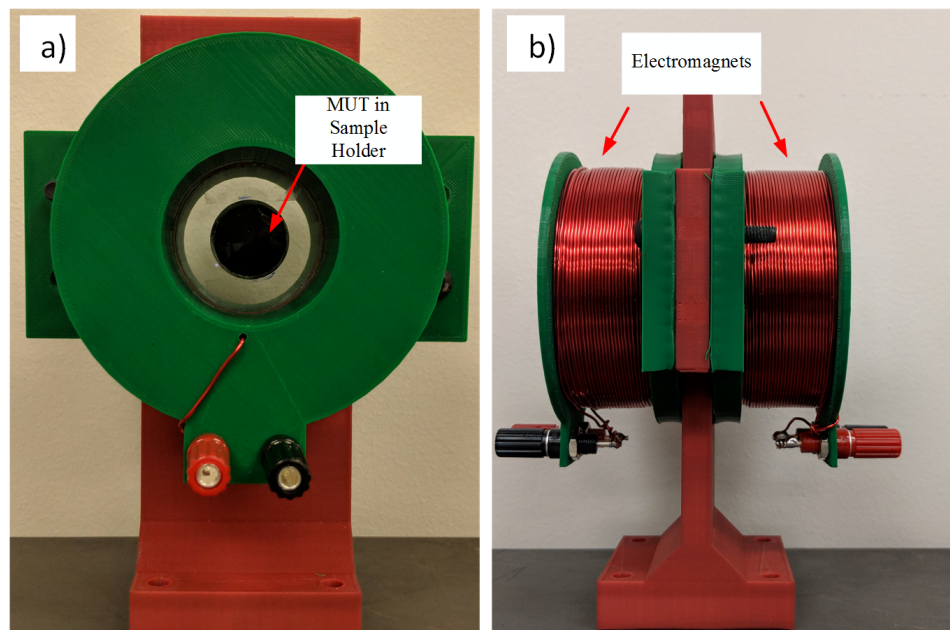


Figure 5.13: Photograph of custom made sample holder used for FMNWs sample

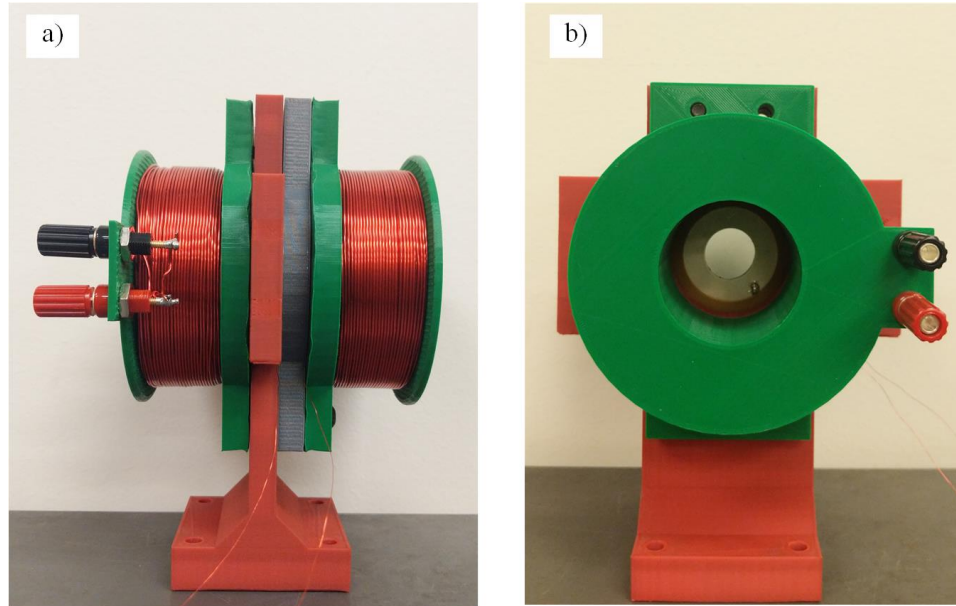


Figure 5.14: Photograph of custom made sample holder used for magnetoelastic material sample

Fig. 5.15 shows the values of  $B$  obtained from the designed electromagnets sample holder. A Gaussmeter was used to measure the  $B$  at the location of the MUT for each value of applied current on the terminals of the electromagnet. It can be observed from the figure that the sample holder can maintain  $B$  of up to 5.5 mT at the location where MUT will be placed.

## 5.6 Design of dielectric beam splitter

A dielectric beam splitter was used in our experiments to split the beam equally when placed at a  $45^\circ$  angle at a frequency of 61.25 GHz. A fused silica optical window as

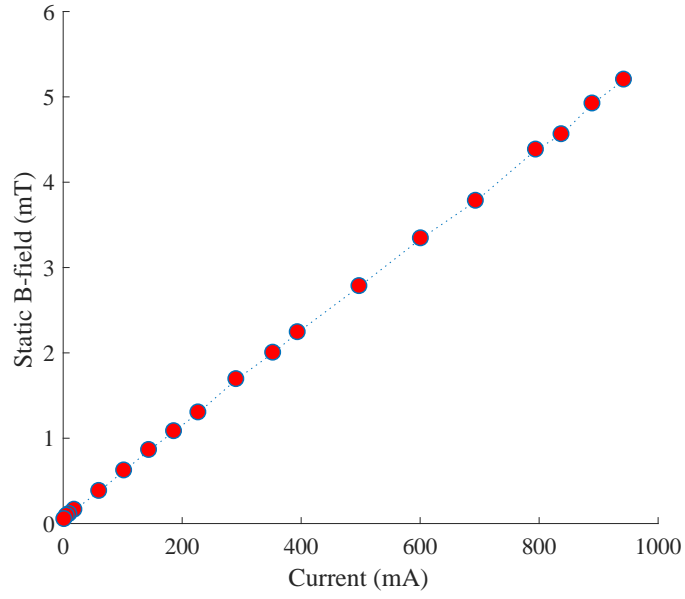


Figure 5.15: Static magnetic field from the electromagnet

shown in Fig 5.16 is used as a beam splitter. The beam splitter was designed using the equations from equations 5.13 to equations 5.16 [45].

$$\phi_{bs} = \frac{4\pi t_{bs}(n^2 - \sin^2 \theta_{bs})}{\lambda} \quad (5.13)$$

$$R_{bs} = \left[ \frac{\cos \theta_{bs} - (n^2 - \sin^2 \theta_{bs})^{0.5}}{\cos \theta_{bs} + (n^2 - \sin^2 \theta_{bs})^{0.5}} \right]^2 \quad (5.14)$$

$$R_f = \frac{4R_{bs} \sin^2 \phi_{bs}}{(1 - R_{bs})^2 + 4R_{bs} \sin^2 \phi_{bs}} \quad (5.15)$$

$$T_f = 1 - R_f \quad (5.16)$$

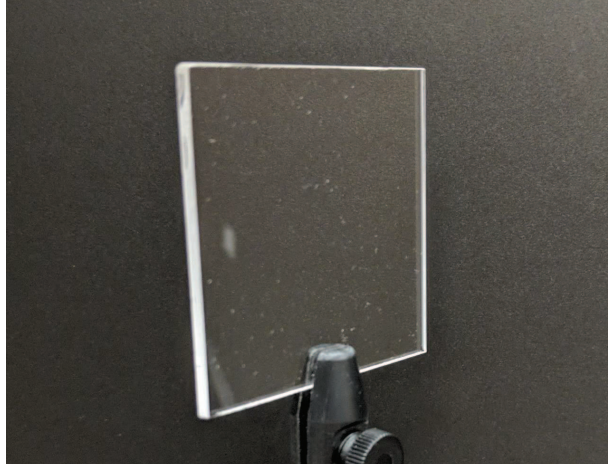


Figure 5.16: Photograph of beam splitter used in the experiments

Table 5.3: Parameters used to design beam splitter

Parameters	Values
Phase delay ( $\phi_{bs}$ )	8.7812
Thickness ( $t_{bs}$ )	1.9812 mm
Reflectivity function ( $R_f$ )	49.63
Transmission function ( $T_f$ )	50.37

## 5.7 Gaussian beam measurements

One of the most important aspects of designing the quasioptical components is to check if the designed components actually operate in the manner described by the

Gaussian beam parameters. This is a key factor in identifying the overall efficiency of the quasioptical system and to be able to predict the accurate performance of the quasioptical components. Hence there is a need to pattern the Gaussian beam at different locations in a quasioptical system. There are many techniques to pattern the Gaussian beam at millimeter and submillimeter wavelengths [39]. A few of the techniques are briefly described here.

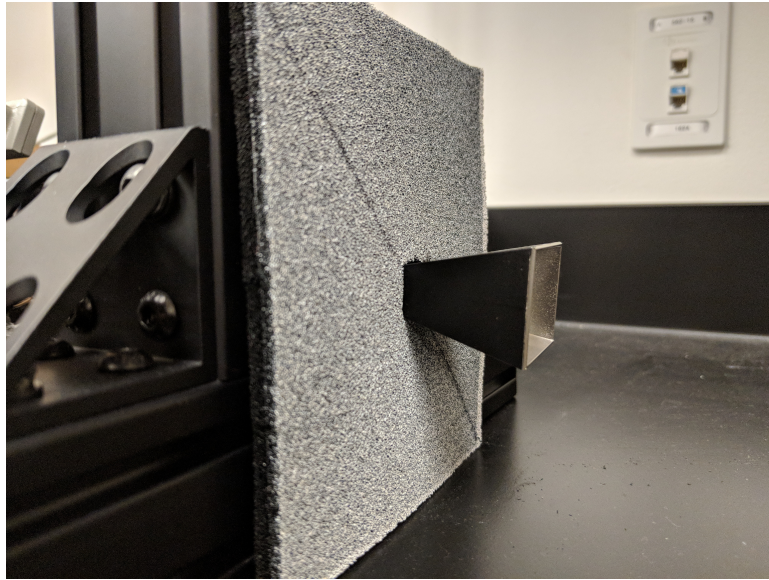


Figure 5.17: Gaussian beam measurement technique using horn antenna as a receiver antenna

First method is to use a high sensitive radiometric system (Radiometry is a set of techniques for measuring electromagnetic radiation) and use a small piece of absorbing material transversely in the beam. If the overall beam is terminated at liquid nitrogen temperature, the moving absorber can be ambient temperature. In order to obtain high spatial resolution, a small fraction of the beam can be filled

by the load at a different temperature. Thus the signal obtained is necessarily a small fraction of maximum that can be obtained for a given temperature difference and good sensitivity is critical. If at all the beam is symmetric, the moving sample can be made in to a strip filling the beam in one direction without sacrificing spatial resolution. A half plane can also be used and the actual beam pattern can be obtained deconvolution. This approach is also applicable for asymmetric beams.

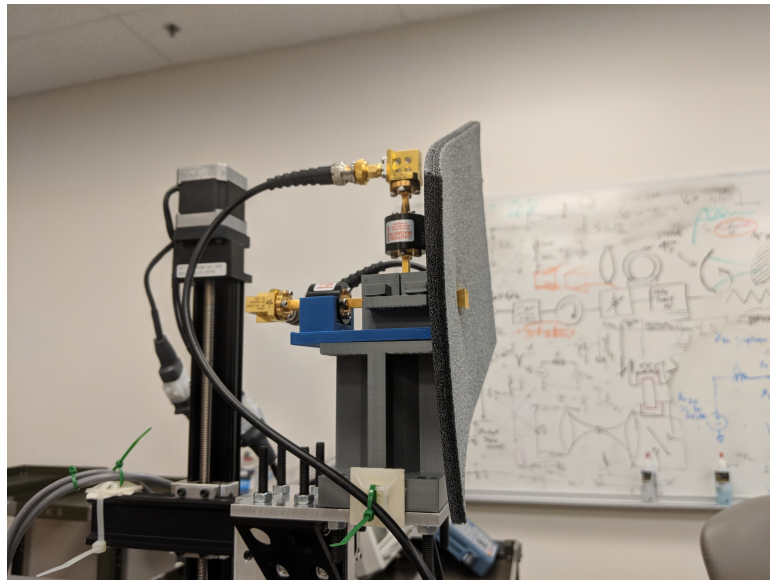


Figure 5.18: Gaussian beam measurement technique using dual polarized horn antenna as a receiver antenna

Another technique is to let the beam propagate and measure the angular distribution of radiation at a distance very much greater than Rayleigh range. Then, following the math for calculating the Gaussian beam parameters, the beam waist radius can be determined. However this technique is particularly effective only for small systems. At millimeter and submillimeter wavelengths beam sizes are usually

long enough that the beam pattern can be accurately determined using a detector. This technique assumes the availability of reasonably strong signal and better results can be obtained by interposing a sheet of absorbing material to minimize reflections from the measurement system. Fig. 5.17 and Fig. 5.18 shows the detection technique used in this work.

In this chapter the design and fabrication of quasioptical components, 3D printed components and Gaussian beam measurement techniques have been discussed. In the next chapter implementation of these quasioptical and 3D printed components in the experiments to demonstrate Faraday rotation in FMNWs and magnetoelastic materials will be discussed.

## CHAPTER VI

### EXPERIMENTS AND RESULTS

In the previous chapters, a mathematical expression for Faraday rotation was derived and quasioptical components used to manipulate Gaussian beam have been discussed. In order to measure the Faraday rotation angle in FMNWs and magnetoelastic materials four different sets of experiments were performed. This chapter discusses about all the four sets of experiments and results obtained. The results presented in this chapter are based on the journal papers "Millimeter-wave Faraday rotation from ferromagnetic nanowires" published in IEEE transactions on nanotechnology, "Voltage-Controlled, Nonreciprocal Millimeter-Wave Propagation From Magnetoelastic Membranes Infused With Aligned Nickel Microparticles" published in IEEE transactions on magnetics and "Ferromagnetic Nanowires for Nonreciprocal Millimeter-Wave Applications: Investigations of Artificial Ferrites for Realizing High-Frequency Communication Components" published in IEEE Nanotechnology magazine.

#### 6.1 Customized signal generator

The signal generator is custom made and constructed from the commercially-Off-The-Shelf (COTS) components. The generator can produce the signal within the

frequency range of 57 to 67 GHz by up-converting the output of a 10-MHz-to-20-GHz local oscillator (LO) with a  $4\times$  active multiplier, removing unwanted distortion products with an iris filter, and preventing reflections with a Faraday rotation isolator. A level set attenuator controls the signals power level. Fig. 6.1 shows the schematic of the signal generator. The LO is a HP83732B signal generator, the frequency multiplier is a solid state multiplier from Quinstar, that works from 14.25 GHz to 16.75 GHz. The bandpass filter is a IRIS filter from Quinstar that works in the frequency range of 57 GHz to 66 GHz.

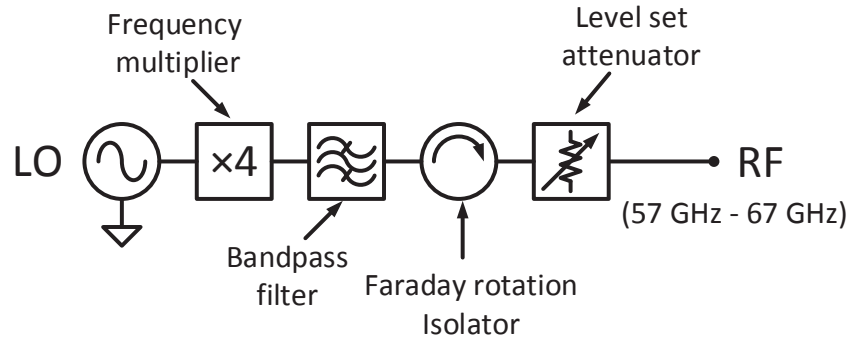


Figure 6.1: Schematic of signal generator

## 6.2 Experiments

Four sets of experiments have been performed. First two sets of experiments were performed with FMNWs as MUT and the second two sets of experiments were performed with magnetoelastic materials as MUT. Apparatus in all the four sets of experiments included a signal generator, ellipsoidal antenna, grid polarizer, sample holder with

magnets, detector antenna and a lock-in amplifier (LIA). EM wave (mm-wave) that propagates through the MUT was detected using a customized detector system. In all the experiments, the signal generator was operated at 61.25 GHz with an output RF power of 5 dBm (output power level can be controlled by the level set attenuator). This mm-wave signal was fed to a linearly-polarized ellipsoidal dish antenna, which was constructed from machined aluminum and fitted with a customized rectangular waveguide feed. An adjustable linear polarizer placed after the antenna ensured that the outgoing signal had a precise orientation of  $45^\circ$ .

### 6.2.1 First set of experiments

The first set of experiments were performed to confirm the existence of Faraday rotation in FMNWs. The experiments were based on a well-known three polarizer experiment which is briefly discussed here. When a parallel unpolarized light source (S), propagates a beam through a polarizing filter oriented at  $0^\circ$  ( $P_1$ ) as shown in Fig.6.2 a), the light passes through a polarizer the component of its amplitude parallel to the polarizer orientation is retained while the component perpendicular to the polarizer orientation is filtered out. By placing a detector (D) next to the polarizing filter, it can be noticed that a strong signal is observed in the detector. Similarly when another polarizing filter ( $P_3$ ) oriented at  $90^\circ$  is placed after the first polarizing filter, (as shown in Fig.6.2 b)) the detector receives no signal as the light after passing through the first polarizing filter, retains only the horizontal component. Since there is no light parallel to the filter  $P_3$ , the detector receives no signal. When a polarizer

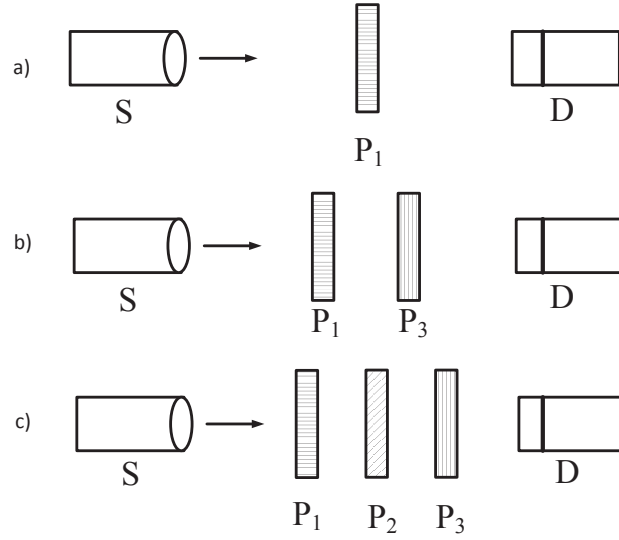


Figure 6.2: Three polarizer experiment

( $P_2$ ) filter oriented at  $45^\circ$  is placed in between these two polarizing filters, (as shown in Fig.6.2c)) a weak signal detected. Light after passing  $P_1$  generates only horizontal component. However after passing through  $P_2$ , lights polarization changed to  $45^\circ$  and hence there is a parallel component with respect to  $P_3$  and this signal is observed in the detector.

As mentioned before, the first set of experiments were based up on the three polarizer experiment. The source S is now an ellipsoidal dish antenna oriented at  $45^\circ \pm \delta\theta$  ( $\delta\theta$  is the error bar) that generates a mm-wave signal,  $P_1$  is a grid polarizer oriented at  $45^\circ$  (ensures that there is no error bar in the measurement), in place of  $P_2$  there is sample holder with static magnetic field biasing. A horn antenna (detector antenna) oriented at  $-45^\circ$  is used as a detector D. Ideally when there is no MUT, the

horn should receive no signal. When MUT is placed inside a sample holder, if there is any Faraday rotation due to the MUT, the detector receives a signal. Fig.6.3 shows the schematic of the apparatus used in the initial set of experiments.

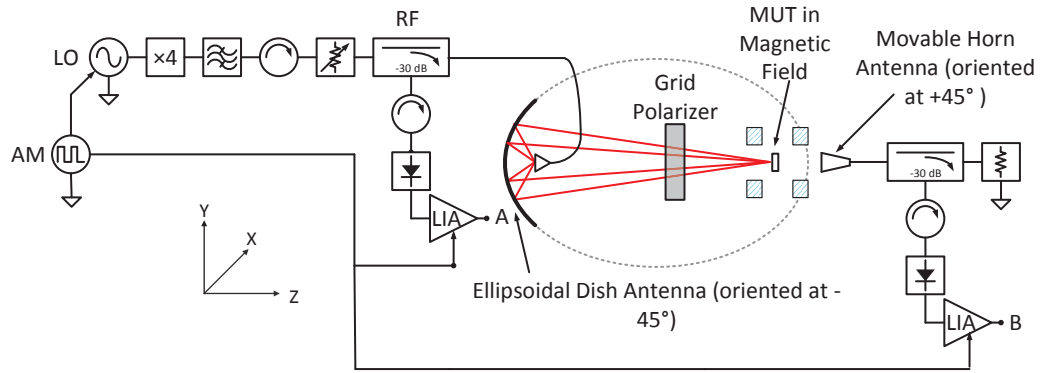


Figure 6.3: Schematic of the apparatus in the first set of experiments

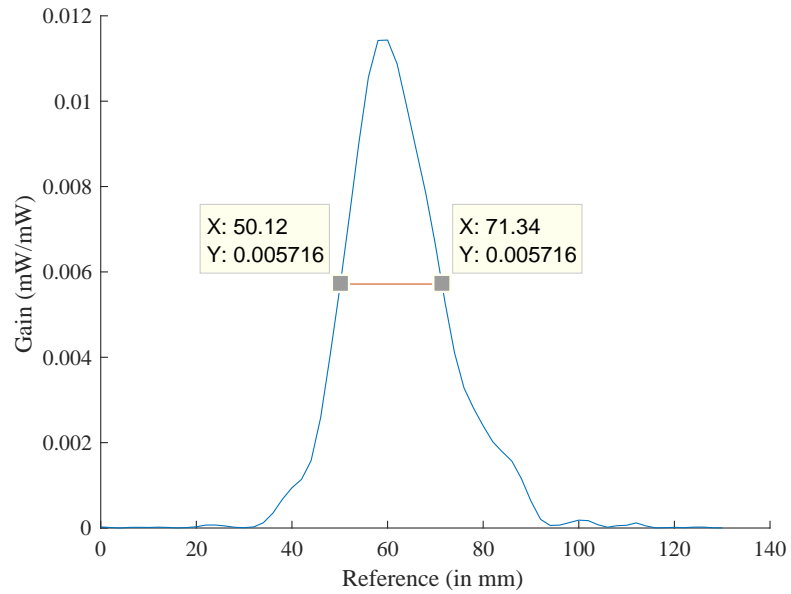


Figure 6.4: Detected Gaussian beam ( FWHM= 21mm)

In all of the first set of experiments a small fraction of the signal that was fed to the antenna was detected using customized detector system consisting of a 30 dB directional coupler, isolator and a broadband diode-based power detector. A lock-in amplifier, which was phase-locked with the square-wave amplitude modulation (AM) of the mmW signal at 13.7 KHz, provides the input voltage (labeled  $A$  in Fig 6.3) that is directly proportional to the power fed to the antenna. The antenna focused a Gaussian-like beam at approximately 540 mm from its center to a spot diameter of approximately 21 mm (spot diameter was determined based on the Full width at half maximum) (Fig 6.4) where the MUT was held in position with the customized sample holder with static magnetic field biasing. After the beam propagates through the MUT, the output transmitted signal from the MUT (labeled  $B$  in Fig 6.3) was received by a detector system (identical to that employed in detecting the power fed to the antenna). Five different experiments ( $F_1$  to  $F_5$ ) were performed in which the horn antenna was swept along an axis perpendicular ( $X$ -axis, as shown in Fig 6.3) to the optical axis ( $Z$ -axis) while measuring detected input and output power at each sweep position. Fig. 6.5 shows the photograph of experimental set-up.

The standard gain horn antenna, used as a receiver, was oriented at  $90^\circ$  with respect to the grid polarizer ( $-45^\circ$  with respect to optical axis) in order to ensure that no power would be received in the absence of a MUT. The detector antenna was swept along  $X$ -axis and the power gain ( $B/A$ ) was determined. A graphical user interface (GUI) was created in Matlab for automated experiments and to collect the gain data from the LIA. Experiment  $F_1$ , was performed with out MUT (labeled as No

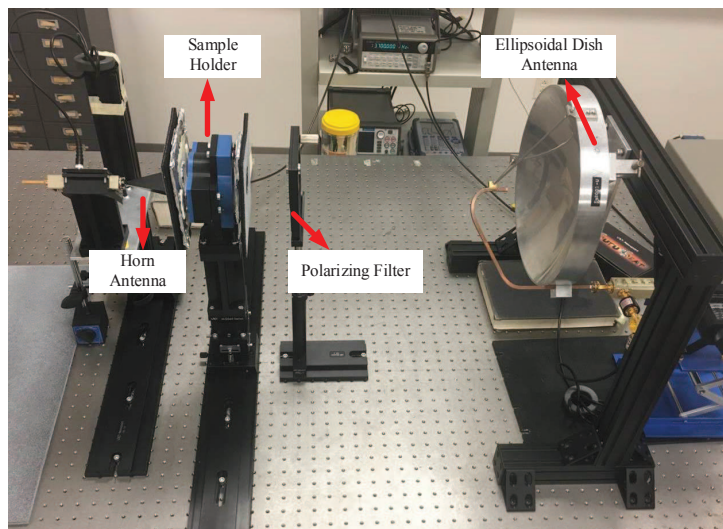


Figure 6.5: Photograph of the mmW Faraday rotation apparatus used in the first set of experiments

MUT in Fig 6.6). This experiment was performed in order to establish a baseline null measurement. It can be observed from Fig. 6.6 that gain data corresponding to null measurement is close to zero. In experiment  $F_2$  (labeled as Unfilled template in Fig 6.6), an unfilled template (having no nickel nanowires) was used as the MUT in order to gauge the contribution of reciprocal polarization rotation on overall measurement. The reciprocal polarization rotation is attributed to birefringence of the nanoporous polycarbonate and can be noticed in the Fig. 6.6.

Experiment  $F_3$  (filled template in Fig 6.6) was performed with FMNWs (nickel nanowires embedded in polycarbonate templates) as MUT. Gain corresponding to experiment  $F_3$  in Fig. 6.6 has a peak that indicates the presence of Faraday rotation in these FMNWs. Experiment  $F_4$  (labeled as -3dB measurement in Fig 6.6)

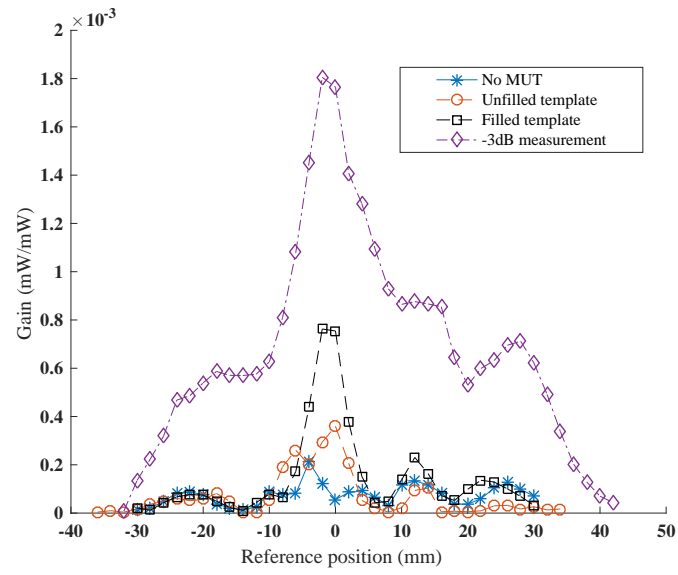


Figure 6.6: Plot comparing gain data in the first set of experiments

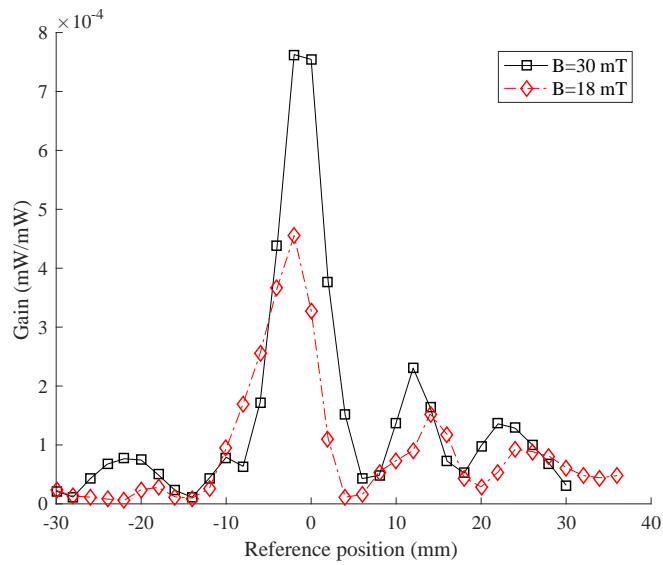


Figure 6.7: Plot comparing gain data for filled template at different DC magnetic bias

is a 3dB measurement, where the grid polarizer was adjusted to send out 50% of the power. This experiment was performed to estimate the amount of Faraday rotation in FMNWs. A final experiment  $F_5$  was performed with similar setup as  $F_3$  where the static magnetic field biasing was changed to 18 mT (with a spacer placed in the sample holder). There is shift in peak value of gain compared to  $F_3$  which confirms the presence of Faraday rotation. The results obtained in experiments ( $F_1$  to  $F_4$ ) are shown in Fig 6.6. The plot comparing the result obtained in  $F_3$  and  $F_5$  are shown in Fig 6.7. Experiments  $F_1$  to  $F_5$  have confirmed the presence of Faraday rotation in FMNWs.

Although these experiments confirm the presence of Faraday rotation in FMNWs, it doesn't give a definite value for Faraday rotation. In order to obtain the exact value of Faraday rotation, an expression to calculate Faraday rotation has to be determined (while birefringence needs to be eliminated). An expression for Faraday rotation angle was derived in chapter 4 and to filter out birefringence from Faraday rotation measurement, quasi optical components have been used (as mentioned in chapter 5). Hence, the experimental set-up in the next three sets of experiments consists of a customized signal generator, ellipsoidal dish antenna, polarizing filter, dielectric lens, beam splitter, customized sample holder with static magnetic field, spherical mirror, LIA and an oscilloscope.

After the first set of experiments, the feed on the antenna was readjusted and there was a shift in Gaussian beam waist location and the waist value. The antenna now generated a Gaussian-like beam approximately at 470 mm from its feed with a

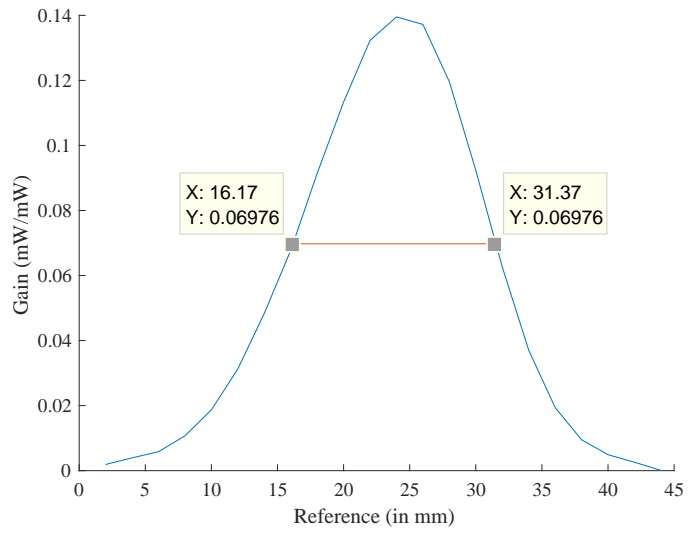


Figure 6.8: Detected Gaussian beam (FWHM= 15mm)

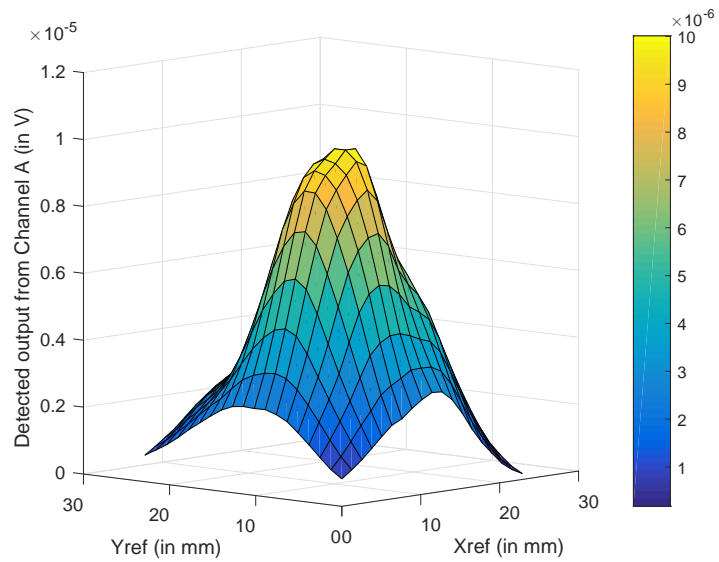


Figure 6.9: Power detected from channel A

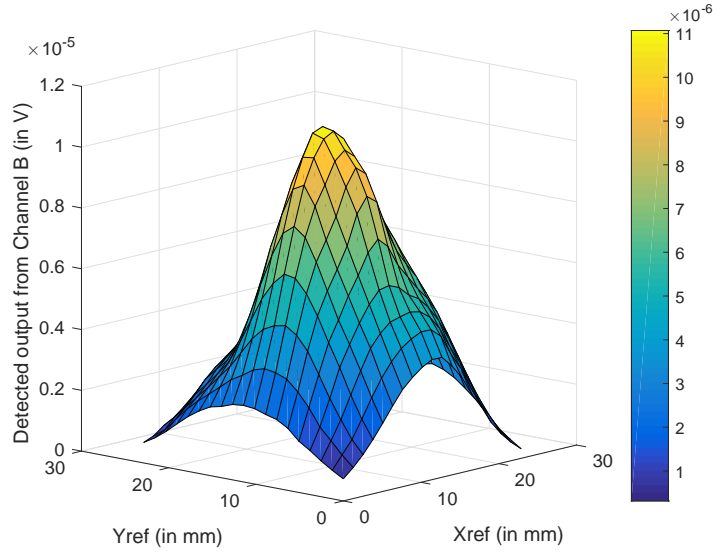


Figure 6.10: Power detected from channel B

spot size of 15 mm, as shown in Fig 6.8.

In order to apply the small angle Faraday rotation equation, intensity due to horizontal and vertical polarizations have to be separated and hence the detector horn antenna was now replaced with dual polarized antenna. This antenna was attached to a programmable XYZ stage from Velmex. A GUI was created in Matlab for automated experiments and 2D Gaussian plots were obtained by sweeping the antenna along XY plane. Fig. 6.9 shows the intensities due to horizontal and Fig.6.10 vertical polarizations from the dual polarized horn antenna.

### 6.2.2 Second set of experiments

In these experiments, MUT is FMNWs in nanoporous polycarbonate template. As mentioned before, the receiving horn antenna was now replaced with dual polarized

antenna (new receiving antenna). This antenna separates out the intensities due to horizontal polarization and vertical polarization through a detector system. The horizontal and vertical polarization intensity data from the dual polarized antenna was used to calculate the Faraday rotation angle in these materials. As mentioned before birefringence due to the MUT was eliminated by using quasi-optical components. The design of the quasi optical components used in this set of experiments was discussed in chapter 5.

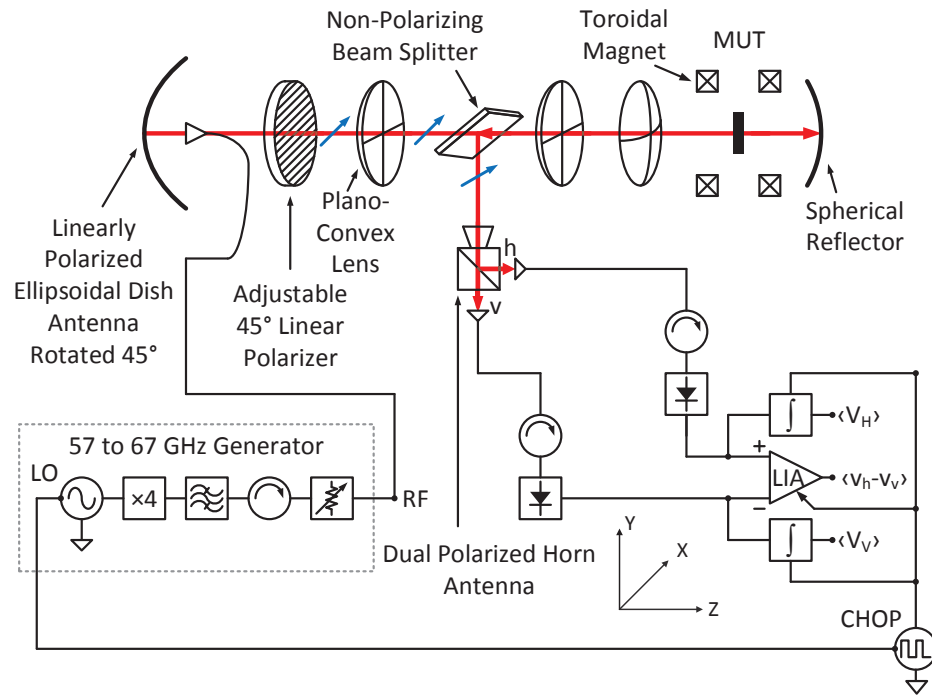


Figure 6.11: Schematic of the quasi-optical system in the second set of experiments

Fig.6.11 shows the schematic of the apparatus used in the second set of experiments. A plano-convex lens, fabricated from high density polyethylene (HDPE), was placed after the polarizer to adjust the beams depth of focus to a scale that is

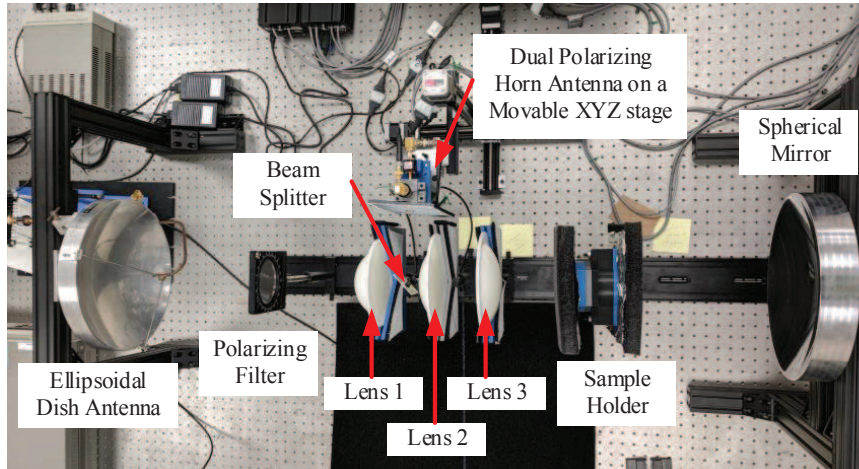


Figure 6.12: Photograph of the mmW Faraday rotation apparatus in the third set of experiments

appropriate for use with subsequent optical components. Following these networks, transmission through a non-polarizing beam splitter (fashioned from a fused silica plate) was placed. The beam splitter passes the beam through a second lensing system (consisting of two more plano-convex lenses) that will focus its spot size down to a value that is comparable to the 25 mm diameter of material under test (MUT). The MUT was biased with  $B$  by placing it in the sample holder. Once the beam has propagated through the MUT, it reflected off of a spherical mirror. The spherical mirror was placed at a location where the radius of curvature of gaussian beam is equal to the radius of curvature of the spherical mirror. The beam after hitting the spherical mirror will retrace the path backwards and was directed to a dual polarized horn antenna. Fig. 6.13 shows the location of lenses from the feed on the ellipsoidal dish antenna. Fig. 6.14 to Fig. 6.18 shows the experimental data collected at dif-

ferent locations during the Gaussian beam transformation. The data fits to a first order Gaussian implying there are no non-Gaussian components generated during the transformation.

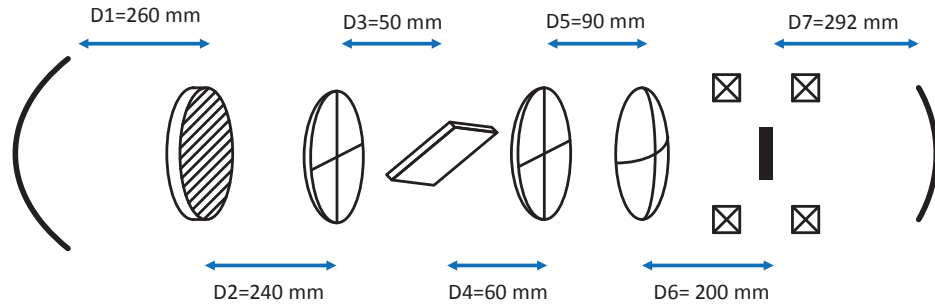


Figure 6.13: Location of different elements in the quasi-optical system

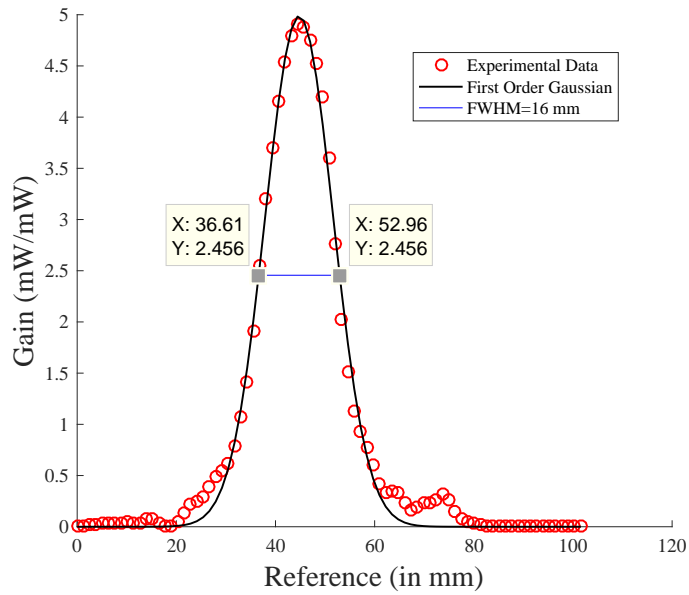


Figure 6.14: Gaussian beam after passing through lens 1

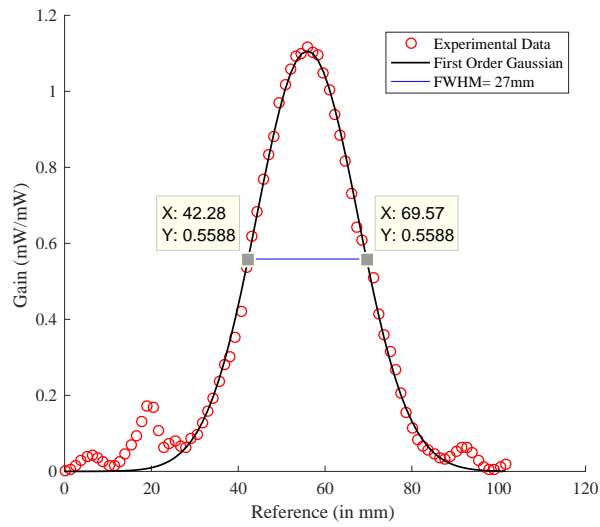


Figure 6.15: Detected Gaussian beam after passing through lens 2 and lens 3

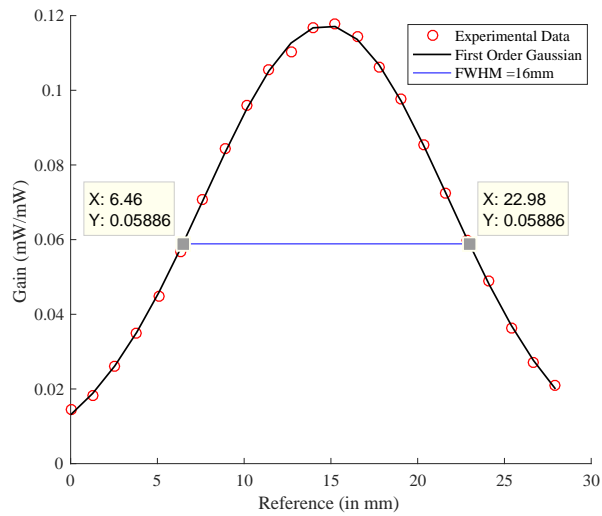


Figure 6.16: Detected Gaussian beam after passing through sample holder

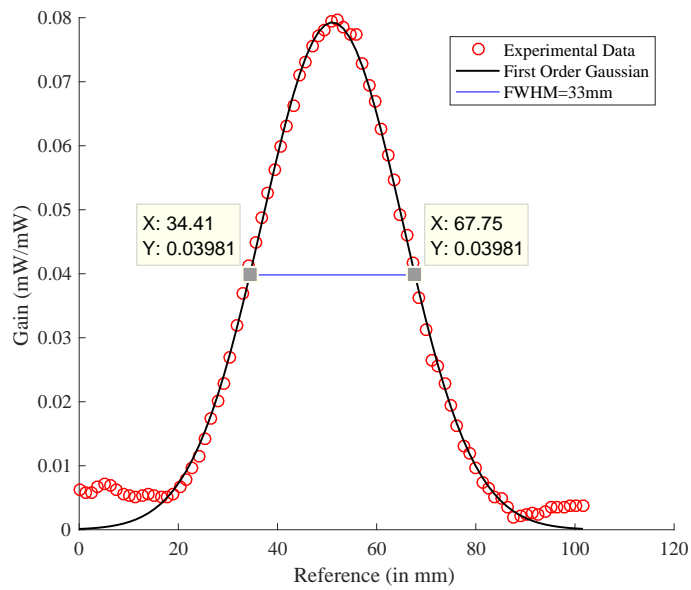


Figure 6.17: Detected Gaussian beam at the location of the spherical mirror

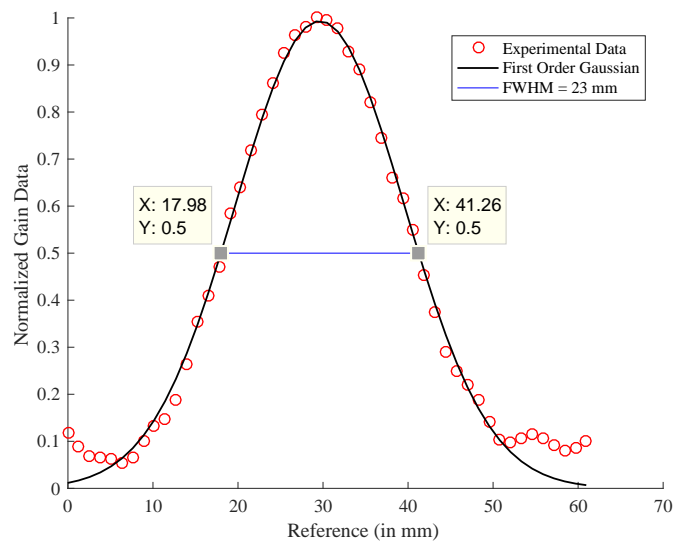


Figure 6.18: Detected Gaussian beam after reflecting back from the beam splitter

The output signals from this system correspond to the vertical (v) and horizontal (h) E-field components. These output signals were detected by a customized power detector system consisting of an isolator and a broadband diode-based detector. The isolators were used to prevent reflections. From the data obtained in the experiments, the Faraday rotation angle was calculated using equation 6.1 derived in chapter 4. Fig. 6.19 shows the plot of Faraday rotation angle calculated for  $B$  values of 30 mT and 18 mT.

$$\theta = \frac{\langle v_h - v_v \rangle}{2(\langle V_H \rangle + \langle V_V \rangle)}, \quad (6.1)$$

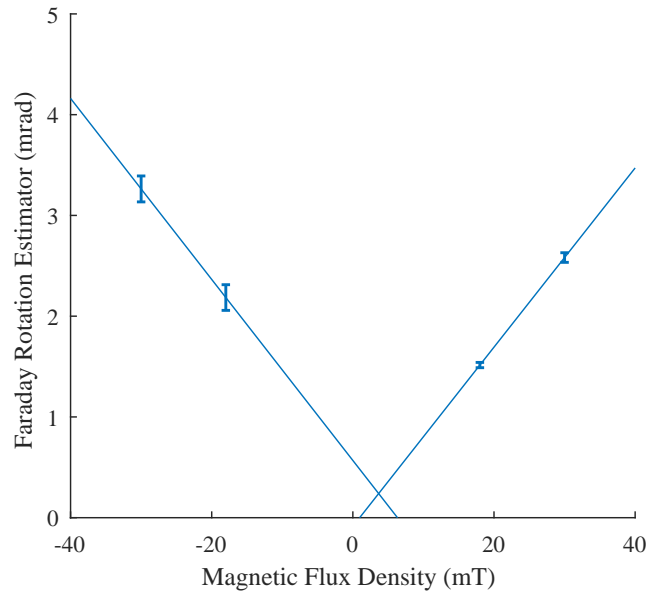


Figure 6.19: Faraday rotation measured at static magnetic fields of 30 mT and 18 mT

The constant  $n$  represents the number of times beam passes through the MUT. In this case the value of  $n$  is 2. The average value of the differential signal  $\langle v_h - v_v \rangle$  was obtained from the LIA, and the signals  $\langle V_H \rangle$  and  $\langle V_V \rangle$  were obtained from the oscilloscope. In the small-angle limit (such that  $2n\theta_{FR} \ll 1$ ), the estimator closely approximates the true angle of Faraday rotation  $\theta_{FR}$ . Experimental results indicate the presence of Faraday rotation due an anisotropic medium with direct proportionality to an externally applied static B-field. The error bar in the figure refers to Faraday rotation measured at different input power levels. The mean value of Verdet constant measured from the data was  $25.5 \times 10^3 \text{ radT}^{-1}\text{m}^{-1}$ . The sample holder with toroidal magnets is now replaced with a new sample holder with electromagnets and Faraday rotation was calculated from 5 mT to -5 mT with more data points. Fig. 6.20 shows the plot for Faraday rotation obtained in these experiments. A verdet constant of  $26.3 \times 10^3 \text{ radT}^{-1}\text{m}^{-1}$  was observed from the experiments. This value on the higher side compared to the reported values in the literature. A comparison of Veredet constants in different materials is shown in Table.6.1

Table 6.1: Table comparing verdet constants of different materials

Material	Frequency	Verdet Constant ( $\text{radT}^{-1}\text{m}^{-1}$ )
<i>MnCl<sub>2</sub>4H<sub>2</sub>O</i>	8.438 GHz to 8.981 GHz	$1.90 \times 10^3$
<i>MnSO<sub>4</sub>4H<sub>2</sub>O</i>	8.438 GHz to 8.981 GHz	$1.90 \times 10^3$
nickel zinc ferrite	9 GHz	$0.958 \times 10^3$
<i>SrFe<sub>12</sub>O<sub>19</sub></i>	200 GHz to 500 GHz	$1.53 \times 10^3$
nickel nanowires in PC templates	61.25 GHz	$25.7 \times 10^3$

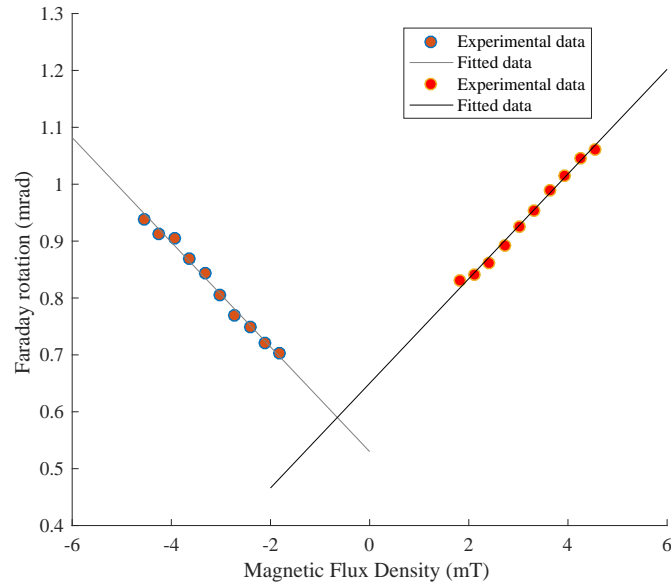


Figure 6.20: Faraday rotation measured at different magnetic fields

### 6.2.3 Third set of experiments

Fig.6.21 shows the schematic of the quasioptical system used in third set of experiments. Silicone rubber embedded with nickel microparticles attached to a piezocrystal was used as MUT in these experiments. As discussed in the previous chapter, these composite materials were fabricated using electromagnetic processing in conjunction with roll-to-roll (R2R) manufacturing [43], and they were fixed to piezoelectric crystals with annular shape. The piezoelectric annula were driven with AC signals so as to induce radial modes of expansion and contraction, to the density of the nickel particles as well as the magnetic permeability (inverse magnetostriction effect). Fig. 6.22a) shows the MUT used in the third set of experiments. Fig. 6.22b) shows the schematic of induced radial mode in the MUT while AC voltage is applied on to the

piezocrystal. In order to estimate the modulation of Ni particle density with the applied strain, experiments were performed. A sample of the magnetoelastic membrane was fixed across the jaws of a caliper using polyimide tape. The edges of the tape were used as reference markings during subsequent measurements of displacement. Using an optical microscope, images of the membrane were captured under unstrained and strained conditions.

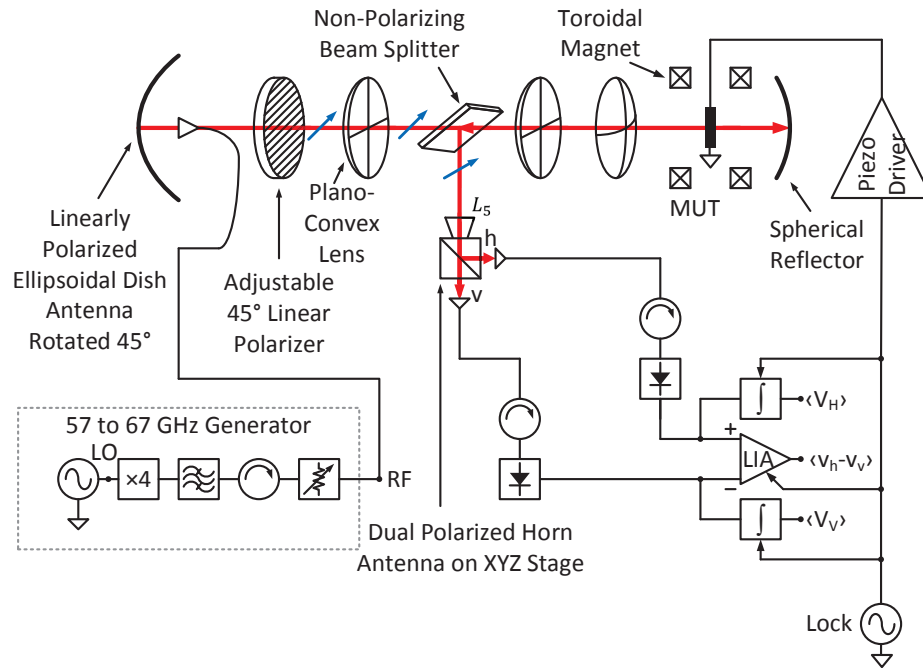


Figure 6.21: Schematic of the quasi-optical system used in the third set of experiments

Figs. 6.23 (a), (b) and (c) are microscope images of the initially unstrained material. Figs. 6.23 (a) and (b) resulted from focusing the microscope on the surface of the membrane with objective lens magnifications of  $2.5\times$  and  $20\times$ , respectively. The image of Fig. 6.23 (c) was captured, using an objective lens with  $20\times$  magnifi-

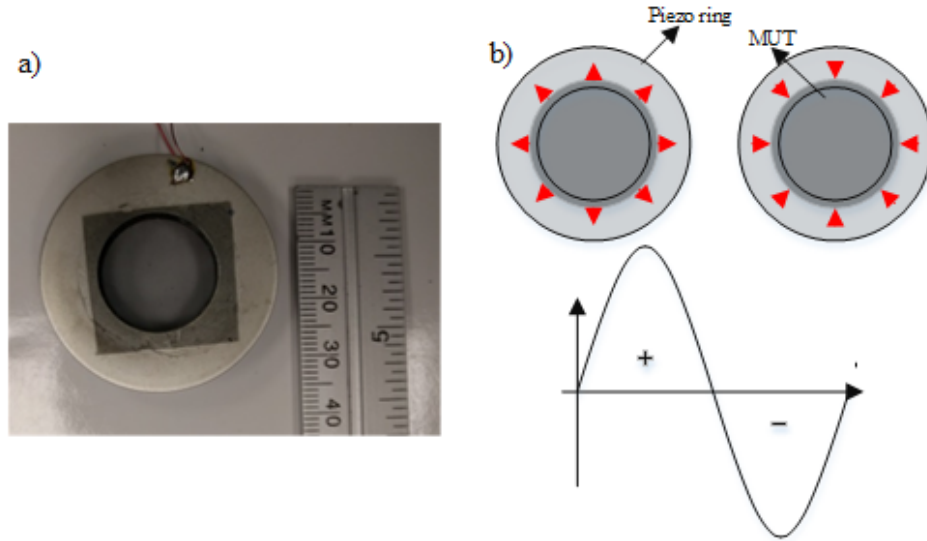


Figure 6.22: MUT attached to a piezoring

cation, with the microscope focused near the midpoint of the membrane's thickness. After capturing these images, the membrane was subjected to static strain by separating the jaws of the caliper by 10 mils (or  $254 \mu\text{m}$ ). The images of Figs. 6.23 (d), (e) and (f) were captured using the same microscope settings as those of Figs. 6.23 (a), (b) and (c), respectively. To ensure that the material would return to initial state when the strain was released, the separation of the caliper jaws was returned to its initial setting and the images of Figs. 6.23 (g), (h) and (i) were captured using the microscope settings of Figs. 6.23 (a), (b) and (c), respectively. By inspection of these three sets of images, it is evident that straining the membrane increased the effective areal cross-section of the Ni microparticle clusters perpendicular to the direction of mm-wave propagation. A Matlab script was used to quantify the ex-

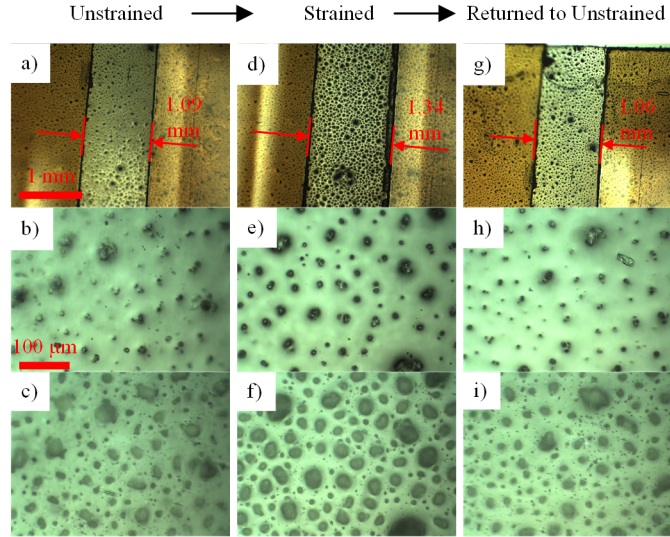


Figure 6.23: Strain experiments on magnetoelastic membranes. Images focused on surface of unstrained membrane with objective lens magnifications of (a)  $2.5\times$  and (b)  $20\times$ . (c) Image focused near midpoint of membrane thickness with objective lens magnification of  $20\times$ . (d), (e), (f) Images of membrane under strain collected with the same microscope settings (g), (h), (i) Images of relaxed membrane (returned to unstrained state) collected with the same microscope settings.

pansion of the clusters in response to the applied strain. The script calculated the ratio of total cluster area (defined by the dark regions) to the total area shown in each photograph. Using the images of Figs. 6.23 (c) and (f), it was determined that the Ni clusters expanded by approximately 67.4% when the material was strained by approximately 23.3% along a single axis. Fig. 6.23 (i) verified that the average Ni cluster size returned to its initial state (within a measurement error of  $\pm 3\%$ ) when the strain was released. It is known that the piezoelectric crystal used in this work (PZT 880) provides a maximum strain that is on the order of 1%. So, one can expect that during our experiments that involved driving the MUT with a sinusoidal voltage signal, the Ni clusters would have expanded by no more than 2.89%.

Experiments were then performed to determine the dependence of differential Faraday rotation  $\delta\theta$  on the frequency  $f_{Lock}$  and amplitude  $V_{Piezo}$  of the signal that drove the piezoelectric crystal. With the MUT in place, measurements of  $\langle v_h - v_v \rangle$ ,  $\langle V_H \rangle$ , and  $\langle V_V \rangle$  were collected as a function of the frequency  $f_{Lock}$  for different values of amplitude  $V_{Piezo}$ . To calculate values of  $\delta\theta$  at each frequency point, the measured quantities were applied to equation 6.1. Fig. 6.24 shows  $\delta\theta$  as a function of  $f_{Lock}$  for different values of amplitude  $V_{Piezo}$ . We were able to extract the radial resonant frequency of the crystal by fitting one of the curves of this dispersion data to a Lorentzian lineshape, which describes systems that can be modeled as simple harmonic oscillators. Our Lorentzian dispersion relationship is expressed as

$$\delta\theta = \frac{A}{(f_{Lock} - f_{res})^2 + (\Delta f/2)^2}. \quad (6.2)$$

In this expression,  $A$ ,  $f_{res}$  and  $\Delta f$  can be regarded as curve-fitting constants with  $f_{res}$  being the radial resonant frequency and  $\Delta f$  being the Lorentzian's full-width-at-half-maximum value. From the curve-fit, it was estimated that the resonance occurs at a frequency of approximately 160 kHz. Unfortunately, this value exceeds the operating limit of our LIA. So, subsequent experiments were performed at the maximum operating frequency of the LIA (150 kHz) in order to observe the largest possible values of  $\delta\theta$  that are measurable using LIA.

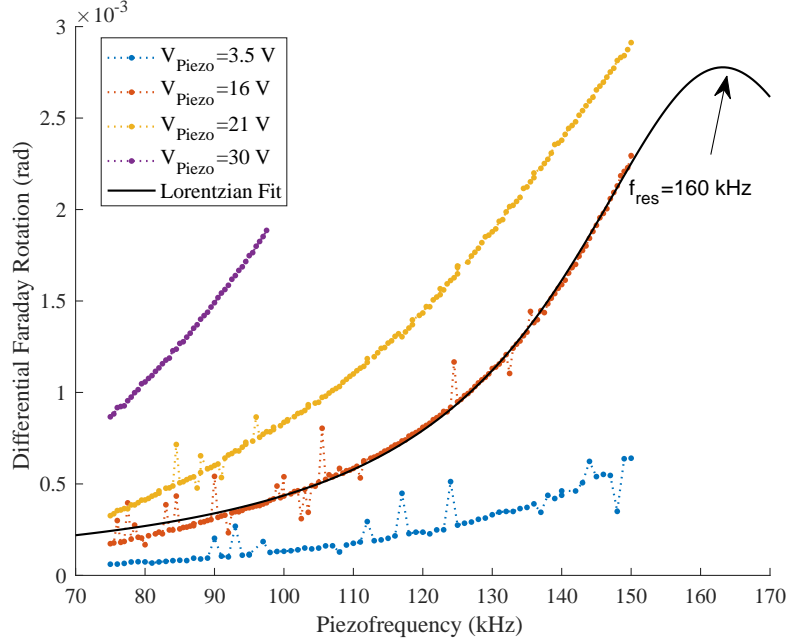


Figure 6.24: Differential Faraday rotation as a function of frequency for different values of amplitude of piezoelectric driving signal. Data corresponding to the case of  $V_{Piezo} = 16V$  has been fit to a Lorentzian lineshape. A radial resonant frequency of approximately 160 kHz has been extracted.

As shown in Fig. 6.25, measurements of  $\delta\theta$  were obtained as a function  $V_{Piezo}$  for two different values of static magnetic flux density ( $B = 18$  mT and  $B = 30$  mT). To demonstrate that the observed differential Faraday rotation was not simply an artifact due to our customized instrumentation, the same measurements were performed on a non-magnetic control sample, which consisted of a PDMS membrane having no infused Ni microparticles and a thickness that matched that of the magnetoelastic membrane. It can be observed from the figure that the non-magnetic control sample (the PDMS membrane) produced negligible differential Faraday rotation. It can also be observed that the differential Faraday rotation from the magnetoelastic

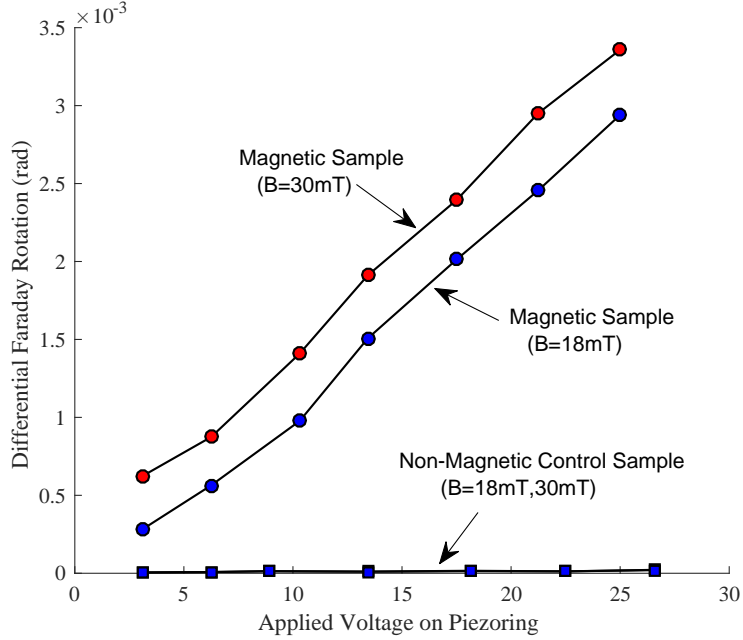


Figure 6.25: Differential Faraday rotation plotted as function of amplitude of piezoelectric driving signal (whose frequency was set to 150 kHz) for values of static magnetic field corresponding to  $B = 18$  mT and  $B = 30$  mT. Data has been obtained from the magnetoelastic membrane and a non-magnetic control sample.

membrane has direct proportionality to  $B$  and the amplitude  $V_{Piezo}$  of the signal used to drive the piezoelectric crystal. We have interpreted the results as indicating that  $V_{Piezo}$  produces a strain in the membrane that expands the apparent size of the areal cross-section of the Ni microparticle clusters and results in a change in the effective Verdet constant  $V$ . As Faraday rotation is often modeled in terms of the empirical relation  $\theta = BLV$  where  $L$  in our case would be the membrane thickness. Our measurements suggest that the observed differential Faraday rotation can be modeled as  $\delta\theta = BV_{Piezo}d(LV)/dV_{Piezo}$ . Radial strain on the membrane results in a change in membrane thickness  $\Delta L$  as determined by the Poisson ratio. At this point in

time, the Poisson ratio of the composite membrane is unknown. In cases where  $\Delta L$  is negligible, the relation for differential Faraday rotation can be approximated as  $\delta\theta \approx BLV_{Piezo}d(V)/dV_{Piezo}$ . Our experiments have shown that the Verdet constant is directly proportional to the amount of strain applied to the composite membrane. The Verdet constant is also related to magnetic permeability, which should be expressible as a function of both the average effective cross-sectional area of the Ni microparticle clusters as well as the density of microparticles comprising the clusters. However, further investigation is needed to determine the extent to which these individual microscopic properties contribute to constitutive parameters (such as magnetic permeability) and macroscopic effects (specifically, Faraday rotation).

#### 6.2.4 Fourth set of experiments

These set of experiments were performed to study the magnetic flux density detection capability of the designed quasioptical system using Faraday rotation. Experimental set-up and MUT in these experiments is similar to the third set of experiments. However, unlike the third set of experiments, sample holder used in these experiments has electromagnets.  $B$  in the sample holder was varied from  $60\mu\text{T}$  to  $5\text{ mT}$ . Amplitude of the applied voltage on the piezocrystal ( $V_{Piezo}$ ) was varied and differential Faraday rotation was calculated for different values of  $B$ . Fig.6.26 shows the differential Faraday rotation with varying  $V_{Piezo}$ .

It can be observed from the figure that differential Faraday rotation below  $0.38\text{ mT}$  did not have direct proportionality to  $B$ . Fig. 6.27 shows the logarithmic

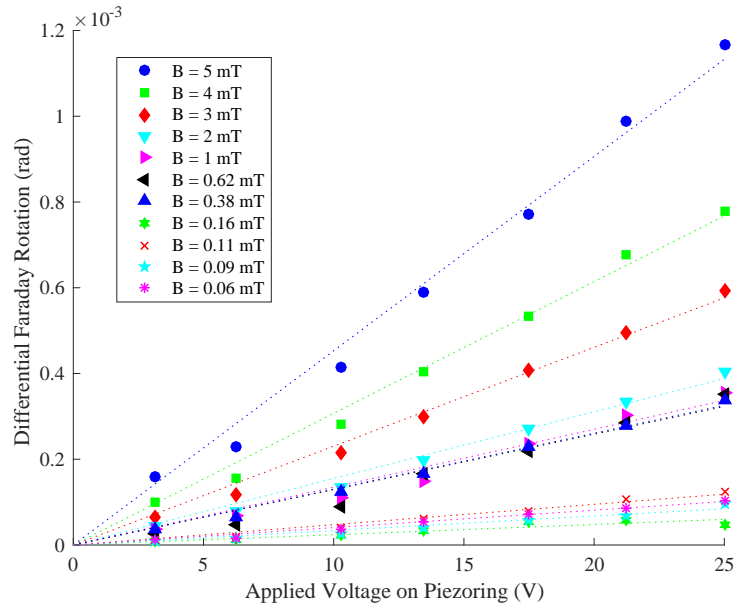


Figure 6.26: Differential Faraday rotation with applied voltage on the piezo crystal

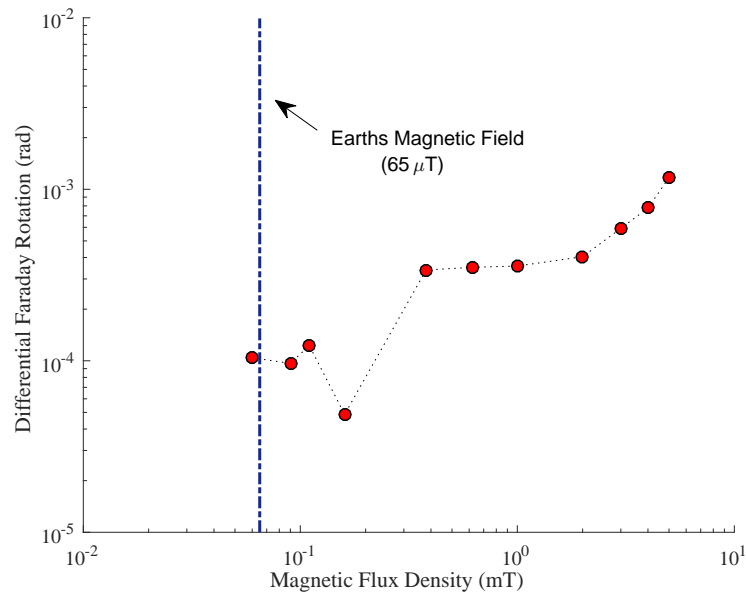


Figure 6.27: Differential Faraday rotation at maximum value of applied voltage on the piezo crystal

plot for differential Faraday rotation at maximum value of  $V_{Piezo}$ . It can be observed from this figure that the system was able to sense  $B$  of the order of 0.38 mT and the sensing deteriorated as the  $B$  value was brought more close to the earth's magnetic field.

In this chapter four different sets of experiments have been performed. First and second sets of experiments were performed using FMNWs as MUT. A high value of Verdet constant was observed in FMNWs. Third and fourth sets of experiments were performed on magnetoelastic materials. Faraday rotation can be tuned in these materials by changing the applied voltage on the piezoring.

## CHAPTER VII

### CONCLUSION AND FUTURE OUTLOOK

#### 7.1 Conclusion

FMNWs (artificial ferrites) have been fabricated using three electrode electrodeposition technique. Magnetoelastic material was grown on the EMP line. A unique quasioptical system was built for studying the Faraday rotation property in these artificial ferrites and magnetoelastic materials. Experiments were performed to confirm the presence of Faraday rotation in these artificial ferrites. Experiments were also performed to rule out birefringence and to calculate the exact Faraday rotation angle in FMNWs and magnetoelastic material. Experimental results from FMNWs indicate the presence of Faraday rotation with direct dependence on static magnetic flux density. Experimental results from magnetoelastic materials showed that Faraday rotation had a dependence of direct proportionality on the applied static magnetic flux density and on the voltage amplitude of the piezoelectric crystal.

#### 7.2 Future Outlook

The attraction of artificial ferrites composed of arrays of FMNWs embedded in nanoporous templates has been that (1) these third-generation metamaterials [1] offer

enhanced properties not normally observed in traditional bulk and thin-film ferrites, (2) these materials are synthesized by the reliable and inexpensive method of electroplating, (3) magnetizing the nanowires allows for self-biasing and eliminates the need for external magnets, and (4) their constitutive parameters (permeability and permittivity) can be tailored by engineering the size, density and material composition of the FMNWs. The major attraction with magnetoelastic materials is that tunable Faraday rotation can be obtained. However, the major drawback of this technology has been its lack of integration with on-chip active circuitry. This is a direction that needs to be explored. In the past research has been done to integrate FMNW based devices with on-chip active circuitry. In comparison to the competing, self-biased, passive solution provided by hexaferrites, three-port circulators based on FMNWs in alumina templates have demonstrated better non-reciprocal isolation but worse insertion loss. A variety of FMNW circulators, engineered to operate at different frequencies within the range of 10 to 30 GHz, provided isolation as high as 35 dB (and as low 25 dB) and insertion loss as low as 5 dB (and as high as 7 dB). Results from a 13.6 GHz circulator based on single-crystal hexaferrite slabs fixed to dielectric substrates have shown 21 dB isolation and 1.52 dB insertion loss [46]. In order to realize passive circulators that can be fully integrated with CMOS circuitry, others have investigated the use thick films based on hexagonal nano-ferrite powders [47] [48]. They realized 58 GHz circulators with unoptimized insertion loss of 8 dB and unreported isolation. However, for these particular comparisons, the main advantage offered by the FMNW technology is its low-cost material synthesis [49].

When integration is required, non-reciprocal components can be realized using competing technologies based on active circuitry. At microwave frequencies below 30 GHz, quasi-circulators have been realized using a 0.18  $\mu\text{m}$  complementary metal-oxide-semiconductor (CMOS) process. Demonstrations of 1.5 to 9.6 GHz operation has yielded  $>18$  dB isolation and an insertion loss of about 6 dB [50]. At 24 GHz,  $>30$  dB isolation with a 9 dB insertion loss has been reported [51], and at 30 GHz,  $>12$  dB isolation and 7.9 dB insertion loss has been reported [52]. At mm-wave frequencies (above 30 GHz), a 77 GHz quasi-circulator was fabricated using SiGe heterojunction bipolar transistor (HBT) technology; it yielded an isolation of 16 dB and an insertion loss of 1.5 dB [53]. In comparison to these competing technologies, based on active circuitry, the FMNW circulators offer superior isolation and comparable insertion loss. However, all the active circuit solutions require undesirable power consumption whereas the FMNW circulators are passive (requiring no power). In the case of the 77 GHz SiGe HBT circulators, which does suffer from the frequency-limiting parasitics of the CMOS solutions [54], the power consumption was 60 mW [53]. Additionally, limiting power consumption in active-circuit quasi-circulators leads to reduced dynamic range [47]. Hence, providing fully-integrated, non-reciprocal components that meet industry requirements remains a challenge. To address the issue of integration compatibility of FMNW-based components with active circuitry, previous researchers demonstrated that AAO templates could be used as substrates for printed circuit boards (PCBs) or possibly MMICs. They demonstrated the synthesis of FMNWs in selected regions of the templates and used this process to produce a self-biased

non-reciprocal component [55]. In terms of selectively patterning regions of FMNWs in AAO templates, others have used laser-assisted processing methods to realize isolators from non-reciprocal, substrate integrated waveguide (SIW) [56] [57].

## BIBLIOGRAPHY

- [1] Louis-Philippe Carignan, Arthur Yelon, David Ménard, and Christophe Caloz. Ferromagnetic nanowire metamaterials: Theory and applications. *IEEE Transactions on microwave theory and techniques*, 59(10):2568–2586, 2011.
- [2] CR Nave. “HyperPhysics: Classification of polarization”. Department of Physics and Astronomy, Georgia State University, 2016. Online: <http://hyperphysics.phy-astr.gsu.edu/hbase/phyopt/polclas.html>, accessed June 22, 2019.
- [3] G Goglio, S Pignard, A Radulescu, Luc Piraux, Isabelle Huynen, D Vanhonenacker, and André Vander Vorst. Microwave properties of metallic nanowires. *Applied Physics Letters*, 75(12):1769–1771, 1999.
- [4] Michaël Darques, Judith Spiegel, J De la Torre Medina, Isabelle Huynen, and Luc Piraux. Ferromagnetic nanowire-loaded membranes for microwave electronics. *Journal of magnetism and magnetic materials*, 321(14):2055–2065, 2009.
- [5] Michaël Darques, J De la Torre Medina, L Piraux, Laurent Cagnon, and Isabelle Huynen. Microwave circulator based on ferromagnetic nanowires in an alumina template. *Nanotechnology*, 21(14):145208, 2010.
- [6] Philips Semiconductor. Circulators and isolators, unique passive devices. *Application Note AN98035*, 1998.
- [7] David M Pozar. Microwave engineering 3e. *Transmission Lines and Waveguides*, pages 143–149, 2005.
- [8] Gerald F Dionne, Gary A Allen, Pamela R Haddad, Caroline A Ross, and Benjamin Lax. Circular polarization and nonreciprocal propagation in magnetic media. *Lincoln Laboratory Journal*, 15(2):323, 2005.
- [9] Heinrich Buff. Ueber das elektrische verhalten des aluminiums. *European Journal of Organic Chemistry*, 102(3):265–284, 1857.

- [10] F Keller, MS Hunter, and DL Robinson. Structural features of oxide coatings on aluminum. *Journal of the Electrochemical Society*, 100(9):411–419, 1953.
- [11] Robert Louis Fleischer, Paul Buford Price, and Robert M Walker. *Nuclear tracks in solids: principles and applications*. Univ of California Press, 1975.
- [12] Dietmar Fink, PS Alegaonkar, AV Petrov, M Wilhelm, P Szimkowiak, M Behar, D Sinha, WR Fahrner, K Hoppe, and LT Chadderton. High energy ion beam irradiation of polymers for electronic applications. *Nuclear Instruments and Methods in Physics Research Section B: Beam Interactions with Materials and Atoms*, 236(1-4):11–20, 2005.
- [13] Satoshi Kawai and Ryuzo Ueda. Magnetic properties of anodic oxide coatings on aluminum containing electrodeposited co and co-ni. *Journal of the Electrochemical Society*, 122(1):32–36, 1975.
- [14] Robert Pool. Physicists tackle theory, tubes, and temperature. *Science*, 247:1410–1412, 1990.
- [15] Charles R Martin. Template synthesis of polymeric and metal microtubules. *Advanced Materials*, 3(9):457–459, 1991.
- [16] D AlMawlawi, N Coombs, and Martin Moskovits. Magnetic properties of fe deposited into anodic aluminum oxide pores as a function of particle size. *Journal of applied physics*, 70(8):4421–4425, 1991.
- [17] TM Whitney, PC Searson, JS Jiang, and CL Chien. Fabrication and magnetic properties of arrays of metallic nanowires. *Science*, 261(5126):1316–1319, 1993.
- [18] Charles R Martin. Nanomaterials: a membrane-based synthetic approach. *Science*, 266(5193):1961–1966, 1994.
- [19] Anne K Bentley, Mohammed Farhoud, Arthur B Ellis, Anne-Marie L Nickel, George C Lisensky, and Wendy C Crone. Template synthesis and magnetic manipulation of nickel nanowires. *Journal of chemical education*, 82(5):765, 2005.
- [20] Shehreen Aslam, Manoj Khanna, Bijoy K Kuanr, and Z Celinski. One dimensional fexcol-x nanowires; ferromagnetic resonance and magnetization dynamics. *AIP Advances*, 7(5):056027, 2017.

- [21] Aimad Saib, Michaël Darques, Luc Piraux, Danielle Vanhoenacker-Janvier, and Isabelle Huynen. An unbiased integrated microstrip circulator based on magnetic nanowired substrate. *IEEE transactions on microwave theory and techniques*, 53(6):2043–2049, 2005.
- [22] J De La Torre Medina, Judith Spiegel, Michaël Darques, Luc Piraux, and Isabelle Huynen. Differential phase shift in nonreciprocal microstrip lines on magnetic nanowired substrates. *Applied Physics Letters*, 96(7):072508, 2010.
- [23] Yanqiu Li, Zheng Chen, Liangliang Li, and James Cai. 20 gigahertz noise suppressor based on ferromagnetic nanowire arrays. In *Advanced Packaging Materials (APM), 2011 International Symposium on*, pages 94–98. IEEE, 2011.
- [24] Bijoy K Kuanr, Ryan Marson, Sanjay R Mishra, Alka V Kuanr, RE Camley, and ZJ Celinski. Gigahertz frequency tunable noise suppressor using nickel nanorod arrays and permalloy films. *Journal of Applied Physics*, 105(7):07A520, 2009.
- [25] Baekil Nam, Yong-Ho Choa, Sung-Tag Oh, Sang Kwan Lee, and Ki Hyeon Kim. Broadband rf noise suppression by magnetic nanowire-filled composite films. *IEEE Transactions on Magnetics*, 45(6):2777–2780, 2009.
- [26] Aimad Saib and Isabelle Huynen. Periodic metamaterials combining ferromagnetic nanowires and dielectric structures for planar circuits applications. *Electromagnetics*, 26(3-4):261–277, 2006.
- [27] Aimad Saib, D Vanhoenacker-Janvier, I Huynen, A Encinas, L Piraux, E Ferain, and R Legras. Magnetic photonic band-gap material at microwave frequencies based on ferromagnetic nanowires. *Applied physics letters*, 83(12):2378–2380, 2003.
- [28] Ariana LC Serrano, Anne-Laure Franc, DP Assis, Florence Podevin, Gustavo P Rehder, Nicolas Corrao, and Philippe Ferrari. Modeling and characterization of slow-wave microstrip lines on metallic-nanowire-filled-membrane substrate. *IEEE Transactions on Microwave Theory and Techniques*, 62(12):3249–3254, 2014.
- [29] Júlio M Pinheiro, Gustavo P Rehder, Leonardo G Gomes, Rogerio CA Alvarenga, Marcus V Pelegrini, Florence Podevin, Philippe Ferrari, and Ariana LC Serrano. 110-ghz through-substrate-via transition based on copper nanowires in alumina membrane. *IEEE Transactions on Microwave Theory and Techniques*, 66(2):784–790, 2018.

- [30] Brian Toal, Mark McMillen, Antony Murphy, William Hendren, Ron Atkinson, and Robert Pollard. Tuneable magneto-optical metamaterials based on photonic resonances in nickel nanorod arrays. *Materials Research Express*, 1(1):015801, 2014.
- [31] AE Clark, BF DeSavage, and R Bozorth. Anomalous thermal expansion and magnetostriction of single-crystal dysprosium. *Physical Review*, 138(1A):A216, 1965.
- [32] JJ Rhyne and S Legvold. Magnetostriction of tb single crystals. *Physical Review*, 138(2A):A507, 1965.
- [33] NC Koon, CM Williams, and BN Das. Giant magnetostriction materials. *Journal of magnetism and magnetic materials*, 100(1-3):173–185, 1991.
- [34] Arthur E Clark and Marilyn Wun-Fogle. Modern magnetostrictive materials: classical and nonclassical alloys. In *Smart Structures and Materials 2002: Active Materials: Behavior and Mechanics*, volume 4699, pages 421–437. International Society for Optics and Photonics, 2002.
- [35] Arthur E Clark, James B Restorff, Marilyn Wun-Fogle, Thomas A Lograsso, and Deborah L Schlagel. Magnetostrictive properties of body-centered cubic fe-ga and fe-ga-al alloys. *IEEE Transactions on Magnetics*, 36(5):3238–3240, 2000.
- [36] John Patrick Domann. *On Magnetoelastodynamics*. PhD thesis, University of California, Los Angeles, 2017.
- [37] CA Grimes, KG Ong, K Loiselle, PG Stoyanov, D Kouzoudis, Y Liu, C Tong, and F Tefiku. Magnetoelastic sensors for remote query environmental monitoring. *Smart Materials and Structures*, 8(5):639, 1999.
- [38] Craig Grimes, Casey Mungle, Kefeng Zeng, Mahaveer Jain, William Dreschel, Maggie Paulose, and Keat Ong. Wireless magnetoelastic resonance sensors: A critical review. *Sensors*, 2(7):294–313, 2002.
- [39] Paul F Goldsmith, Institute of Electrical, Electronics Engineers, Microwave Theory, and Techniques Society. *Quasioptical systems: Gaussian beam quasioptical propagation and applications*. IEEE press New York, 1998.
- [40] Huamei Mary Shang and Guozhong Cao. Template-based synthesis of nanorod or nanowire arrays. In *Springer Handbook of Nanotechnology*, pages 169–186. Springer, 2010.

- [41] Sai Prudhvi Kumar Gummadi. Microwave applications of the ferromagnetic nanowires. Master's thesis, The University of Akron, 2016.
- [42] Vale. Datasheet: "Nickel powder - T123 CDN", February 2011. Online: <http://www.vale.com/EN/business/mining/nickel/NickelProducts/T123%20CDN.pdf>, accessed June 22, 2019.
- [43] Yuwei Chen, Yuanhao Guo, Saurabh Batra, Enmin Wang, Yanping Wang, Xueqing Liu, Yimin Wang, and Miko Cakmak. Transparent and through thickness conductive polystyrene films using external magnetic fields for z alignment of nickel nanoparticles. *Nanoscale*, 7(35):14636–14642, 2015.
- [44] Edward Collett. Polarized light. fundamentals and applications. *Optical Engineering*, New York: Dekker, 1992.
- [45] Kenneth J Button. *Infrared and Millimeter Waves V7: Coherent Sources and Applications, Part-II*. Elsevier, 1983.
- [46] Jianwei Wang, Aria Yang, Yajie Chen, Zhaohui Chen, Anton Geiler, Scott M Gillette, Vincent G Harris, and Carmine Vittoria. Self biased y-junction circulator at  $k_u$  band. *IEEE Microwave and Wireless Components Letters*, 21(6):292–294, 2011.
- [47] Liu Chao, Hassan Oukacha, Enjin Fu, Valencia Joyner Koomson, and Mohammed N Afsar. Millimeter wave complementary metal-oxide-semiconductor on-chip hexagonal nano-ferrite circulator. *Journal of Applied Physics*, 117(17), 2015.
- [48] Liu Chao, Enjin Fu, Valencia J Koomson, and Mohammed N Afsar. Millimeter wave complementary metal-oxide-semiconductor on-chip hexagonal ferrite circulator. *Journal of Applied Physics*, 115(17):17E511, 2014.
- [49] Yajie Chen, Anton L Geiler, Taiyang Chen, Tomokazu Sakai, C Vittoria, and VG Harris. Low-loss barium ferrite quasi-single-crystals for microwave application. *Journal of applied physics*, 101(9):09M501, 2007.
- [50] Shih-Chieh Shin, Jih-Yu Huang, Kun-You Lin, and Huei Wang. A 1.5–9.6 ghz monolithic active quasi-circulator in 0.18  $\mu\text{m}$  cmos technology. *IEEE Microwave and Wireless Components Letters*, 18(12):797–799, 2008.
- [51] Ding-Jie Huang, Jing-Lin Kuo, and Huei Wang. A 24-ghz low power and high isolation active quasi-circulator. In *Microwave Symposium Digest (MTT), 2012 IEEE MTT-S International*, pages 1–3. IEEE, 2012.

- [52] Chia-Hao Chang, Yu-Tsung Lo, and Jean-Fu Kiang. A 30 ghz active quasi-circulator with current-reuse technique in 0.18  $\mu\text{m}$  cmos technology. *IEEE Microwave and Wireless Components Letters*, 20(12):693–695, 2010.
- [53] Matthias Porranzl, Christoph Wagner, Herbert Jaeger, and Andreas Stelzer. An active quasi-circulator for 77 ghz automotive fmcw radar systems in sige technology. *IEEE Microwave and Wireless Components Letters*, 25(5):313–315, 2015.
- [54] Michael Schröter, Tommy Rosenbaum, Pascal Chevalier, Bernd Heinemann, Sorin P Voinigescu, Ed Preisler, Josef Böck, and Anindya Mukherjee. Sige hbt technology: Future trends and tcad-based roadmap. *Proceedings of the IEEE*, 105(6):1068–1086, 2017.
- [55] Louis-Philippe Carignan, Toshiro Kodera, Arthur Yelon, Christophe Caloz, and David Menard. Integrated and self-biased planar magnetic microwave circuits based on ferromagnetic nanowire substrates. In *Microwave Conference, 2009. EuMC 2009. European*, pages 743–746. IEEE, 2009.
- [56] Vivien Van Kerckhoven, Luc Piraux, and Isabelle Huynen. A laser-assisted process to produce patterned growth of vertically aligned nanowire arrays for monolithic microwave integrated devices. *Nanotechnology*, 27(23):235301, 2016.
- [57] Ke Wu, Dominic Deslandes, and Yves Cassivi. The substrate integrated circuits-a new concept for high-frequency electronics and optoelectronics. In *Telecommunications in Modern Satellite, Cable and Broadcasting Service, 2003. TELSIKS 2003. 6th International Conference on*, volume 1, pages P–III. IEEE, 2003.

## APPENDICES

## APPENDIX A

### SMALL ANGLE FARADAY ROTATION DERIVATION

(\* Stokes Vector for Unpolarized Wave \*)

$$S_u = \begin{pmatrix} +1 \\ 0 \\ 0 \\ 0 \end{pmatrix};$$

(\*StokesVectorforLinearlyPolarizedWave – Horizontal\*)

$$S_h = \begin{pmatrix} +1 \\ +1 \\ 0 \\ 0 \end{pmatrix};$$

(\*StokesVectorforLinearlyPolarizedWave – Vertical\*)

$$S_v = \begin{pmatrix} +1 \\ -1 \\ 0 \\ 0 \end{pmatrix};$$

(\*StokesVectorforLinearlyPolarizedWave – +45°\*)

$$\text{Sp45} = \begin{pmatrix} +1 \\ 0 \\ +1 \\ 0 \end{pmatrix};$$

(\*StokesVectorforRight – HandCircularlyPolarizedWave\*)

$$\text{Srcp} = \begin{pmatrix} +1 \\ 0 \\ 0 \\ +1 \end{pmatrix};$$

(\*StokesVectorforLeft – HandCircularlyPolarizedWave\*)

$$\text{Slcp} = \begin{pmatrix} +1 \\ 0 \\ 0 \\ -1 \end{pmatrix};$$

(\* Mueller Matrix for Faraday Rotating Sample \*)

$$\text{Ms}[\theta] = \begin{pmatrix} +1 & 0 & 0 & 0 \\ 0 & +\text{Cos}[2 * \theta] & -\text{Sin}[2 * \theta] & 0 \\ 0 & +\text{Sin}[2 * \theta] & +\text{Cos}[2 * \theta] & 0 \\ 0 & 0 & 0 & +1 \end{pmatrix};$$

$$Mh = \frac{1}{2} \begin{pmatrix} +1 & +1 & 0 & 0 \\ +1 & +1 & 0 & 0 \\ 0 & 0 & 0 & 0 \\ 0 & 0 & 0 & 0 \end{pmatrix}; (* \text{ Horizontal Component } *)$$

$$Mv = \frac{1}{2} \begin{pmatrix} +1 & -1 & 0 & 0 \\ -1 & +1 & 0 & 0 \\ 0 & 0 & 0 & 0 \\ 0 & 0 & 0 & 0 \end{pmatrix}; (* \text{ Vertical Component } *)$$

$$\theta[\theta_-, fm_-, t_-] := \theta_0 * \text{UnitStep}[\text{Sin}[2 * \pi * fm * t]]$$

$$Mmom[n_-, \theta_0_-, fm_-, t_-] = \begin{pmatrix} 1 & 0 & 0 & 0 \\ 0 & \text{Cos}[2 * \theta[\theta_0, fm, t]] & -\text{Sin}[2 * \theta[\theta_0, fm, t]] & 0 \\ 0 & \text{Sin}[2 * \theta[\theta_0, fm, t]] & \text{Cos}[2 * \theta[\theta_0, fm, t]] & 0 \\ 0 & 0 & 0 & 1 \end{pmatrix};$$

(\*Mueller Matrix for vertical component\*)

$$Iv[n_-, \theta_0_-, fm_-, t_-] = \text{MatrixForm}[\text{FullSimplify}[Mv.Mmom[n, \theta_0, fm, t].Sp45, \{n > 0, f > 0, t > 0, \theta_0 \in \text{Reals}\}]][[1, 1]][[1]]$$

(\*Mueller Matrix for Horizontal component\*)

$$Ih[n_-, \theta_0_-, fm_-, t_-] = \text{MatrixForm}[\text{FullSimplify}[Mh.Mmom[n, \theta_0, fm, t].Sp45, \{n > 0, f > 0, t > 0, \theta_0 \in \text{Reals}\}]][[1, 1]][[1]] \\ \frac{1}{2}(1 + \text{Sin}[2\theta_0 \text{UnitStep}[\text{Sin}[2fm\pi t]]])$$

$$\frac{1}{2} - \frac{1}{2}\text{Sin}[2\theta 0\text{UnitStep}[\text{Sin}[2\text{fm}\pi t]]]$$

**(\* Gated Integrator Signals \*)**

$$V[n_-, \theta_-, \text{fm}_-, t_-] = \text{FullSimplify}[\text{Iv}[n, \theta 0, \text{fm}, t], \{n > 0, f > 0, t > 0, \theta 0 \in \text{Reals}\}]$$

$$\frac{1}{2}(1 + \text{Sin}[2\theta 0\text{UnitStep}[\text{Sin}[2\text{fm}\pi t]]])$$

**(\*Large – SignalfromVerticalPolarizationDetector\*)**

$$\langle V_V \rangle = \text{FullSimplify} \left[ \frac{1}{1/\text{fm}} * \text{Abs} \left[ \int_0^{(1/\text{fm})} V[n, \theta 0, \text{fm}, t] dt \right], \{n > 0, t > 0, \text{fm} > 0\} \right]$$

$$\frac{1}{2}\text{Abs}[1 + \text{Cos}[\theta 0]\text{Sin}[\theta 0]]$$

$$H[n_-, \theta_-, \text{fm}_-, t_-] = \text{FullSimplify}[\text{Ih}[n, \theta 0, \text{fm}, t], \{n > 0, f > 0, t > 0, \theta 0 \in \text{Reals}\}]$$

$$\frac{1}{2} - \frac{1}{2}\text{Sin}[2\theta 0\text{UnitStep}[\text{Sin}[2\text{fm}\pi t]]]$$

**(\*Large – SignalfromHorizontalPolarizationDetector\*)**

$$\langle V_H \rangle = \text{FullSimplify} \left[ \frac{1}{1/\text{fm}} * \text{Abs} \left[ \int_0^{(1/\text{fm})} H[n, \theta 0, \text{fm}, t] dt \right], \{n > 0, t > 0, \text{fm} > 0\} \right]$$

$$\frac{1}{2}\text{Abs}[1 - \text{Cos}[\theta 0]\text{Sin}[\theta 0]]$$

(\*Lock – InAmplifierSignal\*)

$$\text{LI}[\text{fm}_-, \text{t}_-] := 2 * (\text{UnitStep}[\text{Sin}[2 * \pi * \text{fm} * \text{t}]] - \frac{1}{2})$$

$$\text{DIFF}[\text{n}_-, \theta\text{0}_-, \text{fm}_-, \text{t}_-] = \text{FullSimplify}[(\text{Iv}[\text{n}, \theta\text{0}, \text{fm}, \text{t}] - \text{Ih}[\text{n}, \theta\text{0}, \text{fm}, \text{t}]), \\ \{\text{n} > 0, \text{f} > 0, \text{t} > 0, \theta\text{0} \in \text{Reals}\}]$$

$$\text{Sin}[2\theta\text{0UnitStep}[\text{Sin}[2\text{fm}\pi\text{t}]]]$$

$$\langle v_h - v_v \rangle = \text{FullSimplify} \left[ \frac{1}{\text{fm}} * \text{Abs} \left[ \int_0^{1/\text{fm}} \text{LI}[\text{fm}, \text{t}] * \text{DIFF}[\text{n}, \theta\text{0}, \text{fm}, \text{t}] \text{dt} \right], \right. \\ \left. \{\text{n} > 0, \theta\text{0} > 0, \text{t} > 0, \text{fm} > 0\} \right]$$

$$\text{Abs}[\text{Cos}[\theta\text{0}]\text{Sin}[\theta\text{0}]]$$

(\*DifferentialSmall – Signal\*)

(\* $\theta_0$ Estimator\*)

$$\text{FullSimplify}[(\langle V_H \rangle + \langle V_V \rangle), \{\theta\text{0} > 0\}]$$

1

$$\text{FullSimplify} \left[ \frac{\langle v_h - v_v \rangle}{(\langle V_H \rangle + \langle V_V \rangle)}, \{\theta\text{0} > 0\} \right]$$

$$\text{Abs}[\text{Cos}[\theta\text{0}]\text{Sin}[\theta\text{0}]]$$

## APPENDIX B

## MATLAB GUI

### Interfacing the Instruments

Connect

Velmex status ●

Disconnect

Connect LIA

LIA status ●

Disconnect LIA

### 3D-stage Data

Z-C  X-C  Y-C

**Set the stage in Ref position**

Green- Moving the stage

Red- Done

Abs zeroabs Zero ●

Ref zeroRef Zero ●

Stage Status ●

Green- Still working

Red- Done

Stage2 (X) **50**

Stage3 (Y) **50**

Stage1 (Z)

**Number of points (max points )**

### Lock-in Amplifier Data

Time constant  ▼

load Time Constant

Status ●

**Final TC : Do not enter the value**

Final TC

	Magnitude	Phase
A	<input style="width: 60px;" type="text" value="0"/>	A <input style="width: 60px;" type="text" value="0"/>
-B	<input style="width: 60px;" type="text" value="0"/>	-B <input style="width: 60px;" type="text" value="0"/>
A-B	<input style="width: 60px;" type="text" value="0"/>	A-B <input style="width: 60px;" type="text" value="0"/>

Run the stage

120